2001

SURFO Technical Report No. 2001-02

SURFO

Papers from
the

SUMMER UNDERGRADUATE RESEARCH FELLOWSHIP PROGRAM IN OCEANOGRAPHY

at

THE UNIVERSITY OF RHODE ISLAND
Graduate School of Oceanography
and
Department of Ocean Engineering

NARRAGANSETT, RHODE ISLAND

June - August 2001

This program was funded by Grant OCE-9912236 from the National Science Foundation.

GSO Technical Report No. 2001-2

PARTICIPANTS IN THE 2001 SUMMER UNDERGRADUATE RESEARCH FELLOWSHIP PROGRAM IN OCEANOGRAPHY

FELLOWS

Angela Adams	Western Kentucky University, Bowling Green, KY
Brent Buffington	University of Montana, Missoula, MT
Brenda Dolan	Colorado State University, Fort Collins, CO
Robin Glas	University of Maine, Orono, ME
Erin Hodel	University of Missouri, Columbia, MO
David Katz	SUNY Environmental. Science-Forestry, Syracuse, NY
Marcie Kerneklian	SUNY Binghamton, Binghamton, NY
Nicole Persky	Oberlin College, Oberlin, OH
Dan Shaevitz	Columbia University, New York, NY
Rebecca Walker	Hamilton College, Clinton, NY

ADVISORS

Peter Cornillon
Brian Heikes
Chris Kincaid
John King
Roger Larson
Craig McNeil
Sunshine Menezes
Yang Shen
Art Spivack
Randy Watts
Mark Wimbush

MENTORS

Clifford Heil
Anthony Kinirich
Doug Mitchell
Bridget Sullivan
Richard Sweetman
Karen Tracey
Rich Viso
Ting Yang

PROGRAM ASSISTANTS

Paul Hall, Kim Carey & Rhonda Kenny

PREFACE

This report presents the papers written by the ten participants in the 2001 Summer Undergraduate Research Fellowships in Oceanography (SURFO) program at the Graduate School of Oceanography (GSO), University of Rhode Island (URI). This past summer represented the 16th year in which the program has been coordinated and extended through the several disciplines in oceanography and ocean engineering at URI's Narragansett Bay Campus.

The 2001 program was once again a strong success. During the fall of 2000 advertisements were sent to physics, chemistry, biology and geology departments, including faculty advisors at a number of minority colleges. Letters announcing the program were also sent to all Society of Physics Students, college advisors and to individual student members of ΣΠΣ Physics Honor Society. The SURFO web site has continued to be updated and more useful links describing possible research programs at GSO/URI have been added. We received 78 applications for the program, and about two-thirds of these applicants used the electronic application form. This trend of increasing electronic applications has continued since the SURFO web site was initially established in 1997. Ten students were selected for the program with a breakdown by oceanographic discipline as follows: 3 Geological, 3 Physical, 3 Chemical, and 1 Biological. Seven of the fellows who participated in the program are women and one student is from an underrepresented group.

The program began with an orientation session and a tour of the GSO campus and facilities. For the 11 weeks of the summer program, each fellow worked on a research project under the supervision of a faculty mentor and a graduate student mentor. The range of research included: 1) Instrument development for chemical analysis of seawater; 2) numerical and physical modeling of estuarine circulation, ocean front development and plume-ridge interaction; and 3) analysis of sediment geochemistry, lacustrine paleomagnetics, seismic waveform, estuarine plankton, and inverted echosounder data. The results of the lacustrine paleomagnetics data will be presented SURFO participant Becca Walker at the Winter ASLO meeting in February 2002.

Fellows attended a total of 18 biweekly seminars (1-1.5 hour-long) during which faculty members and local environmental consultants gave informal presentations on a range of oceanographic disciplines. These presentations ranged from basic oceanographic topics to topics related to potential academic, governmental and industry-related career possibilities. We also offered lectures on scientific writing and how to create effective oral and poster presentations. This year we also instituted an informal round-table meeting with several faculty members, graduate students and SURFOs to discuss how to get into graduate school and what will be expected of them. Our exit questionnaires revealed that students found these seminars interesting and very useful, and the exposure to a wide range of disciplines/research topics helped students identify additional areas of interest. Other undergraduates (NOT affiliated with the SURFO program) working at EPA or NOAA labs on the Bay Campus and even graduate students at GSO also attend many of these seminars.

Finally, in addition to preparing their written reports, each SURFO gave a 30-minute presentation at the end of the program to summarize her/his results. The SURFOs found the report writing and oral presentation intimidating initially, but they all agreed that it was a worthwhile experience that helped them summarize and realize the scope of their summer projects. Included in the summer events was our annual day of kayaking on the Narrow River, led by Bob Sand, to investigate the flora and fauna of an estuary. A subset of SURFOs also participated in a series of field days funded by other projects where water sampling and fish trawls were made at several locations in Narragansett Bay and Rhode Island Sound. We also continued with our third year of having an informal noontime barbecue for the SURFOs

on the veranda at the Horn Lab. This provided the SURFOs with a taste of graduate-student life in an informal setting where they were able to meet with GSO faculty, graduate students and staff.

One measure of success of our program is if fellows continue on with graduate studies in science and, specifically, in oceanography or ocean engineering. The exit questionnaire indicates that all 9 of the 10 students definitely plan to continue on with graduate studies in science/engineering. Of these, 5 said they are seriously considering oceanography. The participants in the 2001 SURFO program are grateful to the National Science Foundation for its support of the program through grant OCE-9912236. Supplemental NSF funding for undergraduate research was also provided by Brian Heikes (OPP-9907808) and Yang Shen (OCE-9906902) for David Katz and Robin Glas, respectively. The SURFO participants and I would like to thank all of those individuals at URI who contributed to the program's success including those who advised the students and who gave SURFO seminar presentations. In addition, our thanks to Rhonda Kenny and Kim Carey for their assistance in the preparation of this report as well as the administrative, financial and recruitment tasks. Finally, we would like to thank Paul Hall (SURFO Class of 1994) who served as a graduate coordinator for the program and Friday barbecue chef, Friends of Oceanography for providing seminar refreshments, and Bob Sand for running the kayak trip.

Robert A. Pockalny
SURFO Site Director

TABLE OF CONTENTS

Evidence of Diurnal Fish Migration in the Japan/East Sea

Angela N. Adams[1]

Graduate School of Oceanography, University of Rhode Island, Narragansett, Rhode Island

Abstract. In 1999, 25 inverted echo sounders equipped with pressure gauges (PIES) were deployed for two years in the Ulleung basin in the Japan/East Sea. The main goal of this project, funded by the Office of Naval Research contract N00014-98-1-0246, was to study the variability of the Tsushima Current. When these instruments were recovered in 2001, a diurnal signal was present in 22 of the 23 PIES recovered. This signal was determined to have a depth range of 170 to 200 meters and a maximum depth of approximately 250 meters. The maximum depth was determined to occur between 10am and 3pm every day. This diurnal signal can be described by the daily vertical migration of fish. These fish have migration depths and ranges that correspond to those observed in the data. The also migrate at the same times of the day that the data migration period showed, lower in the water column during the day and toward the water surface at night. These and other correlations between the observed diurnal signal and fish migration will be discussed.

1. Introduction

The East Sea, also known as the Sea of Japan, is a unique body of water that demonstrates most of the physical processes that occur in larger ocean basins. The northern portion of the Japan/East Sea (JES) is ice-covered during winter months, whereas the southern portion is subtropical during most of the year. These conditions allow oceanic phenomena that generally do not take place near each other to happen simultaneously and within a few degrees of latitude and longitude. Since the JES simulates large-scale oceans so completely, scientists hope that a thorough study of this region will lead to great improvements of general physical oceanographic knowledge. (Riser 1)

Studies of this region by countries surrounding the JES have taken place for decades. Recently, with improved foreign relations, U.S scientists, with funding from the Office of Naval Research, have actively joined the exploration of the physical properties of this oceanographic region. Approximately 15 investigators are being funded to work collaboratively with Korean and Japanese researchers to study ocean circulation in the JES. The ultimate goal of these projects is to assimilate the observational data into high-resolution numerical models (Riser 34-5).

2. Background

The majority of water entering into the Japan/East Sea enters through the Tsushima Strait, also known as the Korea Strait, which is located in the southeastern region of the JES. Please refer to Figure 1. The current responsible for this dominant source of water circulation

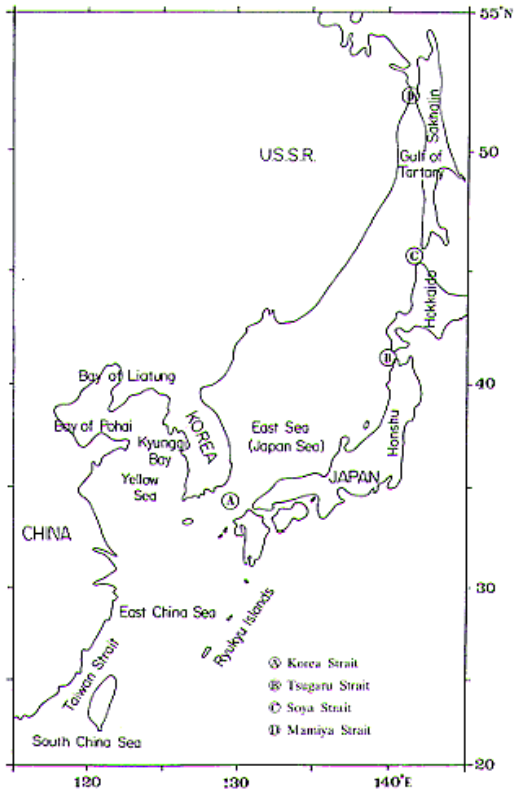

Figure 1. This is a map of the East Sea or Sea of Japan (JES). Figure found in (Kang 26).

in the sea is known as the Tsushima Current. Previous observations during the 1930's and several modeling experiments during the 1980's show that the Tsushima Current splits into two or three branches after leaving the strait and while entering into the Ulleung Basin. One branch travels along the Japanese coast and one branch, referred to as the the East Korea Warm Current, travels along the east coast of the Korean peninsula. (Kim 13-22)

There are two schools of thought on the third branch that may or may not exist between the first two branches. Some believe that there is indeed a third branch that appears during the summer months when the transport through the Tsushima Strait increases. Others believe that meanders or eddies of the East Korea Warm Current are mistaken to be this "third branch." The current branch that travels along the Japanese coast is generally believed to be consistent, but many scientists believe that the East Korea Warm Current (EKWC) follows a path of much more variability.

The main objective of this project was to observe the branches of the Tsushima Current as they travel through the JES. Due to the shallow nature of the region that the Japanese coast branch of the Tsushima Current traveled through, the time-varying transport could not be measured. However, attempts were made to measure

[1]Now at Western Kentucky University, Bowling Green, Kentucky

the time-varying transports of the EKWC and the questionable third branch. Daily maps will be produced with mesoscale resolution to show the path variability of the current. Other work will lead to a better understanding of how shallow and deep currents in this region relate when there are large-amplitude meanders, steep loop formation, and ring pinch off in the upper layers.

3. Data

During cruise HAHNAR06 on the R/V Roger Revelle (June 6-16, 1999, Pusan-Pusan), 25 inverted echo sounders with pressure gauges (PIESs) were deployed in a 5 by 5 array with 55-60 km spacing between sites. These sites are designated by yellow diamonds in Figure 2. Magenta circles designate the 18 current meter moorings located within the array. During this cruise, only 13 of the 18 current meter moorings were deployed. The current meter moorings labeled with an M preceding the site number were deployed on this cruise. Scientists at the Korean Ocean Research and Development Institute (KORDI) deployed the four current meter moorings labeled with KM. The current meter labeled with JM was deployed by Japanese scientists. Two years later on cruise COOK0901 on the R/V Melville (June 21 – July 4, 2001 Pusan-Pusan), 23 PIES were recovered and 12 current meter moorings were recovered. Two of the instruments not recovered were lost due to equipment malfunction. The third instrument never responded to attempted communication. CTD measurements were taken at each PIES site. The fishing industry is prominent in the JES, therefore this instrument is presumed to be flooded or missing due to local fishing activity. Only data collected by the PIES will be discussed in this paper, so the deployed current meter moorings will not be discussed further.

The PIES used in this observational investigation recorded travel time, pressure, and temperature measurements every hour. To measure the travel time, 24 pings were emitted from the PIES one at a time in 10-second intervals for an elapsed time of 3 minutes and 50 seconds at the beginning of each hour. There was a time lockout for each PIES, so that only pings returning to the detector after a certain time period pertaining to a certain depth would be recorded. This depth was generally set to 300 meters less than the actual depth at which the PIES was located. The pressure was averaged over the entire hour, and the temperature measurement was averaged over a one-minute interval just before the data was recorded. The PIES recorded the data at the end of each hour, just before the next travel time measurement series began.

There were three types of PIES instruments used in this investigation. Two of the types recorded the measurements on tapes and the other type utilized a solid-state memory module. Transferring the data from

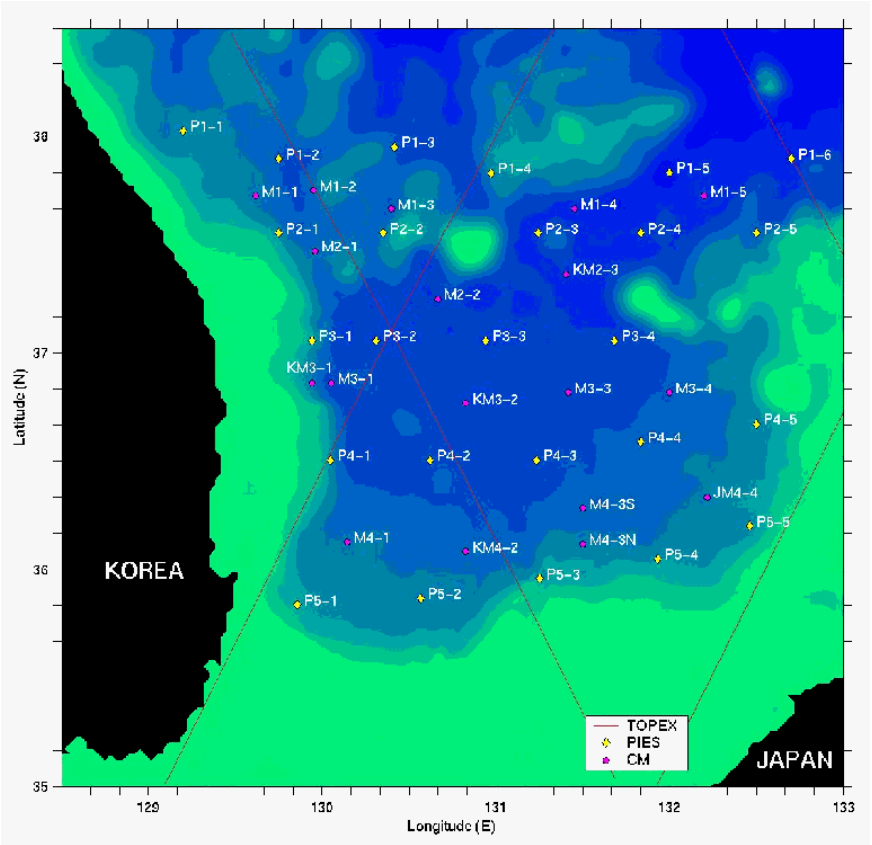

Figure 2. This is a map of all of the sites in the 5 by 5 array of instruments deployed in the Ulleung Basin of the Japan/East Sea. The yellow diamonds represent inverted echo sounders with pressure gauges (PIES) and the magenta circles represent current meter moorings (CM).

the tapes and the solid-state memory recorder took between 45 minutes to an hour. The tapes were read into computer data files using a Sea Data Tape Reader and an Asynchronous Reader Interface (ARI). The ARI interfaced between the tape reader and the computer. The ARI reads data from the tape reader until its buffer is filled. It then transfers the data one record at a time to the computer at a controlled rate. When the buffer is empty, the process is repeated until all data is read from the tape. The PIES with solid-state memory recorders contained a microprocessor. By linking the two via serial cable, the data could be transferred to the computer.

While at sea, data recovered from the PIES were examined for completeness and any obvious complications before processing began. Good travel time, pressure, and temperature records were obtained from all of the instruments with two exceptions. One instrument had no temperature records after deployment, and the travel time measurements of another instrument stopped at about two and a half months into the two-year period.

4. Results

Besides the signal of interest, there was a common phenomenon easily observed in most of the records. This was a diurnal signal that was present in the tau records. Figure 3 is a plot of the unprocessed tau records collected from each site. Site P1-5 is excluded from this figure because the tau data from this site was incomplete. This figure shows that a diurnal signal was present in all but one site, P4-4.

The sites still in question were examined further. P1-1 was not examined more closely due to complications while working with the data set. Figure 4 is a plot of a small section of the tau data from site P2-3. This is characteristic of the diurnal signal present at most of the sites. Of the remaining 20 sites, six sites (P1-4, P3-1, P4-2, P4-3, P5-1, and P5-2) had data sets that were affected by the time lockout that was set for each PIES. At these sites, the lockout was generally set to accept pings returning from objects up to 100 meters lower than the surface of the water. The other sites generally had lockouts corresponding to 350 to 450 meters below the water surface. In these six sites, the diurnal pattern was different from that shown in figure 4. There was no wave pattern to these diurnal signals. Figure 5 shows a diurnal signal from site P4-2 which is characteristic of these six sites.

The diurnal signals seem to have the same general properties in most of the data sets. The signal starts approximately 50 to 80 meters below the desired tau value level and has a depth range of between 170 and 200 meters. The time of day that the signal is at its deepest depth is between 10 AM and 3 PM. The diurnal signal is most often present and most prominent during the period between April and July. Many of the records exhibit the phenomenon at multiple seasonal periods. One other noticeable trait in common among about a third of the sites is that the last half of the travel time data contains little to no diurnal signal. Sites such as P3-3 and P1-6 have a substantial diurnal signal in the first half of the record and the second half has none.

5. Discussion

One possible explanation for this diurnal signal is the daily vertical migration of fish. It is a common occurrence when animals known as zooplankton move toward the water surface at night and move lower in the water column at night. The zooplankton try to maintain a preferred level of light intensity. Fish that eat the zooplankton also join in this migration (Gross 436). The theory fits the observation that the deepest depth was reached between 10 AM and 3 PM (1 AM and 6 AM GMT). This is the time period that the sun is at its highest intensity, and the zooplankton would be the lowest in the water column.

The daily vertical migration of zooplankton can be over 500 meters in range, and as deep as 700 meters (Gross 434-5). According to this, the migration present in the travel time data, which was approximately 200 meters and about 250 meters deep, is very reasonable. Another interesting observation relating to this was made while examining the CTD measurement of temperature at each PIES site. One measurement is plotted in Figure 6. Most of the temperature measurements show a small change between the surface and about 50 meters in depth, and at approximately 200 meters in depth the water column temperature becomes fairly unchanging. In this data set, the range and depth of the migration (approximately 200 and 250 meters, respectively) and the thermocline of the water are fairly similar.

If fish are the cause of this signal, what kind of fish might it be? One consideration is that the fish must have a body type that is optimum for reflecting the PIES ping. It is known that fish such as jellyfish and squid are not good sound reflectors, whereas the swim bladder of a fish is an excellent reflector (Gross 436). Therefore a fish with a swim bladder might be a prime candidate for causing this signal.

Another consideration is whether the signal is caused by large lone fish or by smaller fish in large schools. A lone fish makes a much smaller target for the PIES than a school of fish, making the probability that the school would reflect the pings much higher than that of the lone fish. However, in the data it seems that the closer the fish is/are to the PIES, the more likely the pings are to be reflected. At the maximum depth, there are many data points showing the fish. As the fish migrate(s) up the water column, fewer pings are returned early (refer to figure 4). This could indicate a smaller target such as the lone fish.

More evidence that this signal could be caused by such fish is the location of the sites exhibiting this feature the most. Looking at figures 2 and 3, it is obvious that the sites with the most diurnal signal are located closest to the Tsushima Strait or closest to the coast. These sites are generally more shallow than the other sites due to their location. For this reason and due

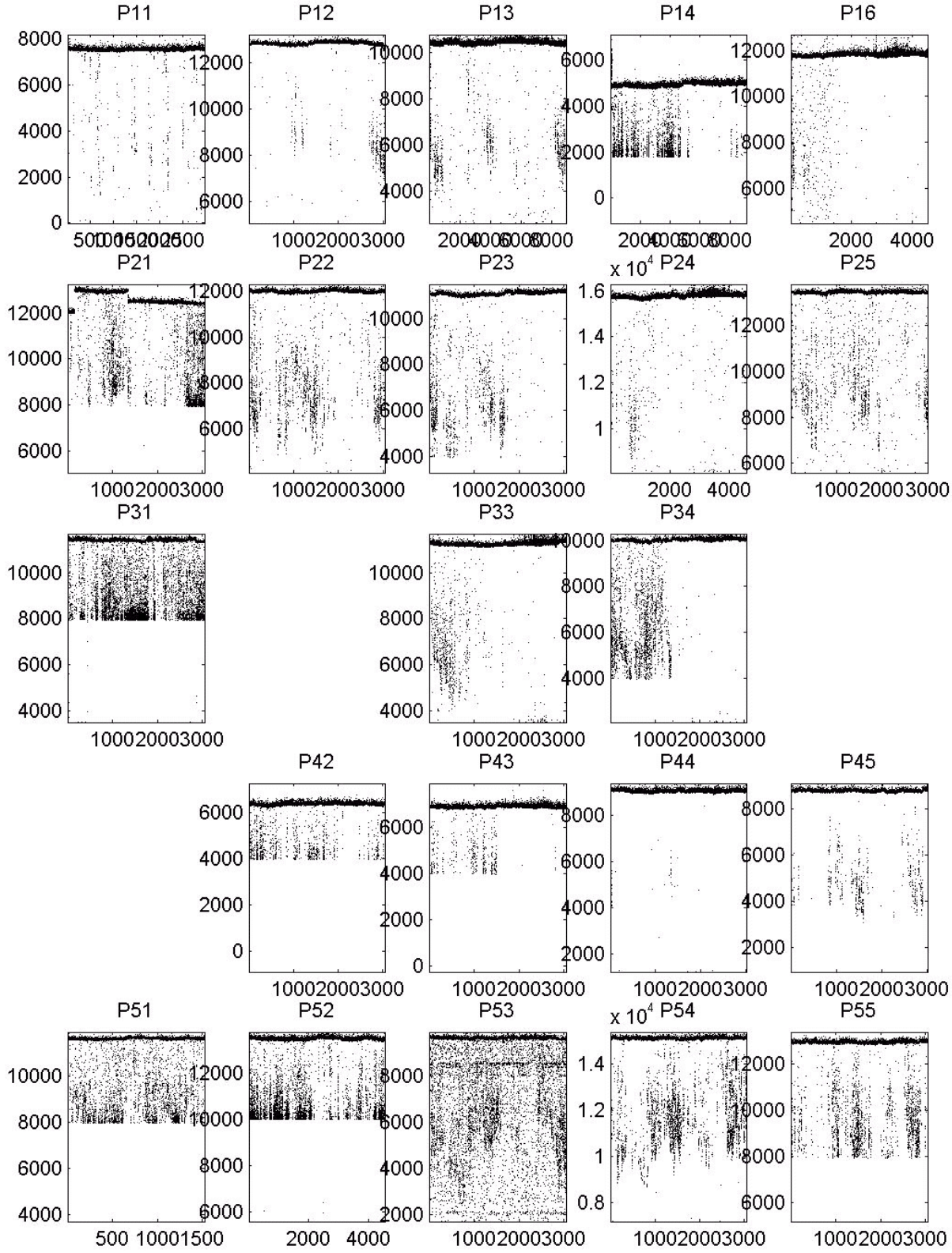

Figure 3. This is a plot of the unprocessed tau signal at each recovered PIES site. A diurnal signal was observed in these data records at 20 sites.

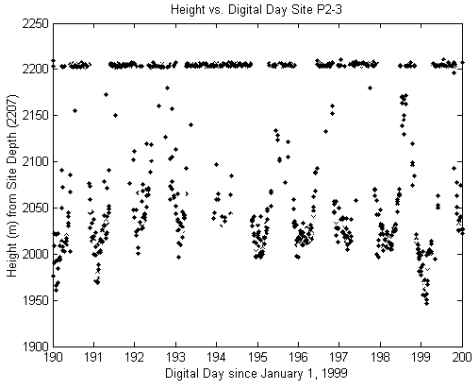

Figure 4. A diurnal signal was determined to be present in 20 PIES sites. This is a typical signal present in a plot of Height from the PIES vs. Digital Day. This signal is from site P2-3. Note that time series is in GMT, local time is 9 hours ahead of this.

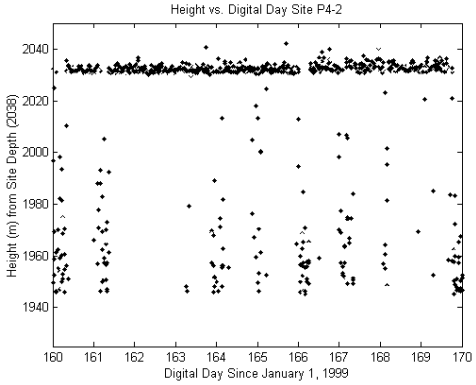

Figure 5. Six of the PIES sites that exhibited a diurnal signal were affected by the time lockout set for each PIES. This is a typical plot of Height from the PIES vs. Digital Day for these six sites. This signal is from site P4-2. Note that time series is in GMT, local time is 9 hours ahead of this.

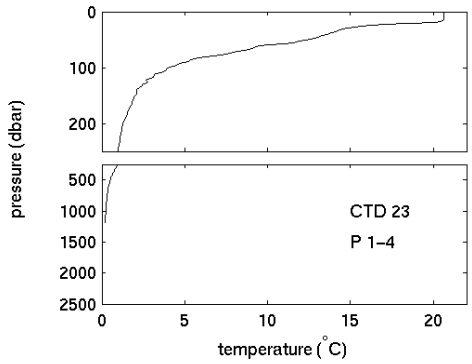

Figure 6. This is a plot of the temperature measurements recorded by a CTD cast at site P1-4.

to more current transport, it would be expected for more fish to be in these areas and the data to show a larger diurnal signal.

While looking at the raw travel time plots, it is obvious that this is a seasonal signal. It was determined that the months of April through July had the most diurnal signal. Further study of this seasonal variation was not completed. It would be interesting to look at the seasonal signal at each site to see how much the maximum depth of the migration changed over time as well as the migration depth range. It is not easily discerned whether the seasonal signals at each site are similar due to the time lockouts in some of the instruments and the lack of diurnal signal at other sites at various times. An explanation for the abrupt end of the signal half way through the two-year observational period would also be interesting to know.

6. Conclusions

During an observation time of 2 years, 25 PIES were recording the travel times of pings every hour in the Japan/East Sea. 23 of these instruments were recovered, and 22 of these had good travel time records. Of these 22 instruments, 20 were shown to exhibit a diurnal signal. Six of these 20 instruments experienced effects on the measurement of the diurnal signal due to the time lockout set for each PIES. The remaining fourteen instruments exhibited diurnal signals varying in density not only between instruments but also between seasons in the tau records at the different sites. There is strong evidence linking these diurnal signals to the daily vertical migration of fish that follow zooplankton in their daily migration.

The next step is to determine what fish is causing this diurnal signal, if it can be determined. Further investigation of the travel time records will most likely be necessary in order to accomplish this. These investigations might include determining the seasonal signal in each record or trying to see if any migration occurs from site to site. If this fish can be pinpointed, this observational data could be very helpful to an interested biological scientist.

Acknowledgments. I would like to thank Randy Watts and Mark Wimbush for giving me the opportunity to enjoy this wonderful research experience. I would also like to thank Karen Tracey and Doug Mitchell for all of the things they have done for me this summer and for having unlimited patience when needed. Last but not least, I would like to thank Rob Pockalny and Paul Hall for all the work they did to coordinate this program.

References

Gross, M. Grant. *OCEANOGRAPHY a view of the earth.* Englewood Cliffs: Prentice Hall, 1972.

Kang, Sok kuh, Sang-Ryong Lee and Ki-Dai Yum. "Tidal Computation of the East China Sea and the

East Sea." K. Takano *Oceanography of Asian Marginal Seas* New York: Elsevier Science Publishers, 1991: p. 26.

Kim, Kuh. "What is CREAMS?" http://pices.ios.bc.ca/picespub/ppress/Jan97/Creams.pdf, August 11, 2001.

Riser, Stephen C. "Creams, PICES, and the Exploration of the Japan/East Sea." *Pices Press* July 1998, Vol. 6 No. 2: p. 1; 34-5.

Frontal Dynamics and Developmental Characteristics in Near Shore Seas

Brent Buffington[1]

Graduate School of Oceanography, University of Rhode Island, Narragansett, Rhode Island 02882

Abstract. A rotating table with a one-meter diameter capable of constant rotation to within 10^{-3} rad · sec^{-1} was used as the basis of all experiments to investigate the developing characteristics of frontal formation in the open ocean. To examine the formation processes, a 50-cm diameter, rotating disk was placed at the bottom of the tank initially filled with a constant density fluid. The disk was rotated slowly relative to the rotating tank resulting in a differential flow, giving rise to a frontal region (sharp discontinuity) between the two flow regimes.

Through numerous designs and prototypes, a semi-automated dye injection system was constructed to aid in the visualization of fluid flow(s), and computer programs were used to estimate velocity vector fields from digital images taken at specified time increments. In addition, the importance of neutrally buoyant dyes, rotation rate, rotation direction, surface stress resulting from the air above the fluid in the tank, and Ekman transport, were investigated. In essence, the methods for further analysis, which could possible lead to the ultimate goals of characterizing frontal formation processes, were developed.

1. Introduction

A front can be defined as a region displaying an increased horizontal gradient of some fluid property when compared with the mean background gradient. Specific fluid property variations include density, temperature, salinity, and/or velocity. Fronts influence weather and climatic tendencies, and through upwelling of nutrients from deep waters at frontal boundaries, a high biological productivity zone may be produced, associated with both ecological and economic importance.

Through the application of a multi-image edge detection algorithm developed at the University of Rhode Island (URI) to the NOAA/NASA AVHRR Pathfinder sea surface temperature (SST) data set acquired from the Jet Propulsion Laboratory, SST fields (Fig. 1) were produced for the North Atlantic (Z. Shan, 1999). In the figure, frontal regions are signified by an abrupt change in color over a finite distance. Through observed ship data (Voorhis and Hersey 1964), the images produced by URI, and many other studies, frontal formations in the open ocean have been well documented, but the characteristic processes associated with ocean fronts are not well known. The study described here was undertaken to address from a laboratory perspective frontogenesis associated with fronts remote from any boundary or changes in bottom topography.

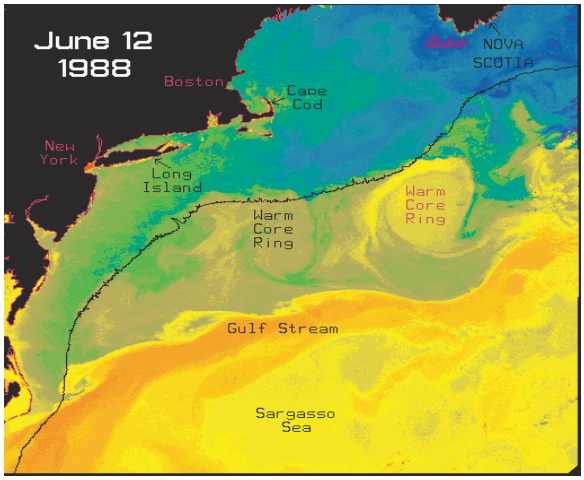

Figure 1. Sea surface temperature (SST) field of the North Atlantic taken in June 1988.

2. Experimental Setup

A rotating table was used to slowly spin up a single density body of water to solid body rotation. With an addition of a rotating disk located at the bottom of the tank, a velocity sheer resulted. Through two digital cameras, an arsenal of digital editing software and computer analysis programs (Matlab), insight into the dynamics associated with ocean fronts was obtained.

The laboratory simulations are exclusively concerned with the fronts in a barotropic, shallow fluid characterized by horizontal motions (horizontal gradients) dictating the distributions of fluid as opposed to a baroclinic ocean where vertical processes dominate. Each experiment consisted of a single density water layer 4 cm thick, a table rotation rate of 1 rad/sec counter-clock wise (therefore simulating the northern hemisphere), and an inner disk speed of approximately one rotation every 15 minutes, although the direction did vary.

2.1. Rotating Table

The Geophysical Fluid Dynamics Rotating Table used in this work, designed by the Professor Ross Griffiths of the Geophysical Fluid Dynamics laboratory of the School of Earth Sciences at the Australian National University (ANU), is a round 1 m (outside diameter) clear acrylic tank mounted on a 1 m diameter anodized cast aluminum table top. To minimize optical deformation due to the tanks round cast, a clear acrylic octagon shell was built around the outside of the tank. By filling the volume between the round tank and the octagon encasement to at least the depth of water in the inner tank, a larger observation surface was created normal to the line of sight. A removable clear acrylic

[1]The University of Montana, Missoula, MT 59801

plate mounted near the bottom of the tank consists of a gear driven inner disk (26.4-cm radius) centered on the axis of rotation of the tank. This disk is power by a variable speed, 0-90 V dc motor. The boundary between the stationary outer ring (with respect to the rotating frame) and the rotating inner disk gives rise to a difference in velocities hence a shear region where frontal formation is highly probable.

The entire tank was mounted securely onto a cast alloy housing containing a bank of 20 slip rings/brushes which make up to 60 connections (4 VHS) possible from the rotating table to the stationary Turntable Control unit. Ten main power slip rings gave the table the ability to maintain four separate power circuits on the table.

The super structure consists of four re-enforced (cross beams and top support) aluminum uprights optimal for mounting addition experimental equipment such as video cameras, still image cameras, lights, power strips, etc.

The rotating table is controlled via a stationary Turntable Control unit. This unit consists of mechanisms for controlling the rotation rates and directions of both the entire table and the inner disk, the activation of the dye injection system (refer to section 2.2), a digital read out of the high-sensitivity electromechanical tachometer in rad/s, a digital read out of total revolution, and as mentioned previously, up to 60 electrical and 4 video connections for additional experimental equipment.

The table has a rotational speed stability of $< \pm$ 0.01% at 0.2 – 10 rad/s and ~0.2% at 0.05 rad/s and consists of a 0.1 – 19.1 rad/s rotation rate range

2.2. Dye Injection System

To visualize fluid flow in the tank, neutrally buoyant dyes of different colors were injected in discrete amounts. All dye consisted of standard food coloring in combination with water of the same density as the tank water. To counteract the effects of the denser food coloring, a very small amount (relative to the amount of food coloring) of rubbing alcohol was added. Neutrally buoyant dye was required to accurately track the flow of the fluid within the water column. When the dye was denser than the water, it gradually sank to the bottom of the tank, becoming entrained in the bottom Ekman layer that was of no value with regards to frontal formation. Similarly, when the dyed fluid is too light it rises to the surface and follows the flow in the surface Ekman layer.

An injection system was needed to both supply and regulate the neutrally buoyant dye. Through a series of designs, tests, and prototypes, a nearly fully automated dye injection system was built. Three 9V dc electric solenoid valves were used to regulate the volume of dye injected, and were wired through the signal connections of the table, to the signal connections on the control panel, and finally through a series of switches mounted on the control panel. Each valve could be independently controlled, and in addition, a master switch was available to control all three valves simultaneously. Dye was supplied to the valves via 1/8" I.D. vinyl tubing connected to three dye vessels mounted on the super-structure, each containing a different color dye. Two dye injector units (Fig. 2) served as the mechanisms to place the dye into the water column. Both were constructed using 1/8", 3/32", and 1/16" (all O.D. diameters) aluminum tubing mounted in white vinyl blocks (approx. size: 1" x 2" x 6").

It must be noted this injection system was the end result of many ideas, methods, and prototypes for dye injection. The evolution of dye injection through the course of the research was as followed:

Manual injection – Releasing drops of food coloring by squeezing a food coloring container and/or dropping potassium permagantate dye crystals into the tank.

Manual injection – Prototype injection system featuring two 1/8" O.D. pieces of aluminum tubing with dye regulated by two separatory vessels each containing a different color dye.
Manual injection – First full-scale (six injectors) injection system with dye regulated by the same two seporatory vessels. (Three injectors/color).

Semi-automated injection – Six dye injectors regulated through electric solenoid valves, which were controlled via four switches (one main, three valve specific) mounted on the control panel.

Semi-automated and manual injection – Same as above with addition of second six-injector injection unit controlled via original two separatory vessels. (Electric solenoid valves were not an option in second unit due to time limiting factors).

2.3 Digital Imagery and Analysis

A still image digital camera and a digital camcorder were used to capture the fluid motion in the tank. A live feed connection from the table was maintained through each experiment to both record directly onto a VCR

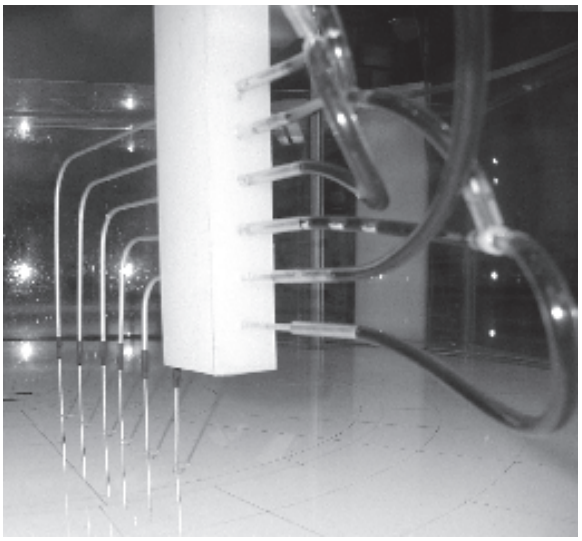

Figure 2. Angled side view of a single six-injector dye injector unit

(real time video) and, using computer software, to obtain a sequenced movie constructed through images taken every second. The sequenced movie was used to better interpret the fluid motion due to the slow rotation rate of the inner disk and hence the relative velocities of the fluid.

To obtain a highly detailed and near exact picture of the fluid's relative velocities, a series of 90 digital still images were taken at two-second intervals. The images were then analyzed with a Matlab program to obtain a vector field giving both direction and magnitude of the water column's velocity at specified points (every 5 pixels in x and y directions) in the tank.

The program took each 320 x 240-pixel image and broke them up in to [10 x 10] pixel squares. The program proceeded to take one [10 x 10] square from image 1 and compared it with a [10 x 10] square in image 2 shifted i pixels in x and j pixels in y compared to the first image. By assigning every color a number value ranging for 1 to 256, the program could take the difference between the two images (image 2 – image 1), resulting in a new [10 x 10] matrix. Each term in the resultant matrix was squared and the sum over the 100 elements in the [10 x 10] pixel square yielded a single number representing the similarity (the nearer zero the more similar) between the two [10 x 10] pixel squares used to obtain the difference field. This process was repeated for $-10 < i < 10$ and $-10 < j < 10$ in image 2. The i, j offset corresponding to the minimum of the sum of squares was taken as the displacement of the corresponding water mass from image 1 to image 2. With displacement and time known, a velocity vector was obtained. This process was repeated for each location on a regular grid defined by every 5th pixel and every 5th line of image 1. The result a complete vector velocity field over the image. The program followed the same series of step for each pair of images resulting in 89 velocity vector fields for the three-minute period sampled. Figure 3 exhibits one of these vector fields superimposed over an image 1 of the fluid for the particular pair of images.

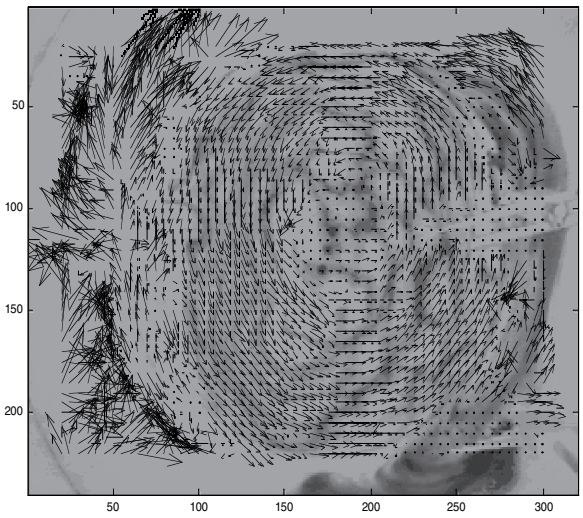

Figure 3. Velocity vector field superimposed over dye trails.

3 Results and Discussion:

3.1 Wind Stress:

A very irregular and chaotic fluid motion was observed in initial experiments when dye was manually injected via dye droplets. It was believed that at least some of the random motion could be attributed to the presence of air turbulence directly above the tank hence effect the top of the water column.

By rotating the table with the inner disk *not* rotating for a time long relative to the spin-up time for the fluid in the tank, all transient turbulent motion caused by setting the table into motion would slowly die off, hence the body of water would reach solid body rotation. This would not be the case however if an added wind stress were present. Therefore, an experiment was conducted in which the table was rotated at 1-rad·sec^{-1} and potassium permagantate dye crystals were dropped into the tank at approximately half-hour increments. The presence of dye transport (vertical water column displacement relative to the rotating tank) would signify the lack of solid body rotation. Dye crystals added at 10,064 revolutions (approximately 17 hours) showed signs of the presence of a bottom Ekman layer as indicated by the dye trails in Fig. 4.a.

To verify the lack of solid body rotation was in fact due to wind stress, the tank was covered with saran-wrap. The tank was again rotated at 1 rad · sec^{-1} and potassium permagantate crystals were dropped into the fluid. After roughly one hour, essentially all motion in the tank was gone (Fig. 4.b). This result both verified wind stress was the cause for some of the irregular motion and gave a base line for the "spin-up time" (one hour) which was used for the remainder of the experiments. A permanent three-piece removable lid was constructed out of 1/8" Plexiglas to better suit all remaining experiments.

3.2 Frontal Region Stability

As previously stated, the table always rotated in a counter clock-wise manner. For the first month of experiments, which were primarily used to refine numerous qualities of the table such as lighting, camera positions, the rotation rate of inner disk, and several dye injection system variations, the inner disk was rotated only in the opposite direction as the table (clock-wise). While a frontal region was formed, the stability of the front was less than desirable. Upon the suggestion of Tom Rossby, the inner disk's rotation direction was switched (clock-wise) resulting in a much more stable frontal region.

3.3 Data

Due to a difference in relative fluid velocities, a sheer stress was present acting on both the stationary fluid (in the rotating frame) and the fluid in motion located over the inner-rotating disk. This sheer stress caused a difference in velocities between the fluids and their

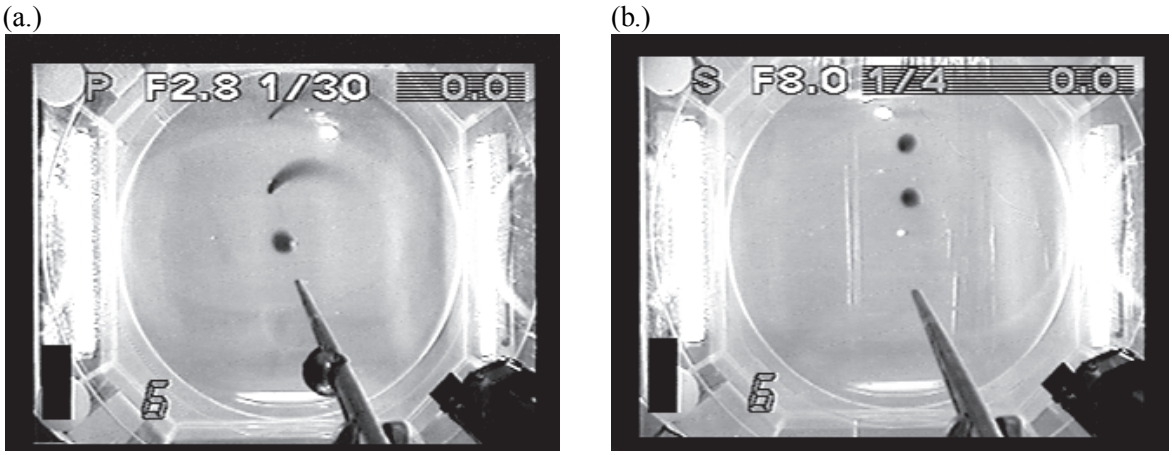

Figure 4. Effects of wind stress; (a.) Fluid unable to reach solid body rotation due to wind stress, (b.) improved situation in which solid body rotation was reached through installation of tank cover.

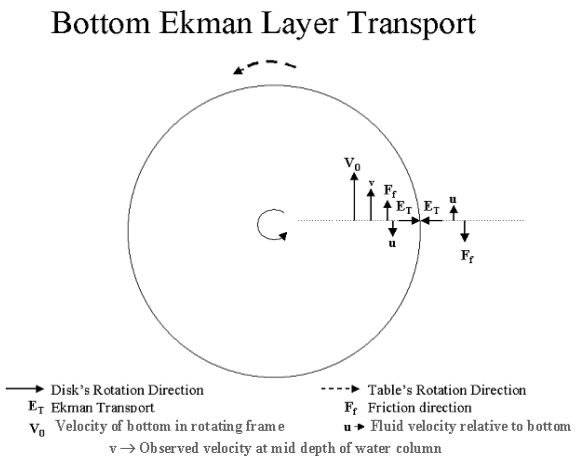

Figure 5. Vector Diagram of Bottom Ekman Layer net transfer of fluid

respective surfaces below resulting in a counter clockwise velocity relative to the base over the outer ring and clockwise over the inner disk. This difference in velocities gave rise to a frictional force in the opposite direction of the relative motion. Due to the rotating reference frame, a Coriolis force was present resulting in a net transport of fluid towards the sheer boundary. (Fig. 5) Taken over the entire tank, the net transport of fluid was convergent on the boundary between the rotating disk and the non-rotating portion of the bottom in the bottom Ekman layer. Conservation of mass requires that the water column above the bottom Ekman layer be divergent. Figure 6 was extrapolated from the data collected from the Matlab program described in section 2.3. In both graphs, the velocities of the bottom (i.e., the velocity that the water column would have if it followed the bottom) have been removed, hence the velocities seen are due purely to the interaction of the two fluid regions. As seen in figure 6a, a net divergence

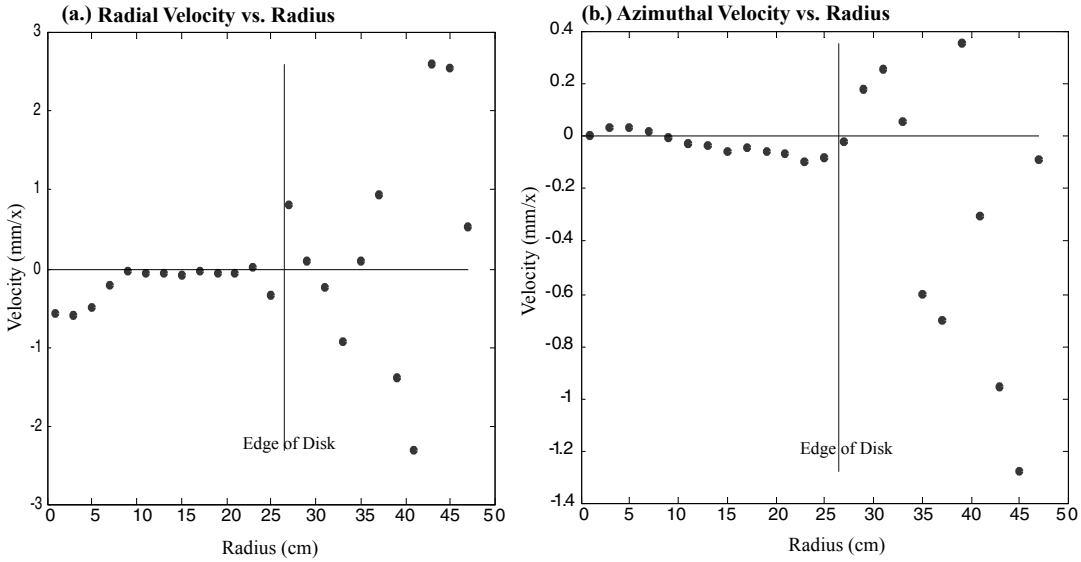

Figure 6. (a.) Radial and (b.) azimuthal velocity components extrapolated from digital images.

(velocities away from boundary) was present in the water column near the sheer boundary verifying our hypothesis.

Another interesting feature of the resultant data is the presence of the negative transient radial velocity within the innermost 5-cm of the tank. This is the result the computer program limits. Since the fluid is traveling very slowly, less than a pixel every two seconds, the program does not register fluid motion, hence a zero resultant velocity. Therefore, when the positive velocity of the bottom of the tank is subtracted, a negative velocity results.

4 . Conclusion:

The goal of these experiments was to gain a detailed understanding of frontal formation processes. While this was not accomplished in the allotted 11-week period, the methods for further analysis, which could possibly lead to the ultimate goals of characterizing frontal formation were developed. This included a highly versatile dye injection system, multiple Matlab programs, and various facts learned through experimentation such as the importance of wind stress as well as relative rotation rates and direction. With these developed methods and some minor modifications such as the use of Labview software, (for a more detailed analysis due to it's higher resolution and fully automated synchronization capabilities) questions such as, "Does a front form in one particular position and propagate around the shear region in a uniform manner, or does it form near the sheer region all at once?" can be answered.

Acknowledgments: This research opportunity was supported by the National Science Foundation (NSF). All research equipment in the Geophysical Fluid Dynamics Lab at the Graduate School of Oceanography (GSO) of the University of Rhode Island was funded under NASA grant number NAG 53736. A special thanks is in order for Professor Peter Cornillon and GSO graduate student Anthony Kirincich. They were always willing to do whatever was necessary, and sometimes more, to help me accomplish the intellectual and/or physical task(s) at hand. Additional thanks to the people that make the SURFO program possible, Rob Pockalny, Paul Hall, Kim Carey, and Rhonda Kenny. Last but not least, GSO graduate student Michael Sutherland, Mark Schneider, Professor Craig McNeil, Professor Tom Rossby, and all the other SURFO's.

References

Cornillon, P. and Z. Shan, 2000: On the Characteristics of Subtropical Fronts in the North Atlantic, unpublished

Voorhis, A. D. and J. B. Hersey, 1964: Oceanic Thermal Fronts in the Sagasso Sea. *Journal of Geophysical Research*, **69**, 3809-3814.

Development and Testing of New Dissolved Gas Sensor Technologies for Monitoring Air-Sea Gas Exchange

Brenda Dolan[1]

Graduate School of Oceanography, University of Rhode Island, Narragansett, Rhode Island

Abstract. This project prepared a Pro-Oceanus Systems, Inc. gas tension device (GTD) for deployment at the Martha's Vineyard Observatory in collaboration with Dr. Wade McGillis (WHOI). It will be deployed sometime during the week of August 15, 2001. This provides an important new communication technology for dissolved gas sensors. Data will be collected real-time *via* the internet. This project also examined the properties of an oxygen absorbent used in new dissolved oxygen/nitrogen sensors. Experiments were performed on the absorbent by injecting research grade oxygen into a nitrogen chamber in AirWare vacuum tight glassware submerged in a temperature bath. The time constant for the removal of oxygen was determined to be 31+/-2 seconds, and all of the oxygen was removed in the nitrogen environment. The time constant of the absorbent was found to be limited by the chemical reactions. These new dissolved gas sensor technologies will be used to develop more stable and reliable instruments for measuring dissolved gases in seawater.

1. Introduction

1.1. Background

Current climate change trends are raising critical questions about the future of our planet. Understanding the role of the oceans in climate change is a necessary step towards predicting future climates. Studying air-sea interactions, especially gas exchange rates and mechanisms, better quantify the importance of the oceans in sequestering green house gases, and ultimately provide knowledge and predictive capabilities through modeling efforts.

Current *in-situ* dissolved gas measurement techniques are lacking in the technology to be able to remain stable over measurement times of years. Instruments also need to be able to withstand severe storms, as it is thought that significant gas exchange occurs during storms. Automated oxygen probes are subject to bio-fouling, and drift significantly over long deployments. Analysis of dissolved oxygen using the Winkler Titration Method is limited to shipboard samples, which also becomes costly.

It is necessary to develop new sensors that are more stable over time and can operate and withstand extreme oceanic conditions. The objective of this project is to develop new gas tension device (GTD) technologies by communicating real time with a deployed GTD using a RS-232 serial connection, and to study the properties of an oxygen absorbent which will be used in a new nitrogen/oxygen sensor.

[1]Now at Colorado State University

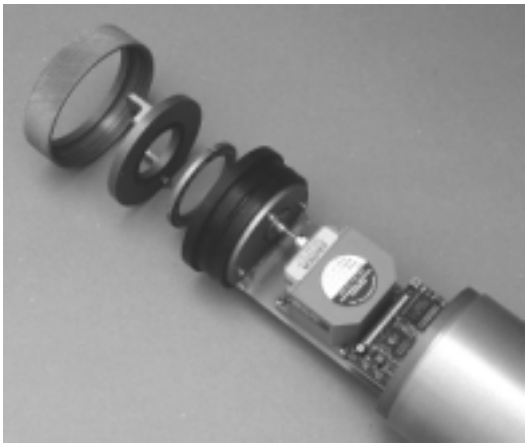

Figure 1. Pro-Oceanus Systems, Inc. Gas Tension Device. Image courtesy of Pro-Oceanus Systems, Inc. (Halifax, N.S., Canada).

1.2. Theory – Gas Tension Device

Figure 1 shows a Pro-Oceanus Systems, Inc. Gas Tension Device (GTD) developed by McNeil et. al. The GTD works on the principle of diffusion of gases through a semi-permeable membrane. A sample volume of air inside the GTD is allowed to equilibrate with the water, and since the membrane is permeable only to gases, at steady state the pressure sensor inside the GTD reads the gas tension of the water. Gas tension, P_T, is the total pressure of dissolved air, composed primarily of nitrogen, pN_2 (~78%), oxygen, pO_2 (~ 21%), water vapor, pH_20 (~1%), and residual trace gases, mainly argon, p_r, or:

$$P_T = pN_2 + pO_2 + pH_2O + p_r. \qquad \text{(Eq 1)}$$

In situ gas concentrations, c, can be related to the partial pressures of the gases by using solubility coefficients, β, which are known functions of water temperature, T, and salinity, S [Weiss, 1970].

The effects of bio-fouling can be minimized by placing small amounts of high molecular weight, low molecular diffusivity, anti-fouling agents on the air interface of the membrane. The anti-fouling agent slowly diffuses through the membrane and minimizes bio-fouling problems.

1.3. Theory – Nitrogen/Oxygen Sensor

The newest technology in dissolved gas sensors is a nitrogen sensor. This operates on the same principal as a GTD, except that an oxygen absorbent is added in the air chamber to remove all the oxygen. The internal pressure sensor thus measures the partial pressure of nitrogen,

$$P_T = pN_2 + pH_2O + p_r. \quad \text{(Eq 2)}$$

By assuming, with negligible error [McNeil et al., 1995], that trace gases are air saturated with respect to the mean water column properties we may calculate pN_2 from Equation (2), as water vapor is a known function of temperature and salinity.

If an independent measurement of the total gas tension (i.e.: with a GTD) is also made, the partial pressure of oxygen in the seawater can also be measured directly by subtracting equation 2 from equation 1.

An important part of developing the oxygen/nitrogen sensor is finding the right absorbent. The absorbent must remove all of the oxygen, as well as have a short time constant for absorbing the oxygen compared to the time constant for equilibrating the GTD. Further, the absorbent must remain stable and not become liquid in the presence of moist air. The residual oxygen pressure in the air chamber is a function of the ratio of the time constants,

$$P_{residual} \sim \tau_{absorbent} / \tau_{N_2 chamber} * \Delta P_{O_2}, \quad \text{Eq (3)}$$

where $\tau_{absorbent}$ is the time constant for absorption of oxygen by the absorbent, $\tau_{N_2 chamber}$ is the time to equilibrate the air chamber inside the nitrogen sensor with the sea water, and ΔP_{O_2} is the pressure difference of oxygen across the membrane, approximately 200 mbar.

The absorbent being tested in this experiment is proprietary to Pro-Oceanus Systems, Inc., however key ingredients include activated charcoal and iron filings. The oxygen is removed by a catalyzed process of rusting, following the chemical reactions [Brady, 1981]:

$Fe(s) \rightarrow Fe^{+2}(aq) + 2\ e^-$ Eq (4)
$O_2\ (aq) + H_2O + 2e^- \rightarrow 2OH^-$ Eq (5)
$Fe^{+2}\ (aq) + 2OH^-\ (aq) \rightarrow Fe(OH)_2\ (s)$ Eq (6)
$Fe(OH)_2\ (s) \rightarrow Fe_2O_3 * xH_2O(s)$ Eq (7)

The activated black carbon provides a very large surface area on which the above reactions can occur.

Developing an oxygen/nitrogen sensor requires an understanding of the absorbent used to remove the oxygen. Pertinent questions include: does the absorbent remove all the oxygen?; what is the time constant for the reaction?; what is the time constant a function of? A series of experiments were performed on the absorbent to address these questions. We expected the time constant of this absorbent to be governed by the chemical reactions given in equations 4-7, rather than a function of the amount of absorbent present or the volume of oxygen injected.

2. Methods

2.1. Gas Tension Device – Laboratory Testing

A GTD made by Pro-Oceanus Systems, Inc. was prepared for deployment at Martha's Vineyard Observatory in Massachusetts, in collaboration with Dr. Wade McGillis of Woods Hole Oceanographic Institute. Preparation included assembling the instrument and completing a series of tests to ensure that the instrument was functioning properly and had no leaks. The GTD was equipped with a membrane of thickness 0.005 in., a ParoScientific pressure sensor, and a RS-232 Serial connector. The first test was conducted in the pressure tanks at the University of Rhode Island Graduate School of Oceanography Equipment Development Laboratory. The pressure sensor and circuit board were removed from the canister before it was sealed to ensure no damage would be incurred should the instrument housing leak. The instrument was first subjected to a hydrostatic pressure of 70 dbar for 2 minutes. The pressure was then decreased to 10dbar, and the instrument was left for 2 hours.

A second test was performed to ensure no internal air leaks. The pressure sensor and circuit board were replaced in the canister, and the GTD was left submerged in a Hart Scientific precision temperature bath at 20.00°C for a day. The GTD was connected to a

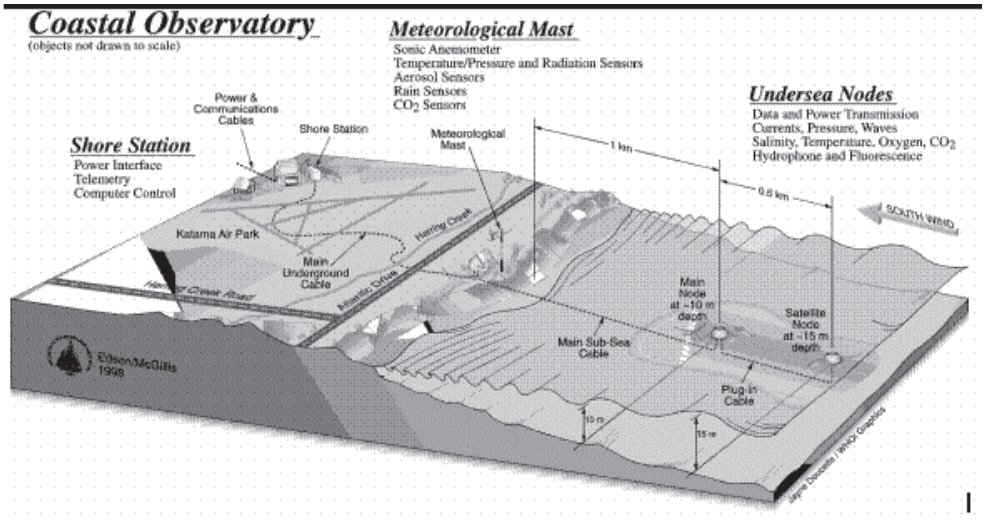

Figure 2. Martha's Vineyard Coastal Observatory. The GTD will be wet-plugged at the main node, 1 km off shore at a depth of 10m. Image courtesy of Dr. Wade McGillis. [http://adcp.whoi.edu/MV_OBSERVATORY/index.html].

computer, which recorded the output from the pressure sensor.

2.2 Gas Tension Device – Deployment

The GTD will be deployed at the Martha's Vineyard Observatory on August 15th, 2001. It will be wet-plugged into the node 1km off shore at a depth of 10m (figure 2) and it will remain at the site for six months to a year. Data will be accessed real-time via the Internet on a web-site designed to retrieve the data.

2.3 Absorbent

Experiments were performed on oxygen absorbents in vacuum tight AirWare Glassware assembled in the configuration shown in figure 3. The glassware between valve A, valve B, and valve C is the oxygen chamber. The pressure of the oxygen chamber was set to near atmospheric pressure (1000 mbar). The glassware between valve C and valve D serves as the nitrogen chamber. The pressure was measured in this chamber by a ParoScientific pressure sensor. A large nitrogen volume compared to the pressure sensor volume was needed to minimize the diffusion of oxygen into and out of the pressure sensor. The nitrogen pressure was reduced by evacuation to 850mbar to simulate atmospheric conditions and mimic the conditions encountered by the absorbent in a useful nitrogen sensor operating in the ocean. The glassware was first flushed with research grade nitrogen for 5 minutes, then evacuated and sealed between valves C and D. Research grade oxygen was then flushed through the glassware from valve A to valve B for 5 minutes. Oxygen injections were done by opening and closing valve C. All experiments were done while submerged in a Hart Scientific precision temperature bath set to 20.00°C to minimize the effect of temperature fluctuations.

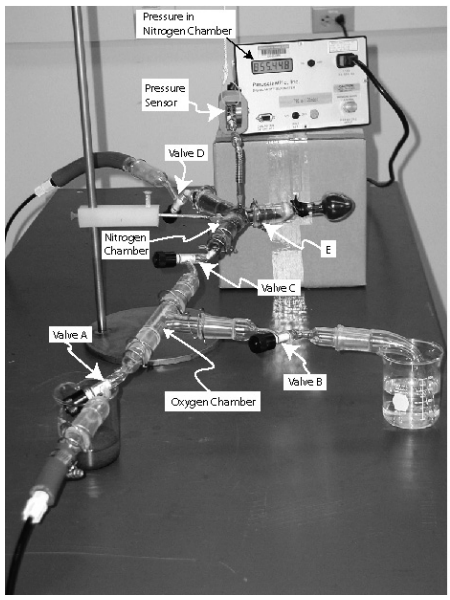

Figure 3. Glassware configuration used to test the absorbent. Valve C was opened to inject oxygen into the nitrogen chamber.

2.4. Steady State (As t-> infinity)

In order to investigate the properties of the absorbent as time goes to infinity, a small amount of absorbent was placed in a 125ml flask. The 125ml flask was attached to point E (fig 2) with approximately 16g of the absorbent. The entire setup was submerged in the temperature bath, and an oxygen volume of approximately 16mbar was injected into the nitrogen chamber. Data was recorded over a few hours.

2.5. $\tau_{absorbent}$

To investigate the properties of the absorbent, an experimental apparatus was assembled to measure the time constant of the reaction. The setup for the steady state experiment needed to be modified because the diffusion time of oxygen through the glassware was the governing time constant, namely:

$$\tau = z^2/\text{[illegible]} \qquad \text{Eq (8)}$$

where z is the length of the glassware, and [illegible] is the diffusivity of oxygen (~30cm^{2}s^{-1}), and τ~30 min.

Therefore, the entire nitrogen chamber, from valve C to valve D was packed with absorbent (approximately 92g), as shown in figure 4 . The 125ml flask was exchanged for a 25ml flask at point E. Multiple injections of oxygen of various volumes were then injected into the nitrogen chamber.

3. Observation and Results

3.1. GTD

The GTD was determined to be leak proof, both outside and inside. The GTD is scheduled for deployment sometime during the week of August 15, 2001. The time constant for equilibration of the GTD is expected to be ten to twenty minutes.

3.2. Absorbent

Figure 5 shows the results of the steady state experiment. Three hours after the injection of 15 mbar of oxygen, the pressure of the nitrogen chamber was

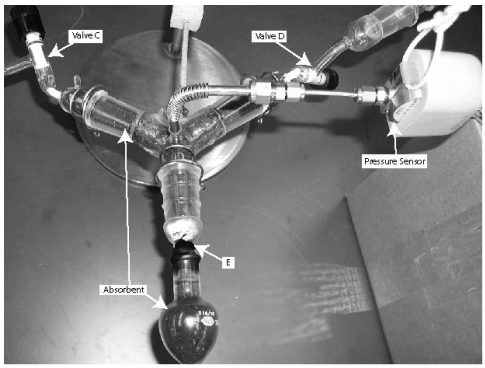

Figure 4. Experimental setup used to determine the time constant of the absorbent. The nitrogen chamber is packed with absorbent to reduce the effects of oxygen diffusion through the glassware.

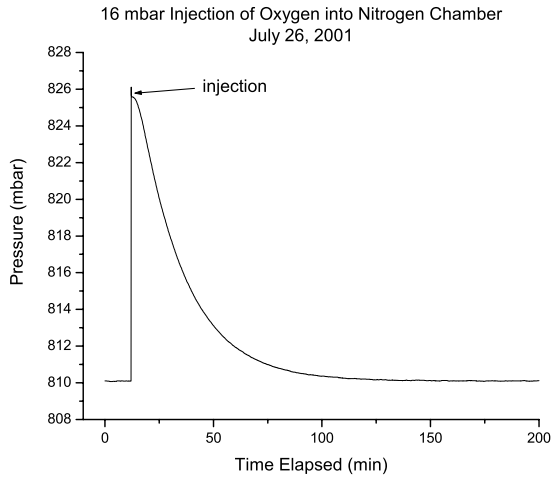

Figure 5. A 16mbar injection of research grade oxygen to determine the steady state residual pressure of oxygen in a nitrogen atmosphere. The spike in the pressure at t=0 is due to the effects of closing valve C during the injection.

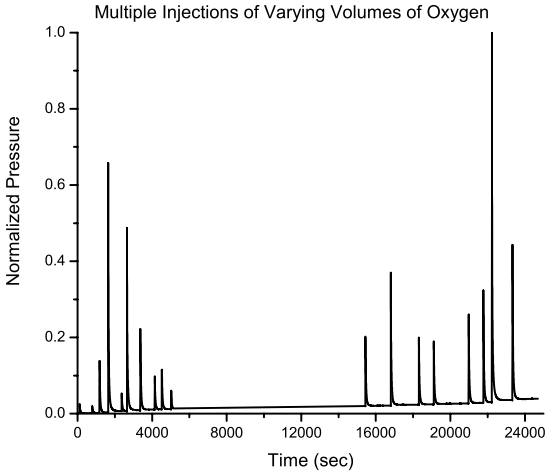

Figure 6. Oxygen injections of varying volumes into a chamber of nitrogen packed with absorbent. The gradual increase in initial pressure over time was determined to be a leak and did not significantly alter the results of these data.

within 0.013 mbar of the initial pressure. We find that the oxygen is removed from the chamber to $P_{residualO_2}$=0.01+/-0.02mbar, verifying our assumption that the absorbent does indeed remove all available oxygen within the absorbent chamber in the presence of a nitrogen atmosphere.

3.3. $\tau_{absorbent}$

Seventeen oxygen injections of various volumes were injected into the absorbent-packed nitrogen chamber. These injections are shown in figure 6. The gradual increase in the initial pressure over the course of injections was determined to be caused by a small leak in the valves or pressure sensor, however the leak rate is small and has an insignificant influence on these set of results. Figure 7 shows the normalized pressure versus the time elapsed after the injection. After fitting an exponential curve to each normalized injection, we found that the time constant varied slightly with the amount of oxygen injected, as shown in Figure 8.The mean time constant was found to be $\tau_{absorbent}$=34+/-2 seconds for 5ml of oxygen. Extrapolation to steady state conditions (no net oxygen) yields $\tau_{absorbent}$=31+/-2 seconds.

4. Discussion

Results from these experiments yield a $\tau_{absorbent}$ value in-situ of 31+/-2 seconds. The equilibration time for a nitrogen sensor is expected to be much larger than the equilibration time for a GTD due to the increased volume acquired by adding an absorbent chamber. Assuming that the equilibration time for the nitrogen sensor is on the order of a few hours, the residual

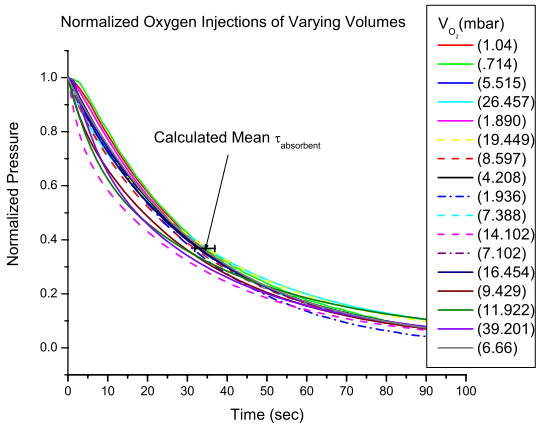

Figure 7. Normalized oxygen injections of varying volumes. The mean time constant was determined to be approximately 34sec+/-2 sec for an oxygen injection volume of 5mbar.

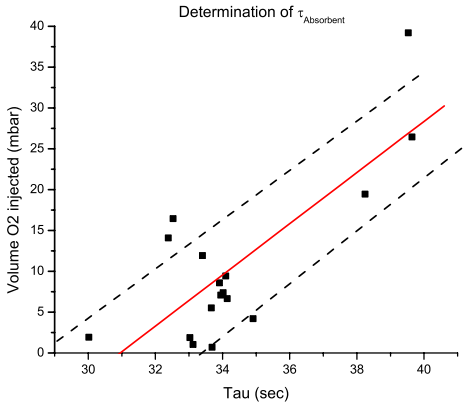

Figure 8. Time constants for the seventeen injections plotted against the injection volume of oxygen. The time constant for equilibrium (no net oxygen) is 31+/-2 seconds.

pressure of oxygen in the sensor can be calculated using equation 3. This yields a residual pressure of oxygen in the nitrogen sensor of $P_{residualO_2}$=0.805mbar. Either increasing the time constant for the nitrogen sensor or decreasing the time constant of the absorbent will decrease the residual pressure of oxygen in the chamber.

The new Pro-Oceanus Systems, Inc. nitrogen sensors are stable to within 0.01% per year, as per manufacturer specifications. This is comparable to the Winkler titration method, which has analytical precision of 0.05% [Knapp, et. al., 1989]. The nitrogen sensors are also more stable than the Sea-Bird Electronics, Inc dissolved oxygen sensor over long deployments, which has a stability of 2% per 1000 hours, or 17.52% per year [http://www.seabird.com].

5. Conclusions

After deployment on the 15th of August, the new RS-232 recording system in a GTD will have been tested. This will pave the way for real-time ultra-stable dissolved gas measurement systems.

The results from tests on the absorbent indicate that it will be possible to build a reliable and useful new dissolved oxygen/nitrogen sensor.

Future work will include refining the chemical composition of the absorbent to absorb oxygen faster, and experimenting with different membrane thickness' to increase the time constant for the nitrogen sensor, which will decrease the total residual pressure of oxygen in the sensor. Long term testing of the absorbent will also be performed. Results of the in-situ oxygen/nitrogen sensor will be intercompared with results from a mass spectrometer. Finally, these new instrument technologies will be employed to collect data for future air-sea gas exchange studies.

Acknowledgments. I would like to thank Craig McNeil for letting me work in his lab this summer. I would like to thank Rob Pockalny and Paul Hall for organizing the SURFO program, and I would like to thank all the SURFOs for a great summer and all the fond memories.

References

Brady, J.E. and J. R. Holum. *Fundamentals of Chemistry, 3rd ed*. John Wiley & Sons, Inc. Canada: 1981, 924.

Knapp, G. P., M. C. Stalcup and R. J. Stanley. 1989. Dissolved Oxygen Measurements in Sea Water at the Woods Hole Oceanographic Institution. WHOI Technical Report, WHOI-89-23, 2.

McNeil, C. L., B. D. Johnson, D. M. Farmer. 1995. *In-situ* Measurement of Dissolved Nitrogen and Oxygen in the Ocean. *Deep-Sea Research*, 42, 819-826.

Weiss, R. F. 1970. On the Solubility of Nitrogen, Oxygen, and Argon in Water and Seawater. *Deep-Sea Research*, 17, 721-735.

[http://adcp.whoi.edu/MV_OBSERVATORY/index.html].

[http://www.seabird.com].

Teleseismic Analysis of Negative Velocity Gradient in the Upper Mantle Transition Zone

Robin Lee Glas[1]

Graduate School of Oceanography, University of Rhode Island, Narragansett, Rhode Island

Abstract. Seismic records from Iceland and the East Pacific Rise show intermittent waveforms indicative of negative velocity gradients within the transition zone of the mantle. A possible explanation for these discontinuities is that they represent segments of ancient, subducted oceanic crust. Above the 660 km discontinuity, the density of subducted oceanic crust, composed mainly of majorite, is greater than that of pyrolite, the commonly accepted mantle composition. However, below the 660km discontinuity, the density of majorite is less than that of the surrounding mantle. Such a density profile may lead to accumulation of subducted oceanic crust at the base of the upper mantle. Throughout the pressures of the transition zone, experimental studies on majorite have shown that the compressional velocity of majorite is significantly less than that of a pyrolite mantle. The observed low velocity areas within the transition zone may then be due to the presence of majorite. To test this hypothesis, it is necessary to observe different regions throughout the world to observe whether or not these discontinuities are consistent throughout the mantle's transition zone. This project has found that the discontinuities in question are, in fact, also existent beneath the Azores Islands and Manitoba, Canada. Results of this study support a model of partial- layered convection of the upper mantle.

1. Introduction

Seismic discontinuities occur in the upper mantle at 410km and 660km in depth. These discontinuities are the result of phase changes from the α to β phase of $(Mg,Fe)_2SiO_4$ for the 410-km discontinuity and from γ $(Mg,Fe)_2SiO_4$ to perovskite plus magnesiowustite at the 660-km discontinuity. This is a result of the density of the mantle as depth increases, dramatically increasing the velocity of P and S waves at 410 and 660 km in depth [Fei, 1999].

The transition zone of the mantle is the region between these two discontinuities. The transition zone consists of a gradual change from the α -phase of $(Mg,Fe)_2SiO_4$ to the β -phase of $(Mg,Fe)_2SiO_4$. Past seismic studies in different regions of the world have imaged this transition zone seismically, and have shown that there exist negative velocity jumps throughout [Shen, 1998a; Shen 1998b; Li 1998; Owens 2000]. These negative velocity gradients within the transition zone could be indicative of "chunks" of another substance aside from the resident mantle spinel. One possible explanation for this is that within the transition zone, there lies ancient, subducted oceanic crust.

Seismic records have shown that the oceanic crust travels deep into the upper mantle, but these recordings cease at the 660-km discontinuity. This may be due to the fact that, as the crust subducts through the upper mantle, the buoyancy of the crust is less than that of the surrounding olivine and spinel. At the 660-km discontinuity, it becomes the opposite. The buoyancy of the crust becomes greater than that of the surrounding perovskite, causing it most likely to stop subducting through the mantle. This would allow for the aforementioned "recycling" within the transition zone [Ringwood, 1994].

At the depths of the transition zone, oceanic crust is composed mainly of majorite, $Mg_3(MgSi)_2Si_3O_{12}$, which has elastic properties consistent with the velocities received in these past data taken of the transition zone. These elastic properties, the bulk and sheer moduli, are incorporated into the two wave equations of velocity of P and S waves. The relationship between velocity (in both cases) and these moduli is a direct one, with a higher velocity corresponding to a higher bulk or sheer modulus. Majorite, in comparison to spinel, has a lower bulk and sheer modulus, implying a lower seismic velocity reading when detected [Anderson, 1989].

The goal of this project is to use teleseismic data recorded from the Azores Islands, and from Manitoba, Canada to answer the question of whether this negative velocity gradient in the transition zone is consistent throughout different regions of the world. The answer to this question is helpful in that it provides more evidence that this could all be from subducted oceanic crust. If, indeed, the crust can reside in the transition zone of the mantle, the nature of mantle convection in general is indicated. With this in mind, these discontinuities would most likely show up according to how the mantle is convecting, being "dragged" along over millions of years with the "currents". Furthermore, mantle plumes would most likely have an effect on the location of the accumulation of majorite, with the upward welling action "catching" or "dragging" the material either partially or completely up to the surface.

2. Data and Methods

The data used in this project (Figure 1) are from the Cha de Macela, Azores station (CMLA), and the Flin Flon, Manitoba, Canada station (FFC), taken from the Incorporated Research Institution for Seismology (IRIS) Data Management Center at the University of Washington. The data consist of events from March of 1996 to March of 2001. Included in the data were events ranging from 5.5Ms to 8.5Ms in magnitude and 10 to 600 km in depth. 176 events were included for CMLA and 75 events were included for FFC, with Figure 2 showing an example of a seismogram received from IRIS. After visual inspection, the data were sliced and rotated, and the radial receiver functions were calculated for each of the events [Cassidy, 1992], an

[1]Now at University of Maine, Orono, ME

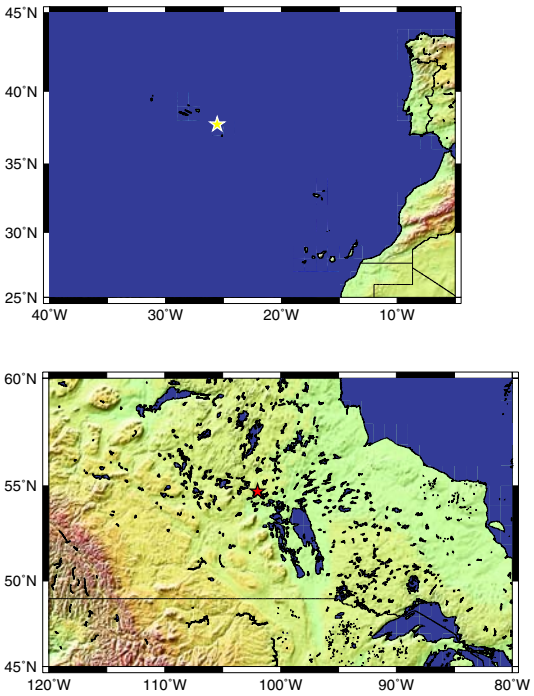

Figure 1. Maps of stations where data were collected. A) Map of Cha deMacela, Portugal site, including the Northwestern coast of Africa, and the Western coast of Spain. (brown star) B) Map of Flin Flon, Manitoba, Canada site. (white star).

example of which is shown in Figure 3. After the radial receiver functions were calculated, the data were stacked using an nth root bootstrap stack (n=2) to maximize the signal to noise ratio [Kanasewich, 1973; Efron, 1983].

3. Results

The data used in this project are from the Cha de Macela, Azores station (CMLA), and the Flin Flon, Manitoba, Canada station (FFC), taken from the Incorporated Research Institution for Seismology (IRIS) Data Management Center at the University of Washington. The data consist of events from March of 1996 to March of 2001. Included in the data were events ranging from 5.5Ms to 8.5Ms in magnitude and 10 to 600 km in depth. 176 events were included for CMLA and 75 events were included for FFC, with Figure 2 showing an example of a seismogram received from IRIS. After visual inspection, the data were sliced and rotated, and the radial receiver functions were calculated for each of the events [Cassidy, 1992], an example of which is shown in Figure 3. After the radial receiver functions were calculated, the data were stacked using an nth root bootstrap stack (n=2) to maximize the signal to noise ratio [Kanasewich, 1973; Efron, 1983].

4. Interpretation

The negative velocity readings for both stations were distinct, with arrival times of about 55s after P for CMLA and about 50 and 60s after P for FFC. The ratio of the negative velocity discontinuity to the 410 at the Cha de Macala is about 1:3 in magnitude. Likewise, this is the case with the 50s negative discontinuity found at the FFC site. According to past lab experiments, at depths of 410 to 450km, both the P and S wave velocities of majorite are consistent with this comparison, with deviations from normal mantle transition zone velocities at about 1/3 the magnitude of the 410-km discontinuity. This corresponds to the readings received at CMLA and FFC. The discontinuity corresponds loosely to past lab studies, showing the difference between mantle transition zone velocities and majorite at depths of 580km to 600km. This difference is about 1/2 to 3/4 the magnitude of the 660-km discontinuity, according to these studies [Anderson, 1989].

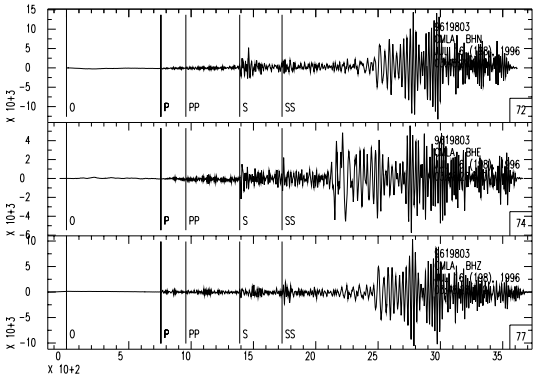

Figure 2. A sample seismogram, containing the horizontal, vertical, and radial components of the event. Labeled are the arrival times for the different wave types in each earthquake. The data for this project were derived by focusing primarily on the arrival times between P and PP.

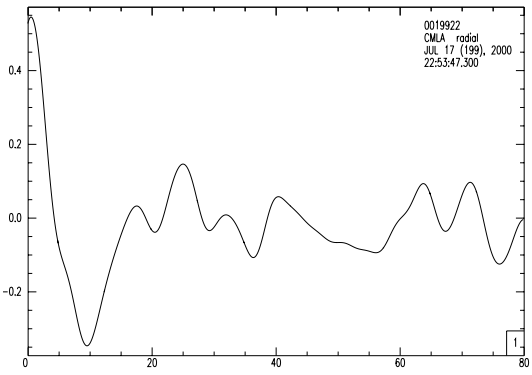

Figure 3. A sample radial receiver function calculated from sliced and rotated seismograms.

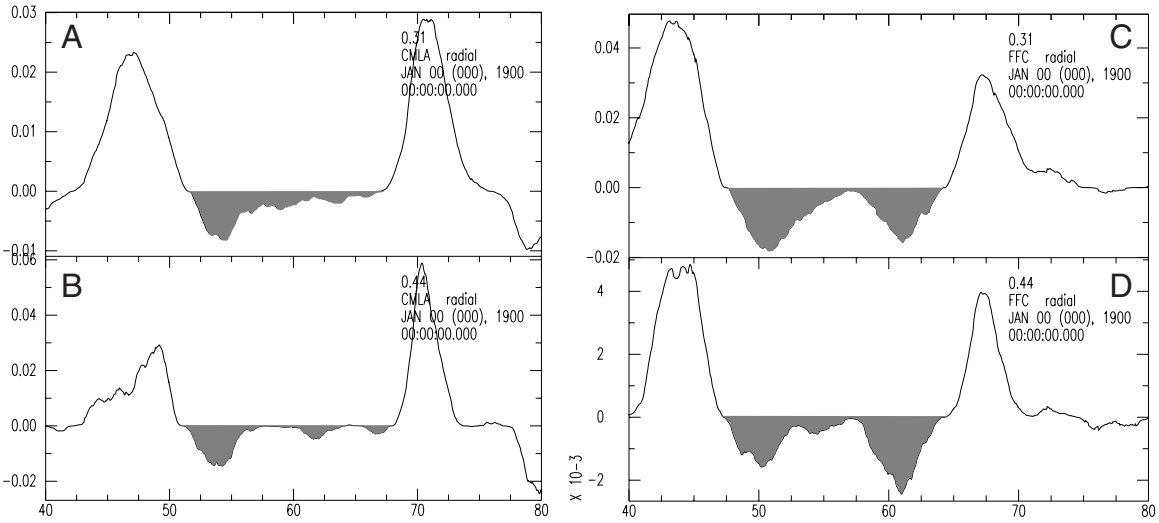

Figure 4. Nth- root stacks of receiver functions for a=0.31and a=0.44 for each station. A) Stacked receiver function with a=0.31 for CMLA. With an a- value of 0.31, the signal-to-noise ratio is higher, clearly displaying a negative velocity discontinuity at about 55 seconds after P. B) At CMLA, the stacked receiver function with an a- value of 0.44 has a much lower signal- to- noise ratio, however, there is still significant P-to-S conversion using this frequency, with the negative velocity discontinuity evident at about 55 seconds after P. C) An a- value of 0.31 for the FFC site, displaying a higher signal- to- noise ratio than for 0.44, with two negative velocity discontinuities at about 50 and 60 seconds after P. D) A lower signal- to- noise ratio was found for the stacked receiver function with an a- value of 0.44 for the FFC site. However, the 410, 660 and negative velocity discontinuities are clear at this frequency as well.

The nature of mantle convection and plumes could possibly have an effect on the location of these negative velocity discontinuities. The Azores islands are known to be the result of an upwelling plume. The location of the negative discontinuity under the Azores is found in the upper transition zone, with a depth of 420 to 450 km. It is possible that this could be the result of the plume dragging the low- velocity substance nearer to the surface. The Manitoba site, however, is not located above a plume. The locations of the two discontinuities here could simply be a result of mantle convection within the transition zone, with the convection cell passing through these discontinuity locations.

4. Conclusion

The data show that the negative velocity gradient in the transition zone is consistently found under the Azores islands, Portugal and Manitoba, Canada. These findings, in conjunction with previously studied areas such as Tanzania, Iceland, the East Pacific Rise, and the Northeastern United States, elude to the possibility that these negative discontinuities could be consistent throughout the world. A plausible explanation for these discontinuities is that they come from ancient, subducted crust, composed of majorite. The data are consistent with the experimental velocities of majorite at pressures corresponding to the depths where the negative discontinuities were found. Furthermore, the locations of the negative velocity discontinuities could likely be influenced by the presence of mantle plumes and the behavior of mantle convection.

Acknowledgments. This project was completed under the close guidance of Yang Shen, with the help of Paul Hall, Rich Viso, Daniel Shaevitz, and Robert Pockalny. I thank these people and the URI's Graduate School of Oceanography. This project supported by NSF Summer Undergraduate Research Fellowship in Oceanography program.

References

Anderson, D. L., Duffy, T. S., Seismic Velocities in Mantle Minerals and the Mineralogy of the Upper Mantle, *Journal of Geophysical Research*, 94, 1895-1912, 1989.

Efron, B., Gong, G., A leisurely Look at the Bootstrap, the Jackknife, and Cross-Validation, *The American Statistician,* 37, 36-48, 1983.

Fei, Y., Bertka, C., Phase Transitions in the Earth's Mantle and Mantle Mineralogy, The Geochemical Society, Special Publication No. 6, 1999.

Hofmann, A. W., White, W. M., Mantle Plumes from Ancient Oceanic Crust, *Earth and Planetary Science Lett.,* 57, 421-436, 1982.

Kanasewich, E. R., Hemmings, C. D., Alpaslan, T., Nth-Root Stack Nonlinear Multichannel Filter, *Geophysics,* 38, 327-338, 1973.

Li, A., Fischer, K., Wysession, M., Clarke, T., Mantle Discontinuities and Temperature under the North American Continental Keel, *Nature*, 395, 160-163, 1998.

Owens, T., Nyblade, A., Gurrola, H., Langston, C., Mantle Transition Zone Structure beneath Tanzania, East Africa, *Geophysical Research Letters,* 27, 827-830, 2000.

Ringwood, A. E., Role of the Transition Zone and 660 km Discontinuity in Mantle Dynamics, *Physics of the Earth and Planetary Interiors*, 86, 5-24, 1994.

Shen, Y., Sheehan, A., Dueker, K., de Groot-Hedlin, C., Gilbert, H., Mantle Discontinuity Structure beneath the Southern East Pacific Rise from P-to-S Converted Phases, *Science*, 280, 1232-1234, 1998.

Shen, Y., Soloman, S., Bjarnason, I., Wolfe, C., Seismic Evidence for a Lower-Mantle Origin of the Iceland Plume, *Nature*, 395, 62-65, 1998.

Tidal Effects on Phytoplankton in the Pettaquamscutt River Estuary

Erin Hodel[1] and Sunshine Menezes

Graduate School of Oceanography, University of Rhode Island, Narragansett, Rhode Island

Abstract. The Pettaquamscutt River Estuary, located in southern Rhode Island, is a diverse ecosystem containing many uncommon planktic organisms. One can distinguish two regions of the river, according to their different geomorphologies. The lower river is dominated by a flood delta and has a shallow depth of approximately two meters with well-mixed water. A sill separates this region from the fjord-like upper river, which consists of two deep kettle lakes with strong pycnoclines. Tidal flushing influences physical, chemical, and biological conditions in the estuary. During the flood, coastal plankton may be carried into the estuary, while during the ebb, plankton (including brackish species) may be washed out to Rhode Island Sound. This project evaluated the effects of this tidal flux on phytoplankton biomass and bacterial abundance via two types of sampling programs along the salinity gradient of the Pettaquamscutt River: a 24-hour station at a specific site on the river, and drogue studies. Water samples were collected during spring tides, when tidal range was greatest due to syzygy, in order to observe maximal tidal effects on planktic organisms. Chlorophyll a was used as a proxy for phytoplankton biomass. Samples were filtered into two size fractions, total phytoplankton and <20 _m phytoplankton, for fluorometric analysis. Bacteria were enumerated as another indicator of planktic tidal input. Relationships between temperature, chlorophyll, bacteria, and salinity were examined. An insignificant inverse relationship was found between temperature and salinity. No significant correlations were found between other variables, yet several trends were noticed and supported findings of previous studies. In addition, drogue studies revealed incoming tidal water velocities for several locations along a 5 kilometer stretch of the estuary.

1. Introduction

Estuaries are semi-enclosed bodies of water connected to the ocean, diluted by a freshwater source (Duxbury, 2001). Because of their free connection to the ocean, estuaries are affected by ocean tides. During the tidal cycle, tidal flushing alters the physical, chemical, and biological conditions of an estuary. Estuarine organisms must be well adapted to cope with these changes.

The Pettaquamscutt River Estuary, located in southern Rhode Island, is a dynamic ecosystem influenced by ocean tides. The Pettaquamscutt River watershed (Figure 1), is 35.5 km2 (Gaines, 1975). The river is approximately nine kilometers long and flows from its freshwater source, Gilbert Stuart Stream, southward to Rhode Island Sound (Sifling, 1997). Effects of tidal flushing are maximal near the mouth of the river with tidal flood volume flux decreasing up-river (Sifling, 1997). The flow dynamics of the river are a function of both tidal inputs and geomorphology.

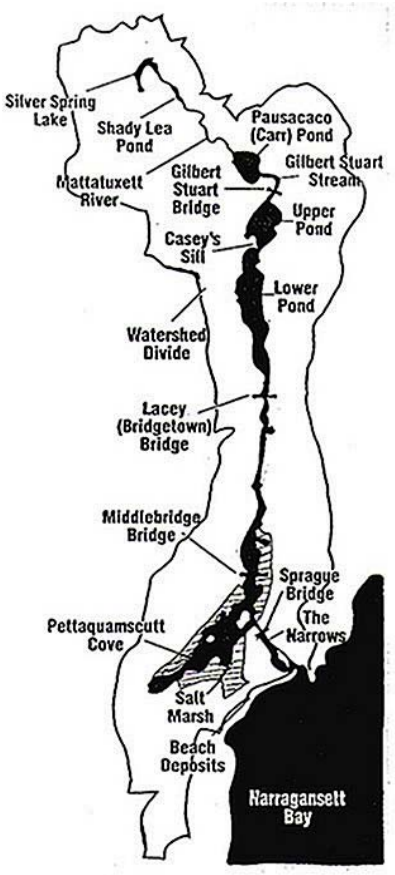

Figure 1. Map View of the Pettaquamscutt River Estuary (Sifling, 1997).

An estuary may be defined either by geomorphology, water circulation, or salinity distribution. The Pettaquamscutt River Estuary is unusual in that it has two distinct regions: the upper and lower river. Each region is characterized by a different geomorphology, which results in a different water circulation pattern and salinity distribution. Receding glaciers were responsible for forming the Pettaquamscutt River and its underlying geomorphology, as illustrated in a longitudinal section in Figure 2. A valley was created in this region during the Tertiary and later deepened by Pleistocene glacial erosion (Gaines, 1975). Meltwater from two large ice blocks at the northern end of the river deposited a sedimentary sequence down-river. The ice blocks formed two deep kettle lakes at the northern end of the river. Water flowed southward, carving meltwater channels and depositing sediments, which accumulated in the lower region. As a result, the lower river is dominated by a flood delta and has a relatively constant,

[1]Now at University of Missouri-Columbia

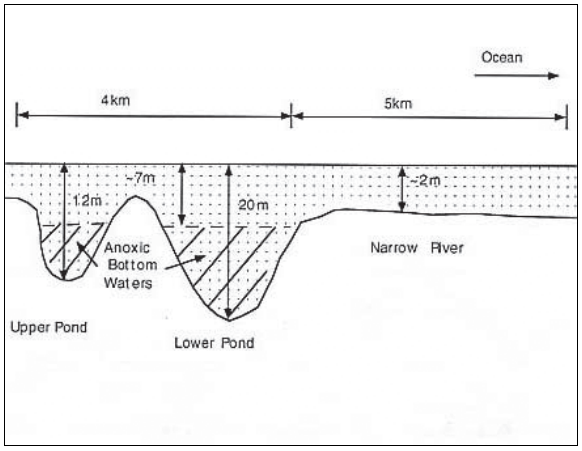

Figure 2. Longitudinal Section of the Pettaquamscutt River (Sifling, 1997).

shallow depth of two meters, on average (Gaines, 1975). In this region of the estuary, mixing of fresh and salt water occurs, giving the river characteristics of a well-mixed estuary. A large, shallow cove is also present at the southern end of the river, which absorbs approximately one-third of the incoming tide (Sifling, 1997).

Glacial meltwater channels connect the lower river to the upper river, which is dominated by two deep kettle lakes, the Lower Pond and Upper Pond, with depths of 19 and 15 m, respectively (Sifling, 1997). The difference in tidal height decreases with distance up the estuary (Gaines, 1975). Therefore, tidal influences are presumed to be less significant in the lakes. Additionally, two shallow sills formed by the ice block depressions hinder flow into this region. These lakes are characteristic of a fjord-type estuary. Each lake has a strong pycnocline resulting from the sinking of incoming seawater, which is colder and more saline, to intermediate depths in the lakes. As a result, water is vertically stratified in three distinct layers: an oxygenated layer approximately 3 meters in depth with an approximate salinity of 5-15 parts per thousand (ppt) depending upon season (Menezes, pers.comm.), a hypoxic layer from approximately 3-5 meters with increased salinity, and a bottom layer with stagnant, anoxic waters and highest salinity (Johnson et al., 1995). The bottom anoxic layer overturns partially every few years (Gaines and Pilson, 1972). Water movement in the shallow waters of the lakes is dominated by advection, and tidal flushing is poor because the sills hinder water flow. However, tidal volume is still more significant than freshwater flux in this region under most weather conditions (Sifling, 1997).

The Pettaquamscutt River Estuary contains a diverse and abundant phytoplankton population (Hargraves, 1991). Some of these planktic organisms are rare and only found in a few locations on Earth (Menezes, 1999). Species have been discovered that were previously unknown in this region (Hargraves, 1991). This study sought to improve our comprehension of the impacts of tidal flux on phytoplankton distribution in the estuary. Like other estuarine organisms, phytoplankton must be tolerant of changes induced by tides on an estuary. During the tidal flood, coastal phytoplankton may be carried into the estuary, while during the ebb tide, phytoplankton, (including brackish species) may be washed out to Rhode Island Sound. This study examined how the tide affects phytoplankton distribution and how the tide progresses up-river.

2. Materials and Methods

The amount of chlorophyll a in water samples was measured in order to approximate phytoplankton biomass. Water samples were collected along the salinity gradient of the river during spring tides, when tidal heights are greatest, in order to observe maximal tidal effects on phytoplankton and also for navigational purposes. Two different sampling methods were employed to assess tidal influence. The first consisted of a 24-hour sampling program at a specific site to determine how chlorophyll and other variables in the estuary change at one location over a tidal cycle. The second employed the use of drogues to measure changes in chlorophyll and other variables in a parcel of water moving up-river with the incoming tide.

2.1. 24-Hour Station

The 24-hour sampling program took place at a site on the river directly under Sprague Bridge, on Route 1A, Narragansett, Rhode Island. This site is located one kilometer from the mouth of the estuary. Depth-integrated samples were collected every two hours over a 24-hour period in order to observe how chlorophyll a concentrations changed at this location over a tidal day. Samples were taken hourly for 3 consecutive hours around high tides. Samples for bacterial abundance were collected as another indicator of tidal plankton input. Depth-integrated temperature and salinity measurements were also taken at all sampling times. Depth-integrated samples were collected with a 2-meter length of plastic pipe and poured into Nalgene bottles. Three replicates for chlorophyll a and two replicates for bacteria were collected along with one sample for salinity and temperature measurements. All sample bottles were rinsed twice prior to sample collection. Samples were placed in a cooler with ice packs and immediately transported to the lab. Temperature was measured in the field using a mercury thermometer. Salinity was determined in the lab using a hand-held Salicon refractometer.

2.1a. Chlorophyll Protocol

Water samples were prefiltered into two size fractions, total and <20 micrometer (μm) phytoplankton (known as nanoplankton) using a 20 μm mesh filter. Twenty-five mL samples from each size fraction of phytoplankton were filtered onto Whatman glass fiber filters using a vacuum filtration system. Filters were removed with forceps, wrapped in aluminum foil, and stored in a freezer for later fluorometric analysis. For this analysis, each filter was placed in a glass culture

tube containing 7 mL of 90% acetone and stored in a refrigerator overnight to extract chlorophyll a. The following day chlorophyll a concentration from each sample was measured using a Turner fluorometer.

2.1b. Bacteria Protocol

Bacterial abundance was determined by the direct count assay method (Hobbie et. al., 1977 and Kirchman, 1982). Two mL bacterial samples were fixed in a 2.2% glutaraldehyde solution to preserve cells. Sixty _L of Tween 80 was added to samples to aid cell separation before they were each sonicated for 30 seconds to dissociate particle-bound cells. Each sample was stained with 40 _L of the fluorescent dye, DAPI (4', 6-diamidino-2-phenylindole) for 10 minutes and then filtered onto 0.2 _m polycarbonate filters prestained with Irgalan Black. Filters were mounted on glass microscope slides using Cargille Type DF immersion oil. One filter was prepared from each of two replicate samples. Using an epifluorescence microscope, bacteria were enumerated by randomly selecting 15 microscope fields and counting the number of cells in each. From this an average number of cells per filter was determined.

2.2. Drogue Studies

Drogue studies were employed to observe changes within a parcel of incoming tidal water, (most notably chlorophyll a) and to determine how far up-river the tidal wave would travel. Three drogues were assembled, each consisting of rubber stoppers, a trawl net ball, a 3-pound dive weight, rope, and two pieces of plywood which formed a symmetrical cross shape with a 40 centimeter width. The total height of the drogue was 75 centimeters (Figure 3). This construction allowed for only the top half of the flotation device (the trawl net ball) to float above the water surface, minimizing possible wind effects. A hand-held waterproof E-Trex global positioning system (GPS) device was attached to the top of one of the drogues and used to measure position and water velocity.

Drogues were released from a boat at a site just north of Sprague Bridge a few minutes prior to the time of high tide at Sprague Bridge and were subsequently followed by boat as they traveled up-river. The three drogues followed a similar path and generally stayed together. Water samples were collected for chlorophyll a, salinity and temperature from the side of the boat near whichever drogue was located in the middle of the three. Samples were taken every 20-30 minutes depending on the location in the river. Samples were taken every 30 minutes in areas of slower water movement and every 20 minutes in areas of greater velocities. Samples for chlorophyll a were filtered in the field onto Whatman glass fiber filters using a plastic filter cartridge, then wrapped in aluminum foil, and stored in a cooler on ice for later fluorometric analysis. Temperature and salinity measurements were taken in the same manner as described for the 24-hour station. Two more drogue studies were performed on different days in order to collect data for locations farther north.

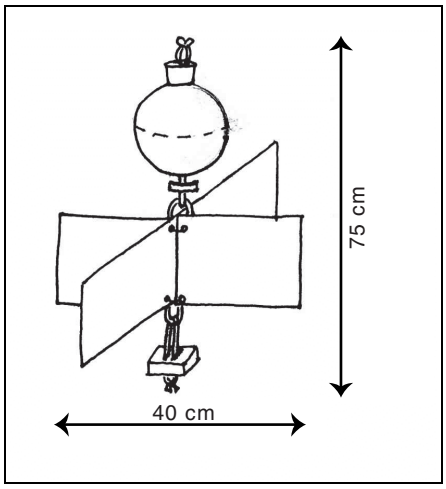

Figure 3. Model of drogue.

3. Results

3.1. 24-Hour Station

Each variable from the 24-hour station was graphed against time and compared to the tidal cycle. Salinity measurements were used as a proxy for tidal stage. No significant patterns were apparent between salinity and each of the variables with linear regressions. Linear regressions for temperature versus each variable were also found to be insignificant. Therefore each variable was broken into four different time blocks according to tidal stage (high tide, low tide, high high tide, and low low tide). Both least squares regression and Spearman Rank Correlation were performed on each time block for both salinity and temperature in comparison to each variable. No significant correlations were found. An inverse relationship was found between temperature and salinity. Salinity was found to increase as temperature decreases (Figure 4), indicating colder, and more saline ocean water coming into the estuary during tidal flood.

An overall increase in both size fractions of chlorophyll a is apparent (Figure 5). This may be attributed to a larger volume of water present later in the tidal day due to a higher second high tide in the 24-hour sampling period. The first high tide had a tidal height of approximately 1.2 meters while the second had a height of approximately 1.5 m. Therefore, increased phytoplankton biomass may simply be a result of more oceanic water entering the estuary. Another possible explanation for this increase is that it is part of a larger cycle of phytoplankton abundance, which spans a time frame longer than 24 hours, with a cyclic pattern not discernable from this study. Chlorophyll a measurements were variable in this study; however this is most likely due to the patchy nature of phytoplankton in the environment. Macro-algae present in the water at this station may have also contributed to error in assessing true phytoplankton biomass.

Bacterial abundance was measured as an independent gauge of planktic tidal input. Measurements for bacterial abundance also proved to be variable (Figure 6), which again may be attributed to patchiness of

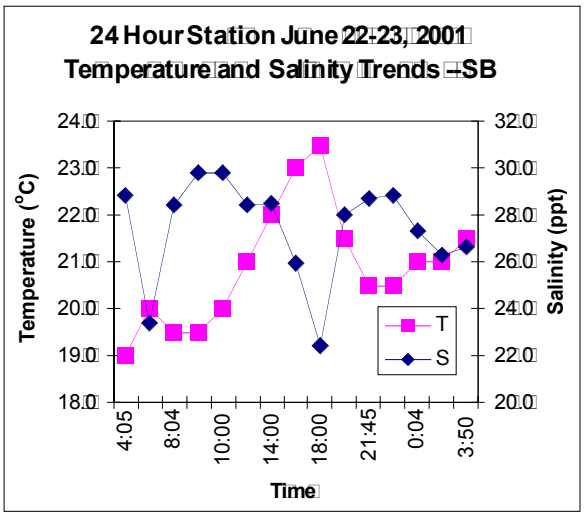

Figure 4. Temperature and Salinity Trends for 24-hour station.

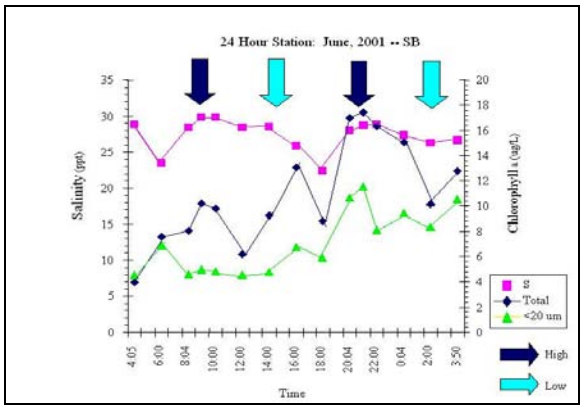

Figure 5. Chlorophyll *a* and Salinity Trends for 24-hour station.

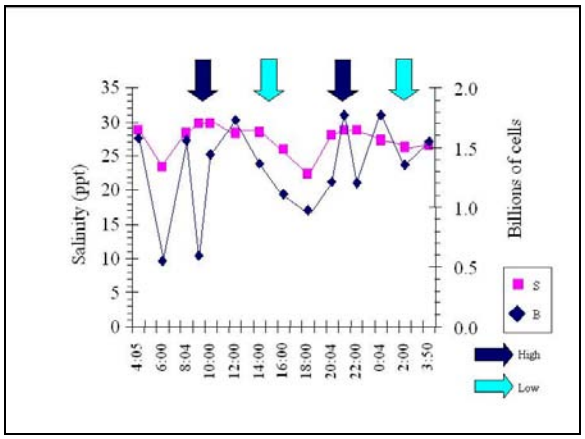

Figure 6. Salinity and Bacterial Abundance Trends from 24-hour station.

bacteria (Shiah and Ducklow, 1995). The average abundance was 1.3 billion cells per liter. Bacteria and phytoplankton were not significantly correlated. Previous studies have confirmed significant correlations between bacterial abundance and phytoplankton (Shiah and Ducklow, 1995). However, these studies were performed on larger time scales than ours. Therefore, it is not surprising that no correlation was found given the small time scale of 24 hours in this study.

Chlorophyll a data from this study were compared to that from a previous 24-hour study at a different location on the Pettaquamscutt River. The older study took place in 1999 at the same time of year, using the same methodology, at a site located near Lacey Bridge, approximately 4.3 km north of the mouth, or approximately 3.3 km north of the Sprague Bridge (Figure 1). Total chlorophyll a concentrations with

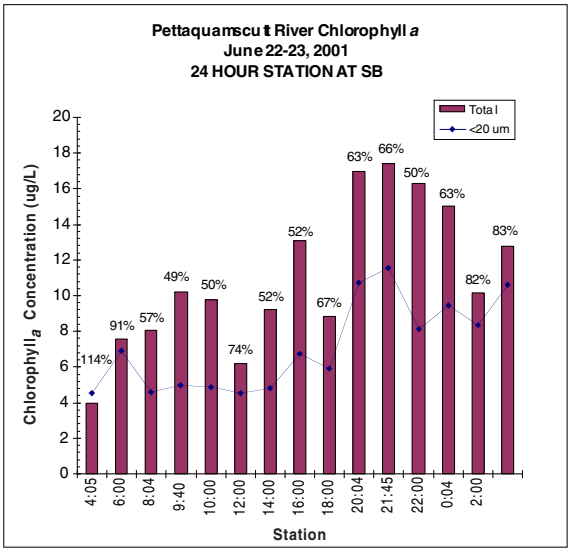

Figure 7. Total and <20 µm Chlorophyll *a* Trends from 24-hour station at Sprague Bridge.

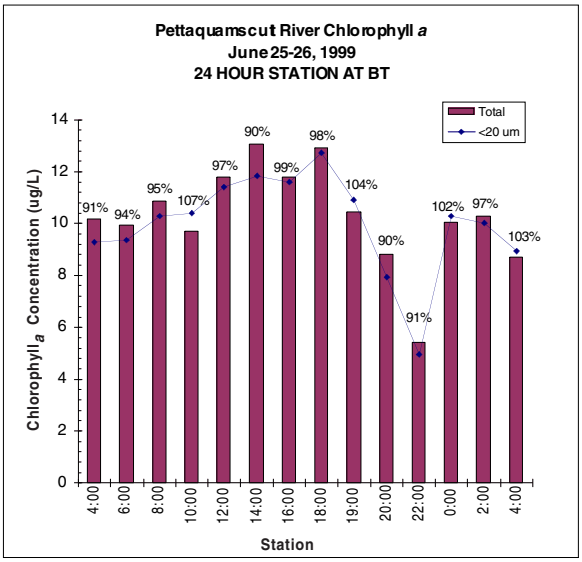

Figure 8. Total and <20 µm Chlorophyll *a* Trends from 24-hour station at Bridge Town Bridge.

respective <20 _m percentages from each study are shown in Figure 7 and Figure 8. Total chlorophyll from the Sprague Bridge site shows a general increase while that from the Bridgetown site remains relatively constant over 24 hours. In addition, values from Sprague Bridge are more variable. Therefore, based upon these studies, it appears that variability in phytoplankton biomass may decrease with increasing distance from the ocean, as tidal effects dampen. Average values of the <20 _m percentage of total phytoplankton were 68% at Sprague Bridge and 97% at Bridgetown, showing the percentage of nanoplankton in total phytoplankton to increase up-river. This is a typical trend based on unpublished data from the Pettaquamscutt River (Menezes, pers. comm.).

3.1. Drogue Studies

Results from two of three drogue studies were analyzed, showing variable water velocities in the river depending on location. A second drogue study became necessary after drogues did not travel as far north as anticipated in the first drogue study. In the first study, we speculate that the drogues floated out of the main current of the incoming tide and became trapped in an eddy-like flow. Due to this, the drogues fell behind the incoming tide. When they were finally placed back in the main channel of the estuary, there was not enough tidal energy to push them forward, since the main bulk of the high tide had already passed. Therefore, a second drogue study was needed in order to compile data representing a larger stretch of the river, and also as an attempt to reach the northern end of the estuary. The second drogue study was started at the end point of the first. During this study, drogues floated to the middle of the Lower Pond and then changed direction and floated southward. A third drogue study was performed in a final attempt to reach the southern end of Gilbert Stuart Stream, which is the northern end of the estuary. Drogues were released at a location just south of the entrance to the Lower Pond, near Lacey Bridge, well in advance of high tide, in hopes of the incoming high tide carrying the drogues to the north end of the Upper Pond. In spite of this, the drogues still did not move past the middle of the Lower Pond. Although seawater reaches the northernmost part of the Upper Pond, it sinks due to temperature and salinity differences into the deep basins of the kettle lakes. This probably hindered movement of the drogues into the northernmost region of the river. Lengths of the drogues extended to less than one meter deep in the water column and therefore were incapable of being carried by the deep currents in the lakes. We can therefore reason the incoming tidal current sinks considerably by the time it reaches the middle of the Lower Pond. Consequently drogues were no longer capable of moving with the incoming tidal water past this location. Water velocities were shown to be variable in the river depending on location (Table 1).

Salinity and temperature displayed the same inverse relationship as the 24-hour station. Salinity decreased and temperature increased with increasing distance from the ocean. Chlorophyll a measurements remained relatively consistent with increasing distance up-river, indicating that drogues were likely representing the same parcel of water as it traveled northward (Figure 9). Both T-tests and Wilcoxin Rank Sums confirmed no significant difference in chlorophyll a values for the same day. Velocities for various legs of a 5 km stretch of the river were calculated from distance and time (Table 1). Distances between sampling locations were recorded by the GPS and the times between them were obtained from field notes due to a problem encountered with the time stamp on the GPS device. Water velocities varied according to location in the river. Water velocity decreased in the middle of the Lower Pond, which was the northernmost point reached by the drogues.

4. Discussion

This study did not elicit significant correlation between chlorophyll a (phytoplankton biomass) and tidal stage, which was the original objective of the project. Additionally, no significant correlations were important to note the small time scale of the study. This

Location	Distance(m)	Time (s)	Velocity (cm/s)
Sprague to Middle Bridge	944.43	7860	12.02
Middle Bridge to middle of narrow stretch	922.00	2400	38.42
middle of narrow stretch to end of narrow stretch	801.29	1200	66.77
Marsh to Bridge Town	573.59	840	68.28
Bridge Town to Lower Pond	654.42	1560	41.95
Lower Lower Pond	318.25	720	44.20
Mid Lower Pond	129.23	660	19.58
Mid Lower Pond	149.40	684	21.84
Mid Lower Pond	116.74	566	20.62

Table 1. GPS Data showing velocities for different sections of the estuary.

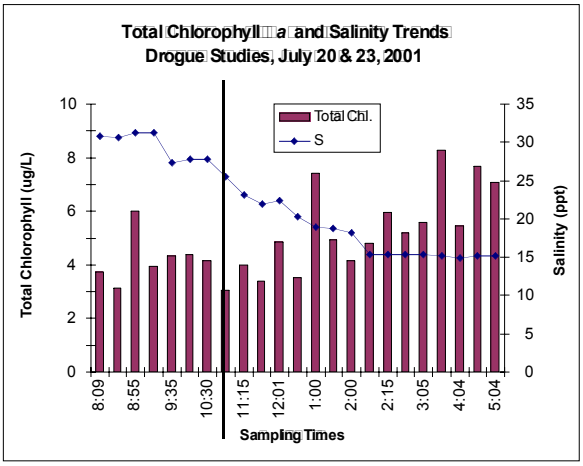

Figure 8. Total chlorophyll *a* values and salinity for two

found between the majority of variables tested. Yet it is may have accounted for the fact that many correlations between variables showed no significance when tested. separate drogue studies on different days. A black, vertical line separates the day. Perhaps this study lacked enough data points, especially for the 24-hour station, to reveal statistical significance. It is likely that chlorophyll a and bacterial data from several consecutive days would have proven to be more telling. However, with only two researchers performing this study and the given the methodology used, obtaining samples for longer than 24 consecutive hours proved to be very difficult. Had more researchers been involved, more data collection would have been possible.

Despite these limitations, several important conclusions can be made from this research. Temperature and salinity showed an inverse relationship, exhibiting the fact that the incoming tide brings colder, more saline water into the estuary. Variability of salinity and temperature measurements decrease with increasing distance from the ocean, indicating that tidal effects are increasingly dampened up-river. Chlorophyll a values from two separate 24-hour station data sets show that percentages of nanoplankton in total phytoplankton increase up-river, which implicates varying phytoplankton community structures in different parts of the river.

The design of the drogues worked well for this project and the methods employed in the drogue studies were successful up to the middle of the Lower Pond, where water velocity slowed down considerably due to hydrodynamics in this region. These studies also demonstrated the path of the incoming tidal current to be complex and variable, depending on the location in the river, supporting previous studies in 1997 by Sifling. Differences in water velocities at various locations were expected due to differences in both geomorphology and biota along the river. Macrophytes along the littoral region of the river are capable of slowing water flow. This was noticed in our study along marshy regions of the river, which tended to be wide and shallow. Narrow regions were shown to have increased water velocities as expected due to a bottleneck effect.

References

B Duxbury, A. C., A. B. Duxbury, and K. A. Sverdrup. 2000. An Introduction to the World's Oceans. McGraw Hill. Boston.

Gaines, A.G. 1975. Papers on Geomorphology, Hydrology, and Geochemistry of the Pettaquamscutt River Estuary. Ph. D. Thesis. University of Rhode Island, Kingston.

Gaines, A.G. and M.E.Q. Pilson. 1972. Anoxic waters in the Pettaquamscutt River.
Limnology and Oceanography. 17(1): 42-49.

Hargraves, P. E., 1991. Narrow River Phytoplankton. Maritimes. 38(2): 6-7.

Hobbie, J.E., R.J. Daley and S. Jasper, 1977. Use of nuclepore filters for counting bacteria by epifluorescence microscopy. Applied Environmental Microbiology. 33: 1225-1228.

Johnson, P.W., P.L. Donaghay, E.B. Small and J. McN. Sieburth. 1995. Ultrastructure and ecology of Perispira ovum (Ciliophora: Litostomatae): An aerobic, planktonic ciliate that sequesters the chloroplasts, mitochondria, and paramylon of Euglena proxima in a micro-oxic habitat. Journal of Eukaryotic Microbiology. 42(3): 323-335.

Kirchman, D. 1982. Statistical Analysis of the Direct Count Method for Enumerating Bacteria. Applied and Environmental Microbiology. 44(2): 376-382.

Menezes, S. 1999. Biodiversity in the Pettaquamscutt River Estuary. Maritimes. 41(4): 10-12.

Shiah, F. and H. W. Ducklow. 1995. Multiscale Variability in Bacterioplankton Abundance, Production, and Specific Growth Rate in a Temperate Salt-Marsh Tidal Creek. Limnology and Oceanography. 40(1): 55-66.

Sifling, J. 1997. Observational Experiments on the Hydrodynamics of the Narrow River Estuary Using and Acoustic Doppler Current Profiler. MS. Thesis. University of Rhode Island, Narragansett.

Adaptation of a Reduced Gas Analyzer for Detection of Molecular Hydrogen and Carbon Monoxide in Seawater

SURFO David Katz[1]

Graduate School of Oceanography, University of Rhode Island, Narragansett, Rhode Island

Abstract. Molecular hydrogen (H_2) and Carbon monoxide (CO) are important atmospheric trace gases. Although often unconsidered by atmospheric and marine alike, these gases are involved in complex environmental processes. Using the HgO method of detection, H_2 and CO can be detected at 10 and 1 ppb levels respectively. This method was used to determine H_2 and CO gas concentrations of the near surface water layer of Narragansett Bay.

1. Introduction

Both molecular hydrogen and carbon monoxide are produced and consumed in photochemical and biochemical reactions. H_2 and CO are important trace gases because of their reaction potential in the atmosphere. Although often overlooked, these gases are involved in complex environmental processes.

The properties of hydrogen allow it to store and release small amounts of energy. Molecular hydrogen is produced or consumed by selected varieties of archea, prokaryotes, and eukaryotes in several different types of reactions. It is a major currency among bacteria in anoxic sediments. With this in mind, hydrogen concentrations in anoxic sediments yield a result of microbial productivity in these sediments (Bryant et al, Scranton et al). Some H_2 escapes the porewater and eventually finds its way into the atmosphere, but the majority of it is taken up and used in the reduction of other compounds by microbes (Lovely et al (1989)), Lovely and Philips (1987)). Hydrogen is also produced by green algae under anoxic photosynthetic conditions (Gaffron (1942)). Carbon monoxide is produced photochemically from humic matter, and by some macroalgae for use in the air sacs that help them float. CO is also produced by siphonophores and coelenterates (Pilson (1988)). H_2 and CO can also originate from the burning of biomass fuel sources.

At the beginning of Summer 2001, our initial study was to collect and analyze atmospheric samples from the roof of the Center for Atmospheric Chemistry Sciences at the University of Rhode Island Graduate School of Oceanography, and from atmospheric samples we intended this method to be used for detection of the gases in the porewater and near surface water layers of Narragansett Bay and the Pettaquamscutt River. The Pettaquamscutt is a unique estuarine system with clear separation between the top layer of oxygenated freshwater and the lower layer of anoxic seawater. However, due to time constraints and instrument difficulties on several occasions, only samples from Narragansett Bay surface water were taken.

[1]Now at SUNY *College of Environmental Science - Forestry*

2. Methods

2.1. Sampling

Samples of surface seawater were taken on August 9, 2001 from the URI's Narragansett Bay Campus pier. The R/V Endeavor was docked there on the east side of the sampling area. The weather on 8-9-2001 was a bright, sunny, summer day with a maximum air temperature of 36ºC and very few clouds. The samples were collected in a 0.5 liter sparge bottle, covered and sealed to prevent gas exchange after sampling. The seawater sample was then returned to the lab and connected to a flow controller 50 sccm of N_2 was bubbled through the seawater in the sparge bottle. New samples of water were taken from the same location on the pier at 2-hour intervals, and the gases were detected using the same method.

2.2. Detection of Molecular Hydrogen and Carbon Monoxide

Molecular hydrogen and carbon monoxide were analyzed using a Model RGA3 Trace Analytical Reduction Gas Analyzer. The headspaces of the sparging bottles were connected directly to the sample inlet of the RGA3 (Figure 1). Gas samples were separated by a heated column (105ºC) and passed to the detector. The detector of the instrument oxidizes reduced gases by flowing them over a heated mercuric oxide bed (265ºC). Mercury gas is left behind, and excited by a mercury vapor lamp, providing sensitive detection in parts per billion quantities (O'Hara and Singh). CO has a detection limit of <1 ppb and H_2 has a detection limit of <10 ppb. These levels are contingent on the background detector noise. Data from the RGA3 was collected using a Scientific Software Inc. SS420x external device and processed with EZChrom Elite software.

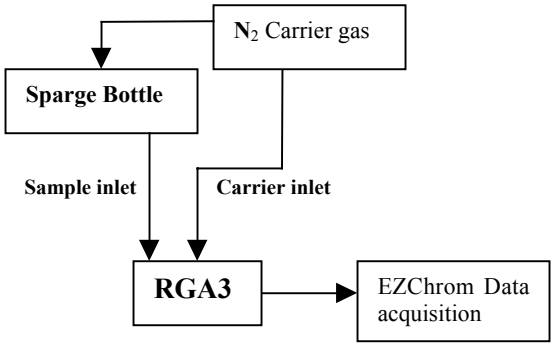

Figure 1. Diagram of the sampling setup. Carrier gas was bubbled through the seawater in the sparge bottle to strip out the gases. The headspace gases are then sent to the RGA3 for analysis.

2.3. Calibration

A flow controller dilution system was constructed for the dilution of gas standards of H_2 (50 ± 5% ppm) in Ultrapure Air and CO (4.88 ± 0.1 ppm) in Ultrapure Air as blended by Scott-Marin Inc. Four model 1159B MKS Flow controllers, associated with a model 247C MKS 4-channel readout, were used in the dilution system. Each Flow controller was calibrated by a Gillian Instrument Corp. *Gilbrator* bubble flow meter. CO was run on a controller at channel 1 with a 50 sccm maximum flow rate, H_2 in Air was flow controlled by a 100 sccm maximum flow rate on channel 2. The gas standards were diluted with UP Air flowing at a maximum possible rate of 5000 sccm on channel 3 and 500 sccm maximum flow rate on channel 4 (Figure 2). These gases were flowed through separate stainless-steel 1/8 inch O.D. tubing to individual Swagelok Toggle Valves (SS-OGS2). The diluted standards were then piped to the sample inlet at a flow rate under 125 sccm. This dilution system was then used for calibration of the RGA3 signal at known concentrations.

3. Results and Discussion

3.1. Data Collection

Over the course of a two-hour series of injections, both gases were effectively stripped out of solution within the first three to four injections (Figure 3). The amount of gases calculated could be lower than the actual concentration of these gases in seawater as a result of continuous carrier flow through the sparge bottle between and during injections.

The changes in H_2 and CO concentrations for the samples collected on 8-9-2001 are presented in Figure 4. Both carbon monoxide and hydrogen seem to follow the buildup of compounds reacting photochemically or biochemically during first light. The slight delay from sunup might be due to the R/V Endeavor may have blocked the first rays of light striking the sampling area due to its position on the eastern side of the sampling area. A sharp decrease in production of both H_2 and CO followed immediately after the first peak of production. A slow buildup of production levels then followed throughout the day. A maximum peak in both H_2 and CO production occurred during the 5:00 PM (EDT) sample. A sharp decrease in production then occurred between 5:00 and 7:00 PM. The drops in production after 7:00 AM and 5:00 PM are of unknown cause at this point. Some sunlight was still striking the target area directly. Also unknown is the mechanism, whether photochemical or biochemical by which these molecules are produced. The amount of sunlight seems to have an impact on the production of H_2 and CO during daylight hours. The effects of the tidal forces may have some implications on the amount of each gas produced, but these are as yet undetermined.

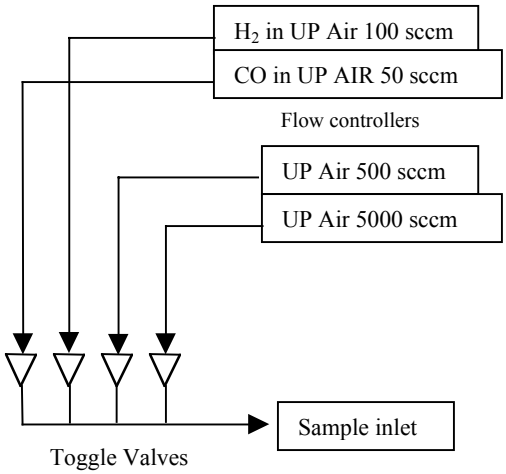

Figure 2. Diagram of dilution system for calibrations of the RGA3 analyzer. Flow controllers are shown with their maximum flow rates. Gases are sent through stainless steel tubing to toggle valves, and are mixed together in the line after the valves on the way to the sample inlet.

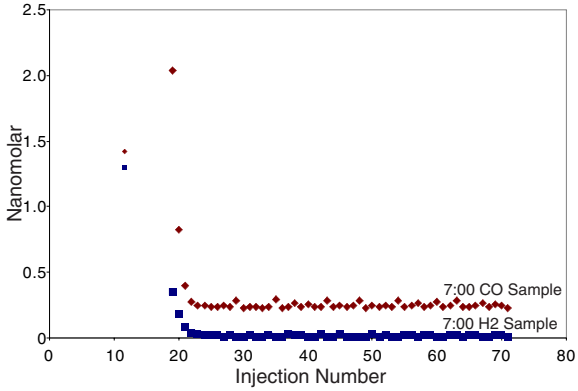

Figure 3. The stripping of CO and H_2 from seawater by N_2. This series of injections were of a sample collected at 7:00 AM 8-9-2001. Injections took place every two minutes over a two-hour period.

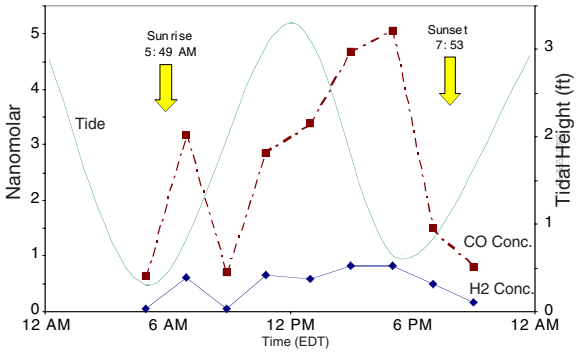

Figure 4. The change in seawater concentrations of H_2 and CO over one day of sampling. Sampling day consisted of 16 hours of sampling on 8-9-2001. Tide movements for the day along with sunrise and sunset times have also been shown.

Only one day of samples was collected for this study due to the instrumental difficulties. More samples from other locations, both in Narragansett Bay and in the Pettaquamscutt River are needed before any conclusions may be drawn.

Acknowledgments. I would like to thank my advisor Brian Heikes for all of his help and support this summer, without which this project would never have gotten off the ground. Rich Sweetman for his help in the laboratory, Matt Chavez for his electrical engineering work, Eddie Roggenstein and Art Spivak for the loan of sparge bottles and ideas, as well as David Smith and Steven D'Hondt for their perspectives on this work.

References

Bryant, M.P., Wolin, E.A., Wolin, M.J., and Wolfe, R.S. (1967) Methanobacillus omelianskii, a syntrphic association of two species of bacteria. Arch. Micro. **59**:20-31.

Gaffron, H., Rubin, J. (1942) Fermentative and photochemical production of hydrogen in algae. J. Gen. Physiol. **26**:219-240.

Lovely, D.R., Phillips, E.J.P. (1987) Competitive mechanisms for inhibition of sulfate reduction and methane production in the zone of ferric iron reduction in sediments. Appl. Environ. Microbiol. **53**:2636-2641.

Lovely, D.R., Phillips, E.J.P., Lonergan, D.J., (1989) Hydrogen and formate oxidation coupled to dissimilatory reduction of iron or manganese by *Alteromonas putrefaciens*. Appl. Environ. Microbiol. **55**:700-706.

O'Hara, D. and Singh, H.B. (1988) Sensitive gas chromatographic detection of acetaldehde and acetone using a reduction gas detector. *Atmospheric Environment* **22**, 2613-2615.

Pilson, M.E.Q., (1998) An introduction to the chemistry of the sea. Prentice Hall.

Scranton, M.I., Novelli, P.C., Michaels, A., Horrigan, S.G., Carpenter, E.J. (1987) Hydrogen production and nitrogen fixation by *Oscillatoria thiebautii* during in situ incuations. Limnol. Oceanogr. **32**:998-1006.

Laboratory modeling of mantle plume dispersion at a segmented ridge

Marcie Kerneklian[1]

Graduate School of Oceanography, University of Rhode Island, Narragansett, Rhode Island

Abstract. Plate-driven and buoyancy-driven flow in the mantle are responsible for many of the volcanic features observed in ocean basins. Geochemical and geophysical studies suggest that at some locations (i.e. Iceland, Galapagos) these two modes may interact. Direct observation of such processes is not possible, therefore theory and modeling provide the best approaches to investigating mantle flow in these locations. This study uses physical models of mantle plume-oceanic spreading center interactions to better constrain the flow processes responsible for observed plume dispersal patterns along spreading ridges. Experiments conducted with isoviscous fluids indicate that waist width (distance along axis to which the plume signal spreads) is a function of spreading rate. The present work increases the complexity of the experiments by utilizing the temperature dependence of the working fluid's viscosity to simulate a rheological boundary layer (RBL) at the base of the lithosphere. Cooling the surface of the fluid creates a sloping rheological boundary layer. Experiments which incorporate this layer were conducted to observe the effects of this layer on the dispersion of the plume. Two unexpected results are reported. First the presence of the RBL decreases along axis dispersion of the plume relative to experiments with no sloping RBL. Secondly, enhanced cooling was observed along the ridge axis at transform offset boundaries.

1. Introduction

Ridge spreading and mantle plumes, the two forms of crustal accretion, are the modes responsible for material transport and thermal fluxing in the mantle. It is known that ridges and plumes interact, but the physical character of the interaction is not well understood [*Kincaid* et al., 1995]. Schilling [1985] documented geochemical anomalies along ridge axes suggesting plumes can flow along the base of the lithosphere and communicate with a nearby spreading center (Figure 1). Modeling of off-axis plumes have indicated that physical interaction of the plume and a single spreading ridge is possible [*Kincaid* et al., 1996a]. The dispersal of on-axis plumes has been modeled for various combinations of plate velocity and plume flux both physically *[Feighner and Richards*, 1995] and numerically [*Ribe* et al, 1995]. These models fail to take into account the presence of a rheological boundary layer corresponding to the base of the lithosphere, or offsets of the spreading ridge due to transform faults. The addition of a sloping RBL is a more realistic representation of the Earth and might significantly alter the dispersal pattern of a plume. Intuitively, one would expect the addition of a boundary layer which slopes away from the ridge axis to enhance along axis flow. Because of this, experiments conducted without a RBL can not be considered accurate models of the Earth.

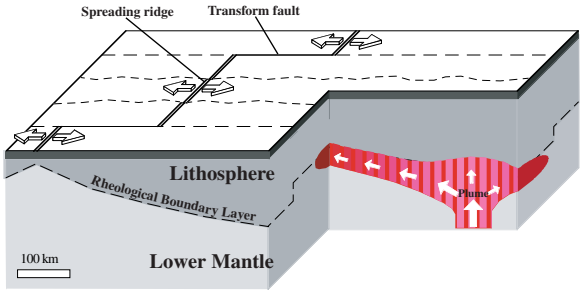

Figure 1: Model of dispersion of an off-axis plume. Plume material may spread along lithosphere-lower mantle boundary and surface at ridge axis.

Accounting only for a single spreading center fails to consider ridge offsets by transform faults. Douglass et al. [1999] found an example suggesting that an on-axis plume crossed a fracture zone, but the fracture zone may not have been active. Rear [1999] investigated experimentally the feasibility of plume dispersal across a transform fault and found it possible at very slow plate velocities (approximately 1 cm per year). Recent tomographic studies by Van Avedonk et al [2001] have demonstrated that cooler temperatures exist below transform faults relative to adjacent ridge axes. The cooler temperatures across the transform may serve as a barrier to flow, and it is not known whether an active transform fault would allow plume material to disperse along the offset.

The origin of the Ontong Java and Manihiki Plateaus (Figure 2) is in many ways unclear. While similar in age it is currently unknown if the formation of the plateaus is related. Back tracing of the Louisville Seamounts correlates formation of the seamount chain to the same plume that formed the Ontong-Java Plateau. No associated seamount chain exists for the Manihiki Plateau. It has been proposed that the plateaus formed from the same plume. A fracture zone between the two plateaus may have allowed the main plume head to form the Ontong Java Plateau, while excess plume material flowed along the fracture zone to form the Manihiki Plateau. The viability of this theory can be constrained by investigating plume dispersion in the vicinity of offset spreading ridges. The relevant conceptual model is a spreading center with a sloping RBL, below which is an on-axis plume (Figure 3).

Tank experiments with and without a RBL were conducted for the case of an on-axis plume to determine the along axis dispersion of plumes for various plume fluxes and plate velocities. The results, presented here, will investigate the following: 1) the dispersal of plume material along a segmented ridge with a rheological boundary layer, and 2) the effect of a RBL at a transform.

[1]Now at your Binghamton University, Binghamton, New York

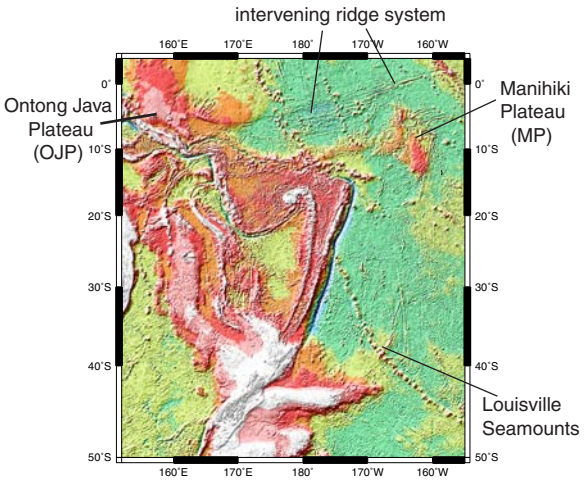

Figure 2: Ontong Java and Manihiki plateaus. Is it possible for material from the formation of Ontong Java plateau to disperse along the intervening ridge system to form the Manihiki Plateau?

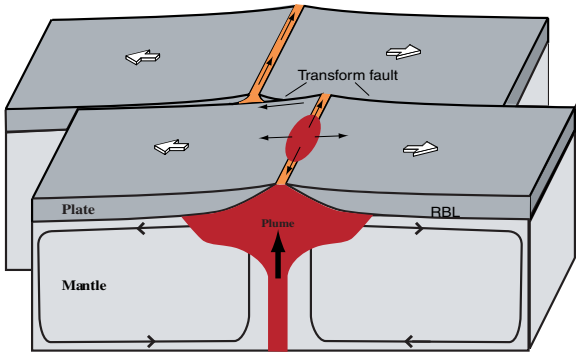

Figure 3: On-axis plume with a segmented spreading ridge and a slopiing rheological boundary layer

2. Methods

Experiments were conducted using a tank apparatus to simulate plume-ridge interaction. The apparatus consisted of an insulated tank containing concentrated sucrose solution with a lexan support structure configured to simulate a ridge-transform-ridge plate geometry placed above the sucrose solution (Figure 4). The tank dimensions were 96X72 cm and was filled with concentrated sucrose solution to a depth of 15.5 cm (Table 1 has tank parameters). The lexan support structure simulates a segmented spreading center geometry with two spreading ridges separated by a 5-cm transform fault. Two mylar sheets per ridge axis were pulled through the ridge bars and along the surface of the fluid to the other end of the tank. Heating elements and scrapers uncoupled the fluid from the mylar sheets, allowing the mylar to be wound around take up reels. Cooling plates suspended 1 cm above the mylar sheets were kept filled with frozen carbon dioxide (dry ice) to cool the working fluid below the mylar. The cooling

Table 1: Experimental apparatus parameters

Parameter	Value
Length	96 cm
Width	17 cm
Fluid Depth	15.5 cm
Heater Diameter	7.5 cm

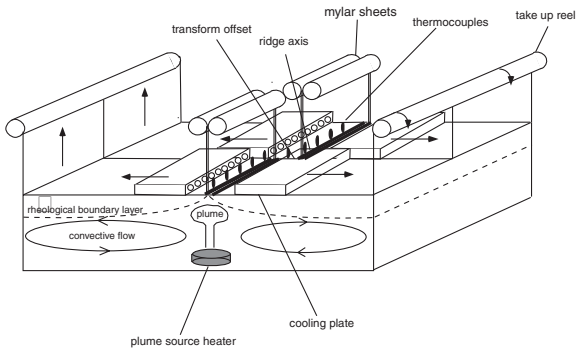

Figure 4: The experimental apparatus.

plates had holes along the ridge axis and transform, which allowed the carbon dioxide gas to sublimate and spill onto the mylar to form a cooled layer of sucrose solution. The concentrated sucrose solution had a temperature dependent viscosity described by [*Kincaid* et al.,1996b]:

$$\mu = e^{\left(\frac{1888}{T+93.3} - 11.48\right)}$$

where μ is viscosity in Pascal seconds, and T is temperature in degrees Celsius. It is an Arrhenius law, where viscosity increases exponentially with the inverse of temperature. Cooling the upper surface to 10°C results in a viscosity change on the order of 11(i.e. $\mu=11\mu_o$) relative to fluid at ambient room temperature, producing a boundary layer. The temperature dependence of the fluid also allowed for plume formation when heated.

A vertical temperature profile was taken using thermocouples mounted on a rod and placed in the fluid. The rod was rotated into the sucrose solution to determine the temperature gradient. The spreading plates were turned on to establish convection when the temperature at 2.5-cm depth in the fluid reached 10°C. The mylar sheets were viscously coupled to the working fluid, initiating plate driven flow as the sheets were dragged across the surface. A DC motor controlled the speed of the take up reels and therefore the spreading rate velocity.

Fifteen thermocouples were placed along the ridge axis and transform fault at approximately 1-cm fluid depth to record the temperatures of the ambient fluid and temperature anomalies from the plume (Figure 5). Of the fifteen, nine were positioned along the ridge where the plume was located, one was placed along the transform fault, and the remaining five extended along the far ridge. Computer automated sampling of the temperatures at the thermocouples was logged every 30

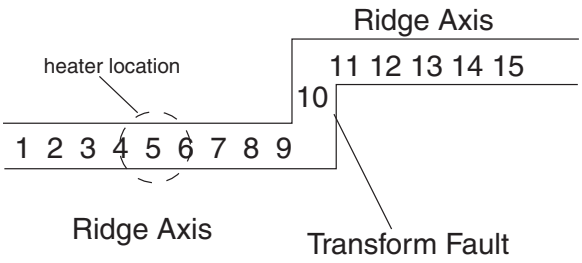

Figure 5: Configuration of thermocouples along the ridges and Transform.

seconds from the time of addition of dry ice until the end of the experiment. When the temperatures along the ridge axis reached steady state a 7.5-cm variable temperature disc heater at the bottom of the tank directly beneath the ridge axis was turned on. The disk heater warmed the surrounding fluid, forming a thermally buoyant plume (Figure 6). The apparatus was allowed to run until plume dispersion along axis reached steady state.

Dimensionless numbers are used to scale the tank experiments to the mantle. The Peclet number (Pe) is the ratio of advection to thermal diffusion and is given by the equation:

$$Pe = \frac{U_p D}{\kappa} = \frac{advection}{diffusion}$$

where U_p is plate velocity D is depth of fluid and κ is thermal diffusivity. This number represents how much heat will diffuse as a particle advects. The Rayleigh number(Ra), the ratio of buoyant forces to diffusive viscosity, is given by:

$$Ra = \frac{g\rho\alpha\Delta T}{\kappa\mu} D^3 = \frac{buoyancy}{resistance}$$

where g is gravitational acceleration ρ is fluid density, α is the coefficient of thermal expansion, T is temperature,

3. Data

12 experiments were conducted with surface cooling, plate velocity and plume strength as control parameters (Table 4). Experiments 1 through 5 were conducted without cooling, 6 through 12 had cooling plates added. Plume strengths were varied between weak, intermediate, and strong based upon plume source voltage corresponding to temperatures of less than 95°C(less than 60 Volts), 105°C(65 Volts), and 125°C(75 Volts), respectively. Plate velocities were slow, medium and fast corresponding to .25, 1.3, and 2.4-cm/min half rate mylar speed (Table 2 lists scaling parameters).

The first five experiments were conducted to determine the along axis dispersion(waist width) of the temperature anomaly produced from differing plate velocities and plume fluxes without a rheological

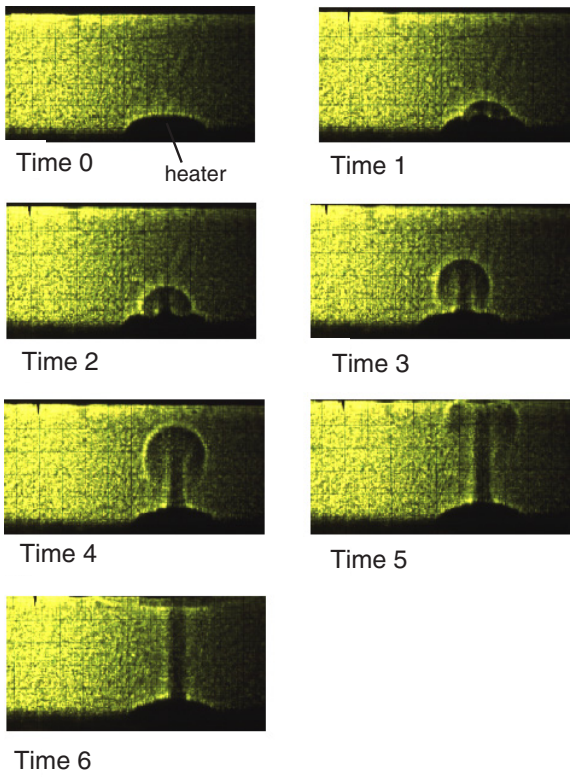

Figure 6: Formation and ascent of a plume in the tank.
D is fluid thickness, κ is thermal diffusivity and μ is dynamic viscosity. The Rayleigh number determines if a fluid is able to convect. Mantle values of the Rayleigh and Peclet numbers are used to calculate the fluid thickness(D), plate velocity (U_p) and temperature change across the fluid layer(ΔT) used to scale the experimental apparatus to the mantle. The values of the scaling parameters for the Peclet number are given in Table 2, and for the Rayleigh number are given in Table 3.

Parameter	Lab Value	Mantle Value
Transform length(m)	0.05	6 x 104
Thermal diffusivity-κ (m2/s)	10-3	10-2
Spreading Rate- Up	.25 cm/min	1 cm/year
Half rates	1.3cm/min	6 cm/year
	2.4cm/min	11 cm/year
Depth-D(m)	0.17	2 x 105

Table 2: Parameters used to scale the Peclet number.

Parameter	Value
Thermal Expansivity(α) (°C-1)	4.6 x 10-4
Density (ρ) @22°C, (kg/m3)	1422
Thermal Diffusivity (κ)(m2/s)	1 x 10-7

Table 3: Parameters used to scale the Rayleigh numbers.

Table 4: Table of experimental parameters.

Experiment	Cooling	Amount of Dry ice (block)	Mylar speed (cm/min)	Scaled speed (half rate) (cm/year)	Plume voltage(V)	Transform jump
1	No	--	1.3	6	65	No
2	No	--	1.3	6	75	No
3	No	--	2.4	11	65	No
4	No	--	.25	1.1	65	Yes
5	No	--	.25	1.1	75	Yes
6	Yes	.25	.25	1.1	65	No
7	Yes	.5	.25	1.1	65	No
8	Yes	1	.25	1.1	50/65*	No
9	Yes	1	1.3	6	65	No
10	Yes	1	1.3	6	50	No
11	Yes	1	1.3	6	50	No
12	Yes	1	1.3	6	55	No

*experiment was run at 50 Volts until steady state/constant waist width was reached then plume turned up to 65 Volts

boundary to serve as a comparison for later experiments with the addition of a sloping RBL.

Experiments 6 through 12 were conducted with cooling. Experiments 6, 7 and 8 were conducted to determine the amount of dry ice needed to produce an adequate RBL. Experiment 6 maintained 1/4 block ofdry ice, 7 a half block of dry ice and 8 through 12 were maintained at 1 entire block of dry ice. Experiments 11 and 12 were conducted with the thermocouples placed 2 centimeters and 3 centimeters deep, respectively, to determine if deeper flow occurred. The remainder of the cooling experiments change plume fluxes and plate rates to observe their effect on waist width relative to the non-cooling experiments.

4. Results

4.1. Non-Cooling experiments

The first 5 experiments determined waist widths in the absence of an RBL. Plume strength and plate velocities were the control variables. By varying the plate velocity at constant plume strength it can be seen that along axis dispersion is inversely related to plate velocity. Temperature anomaly readings along the ridges and transform were used to determine the waist width (Figure 7). Varying the plume strength at a constant plate velocity shows a hotter peak in temperature, but the waist widths are unaltered (Figure 8). These experimental results were used as a standard against which to compare the results of experiments with cooling.

4.2. Cooling experiments

Experiments 6 through 12 were conducted with the addition of a sloping rheological boundary layer. The first three of these experiments (6,7,8) were conducted to determine the amount of dry ice needed to produce a Figure 9: Effect of RBL. With a 1/4(exp. 6) and 1/2(exp. 7) blocks of dry ice per cooling plate the plume dispersion along axis is not affected much, but when cooled with an entire block of dry ice per cooling plate there was a significant change in the anomaly curve (Figure 9). With this amount of cooling the effect of a rheological boundary layer was apparent. With less

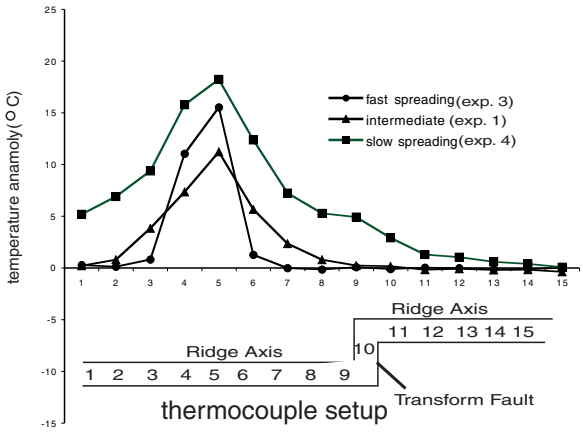

Figure 7: Non-cooling experiments with intermediate plume strength at various plate velocities.

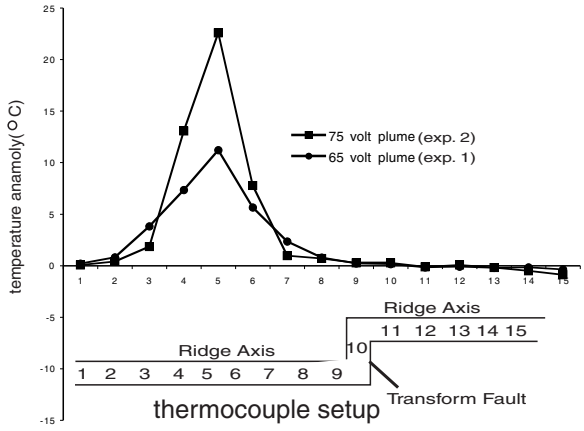

Figure 8: Non-cooling experiments conducted with intermediate plate velocity vith various plume strengths.

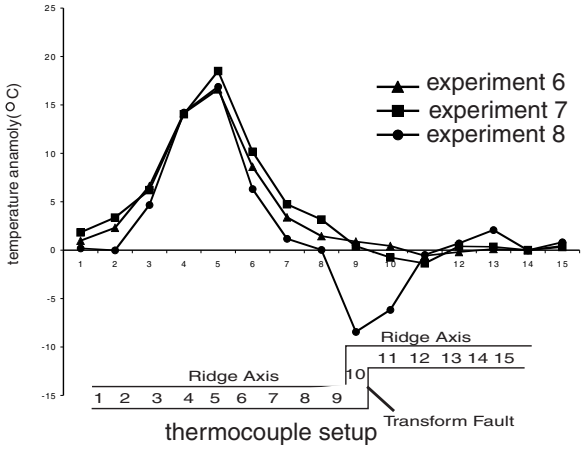

Figure 9: Effect of the amount of dry ice.

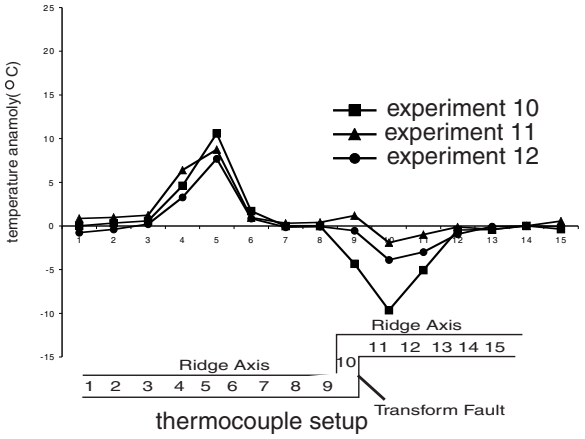

Figure 10: Depth of thermocouples record of flow.

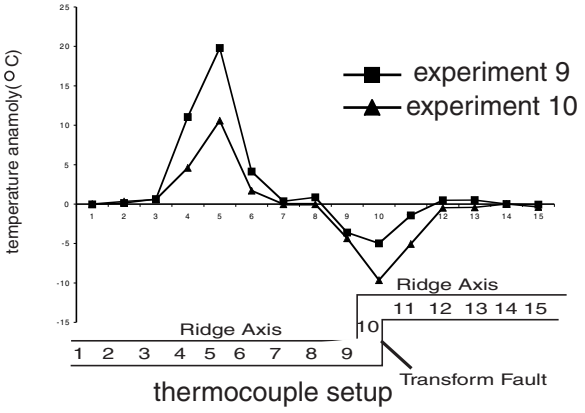

Figure 11: Same spreading velocity, different plume strengths.

cooling, the RBL is obliterated by the plume material. Experiments 10, 11 and 12 were conducted with the thermocouples placed at different depths (Figure 10). The experiments varied plume strength by 5 Volts, a temperature difference of about 10°C at the plume source. The difference in plume peak temperature may be accounted for between experiment 12 and experiments 10 and 11 by the 5-Volt difference in plume strength. Placing the thermocouples deeper in the working fluid provides information about the deeper flow. There is a skewed temperature anomaly in experiment 11. The cooling at the transform is less apparent at depth, but it is unusual that there is more of an effect at 3-cm depth than 2-cm. The basic curve shapes are the same at all the depths.

Experiments 9 and 10 were conducted with the same rate of spreading but different plume strengths (Figure 11). The height of the temperature anomaly is greater for the stronger plume, but the width of the anomaly is the same for both plumes. Experiments 8 and 10 had the same plume strength but different spreading velocities (Figure 12). The waist widths are very similar despite the difference in spreading rates. There is a skewedness to the cooling effect at the transform at the lower plate velocity.

The addition of cooling has two unexpected results (Figure 13). With an intermediate plate speed it can be seen that the waist width is smaller with cooling (experiment 9) than without (experiment 1). We had predicted greater along axis flow, so this is the exact opposite of our predicted result (Figure 13a). There is also a significant cooling effect at the transform not seen in the uncooled experiment. At a slower spreading rate, without cooling (experiment 4), the plume material spreads across the transform, but with the addition of the RBL the plume material does not even disperse to the transform, spreading only to thermocouple 8(Figure 13b). This also has the effect of greatest cooling at thermocouple 9, located just before the transform rather than thermocouple 10, in the transform, where the coldest temperatures would be expected.

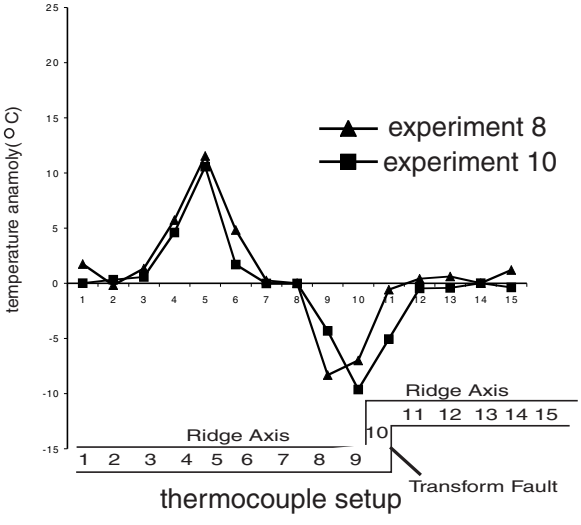

Figure 12: Same plume strength, different plate velocities.

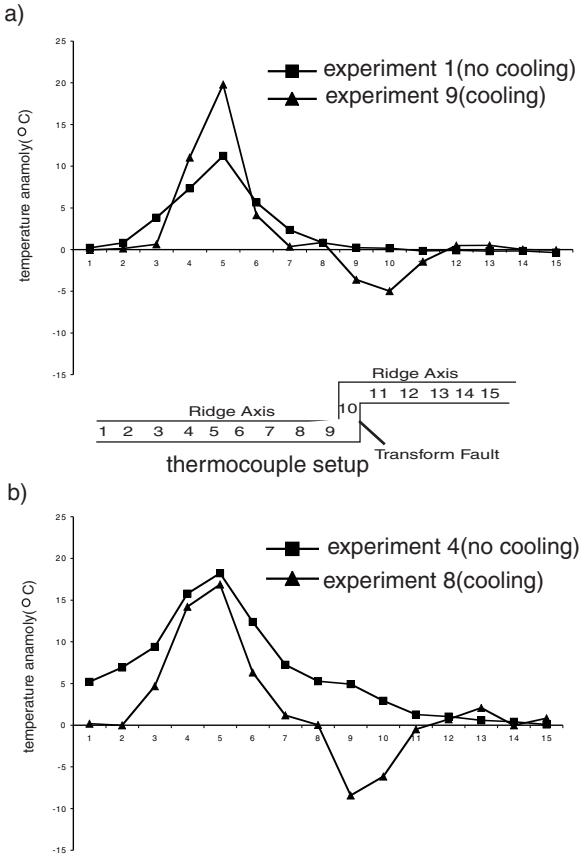

Figure 13: Comparison of cooling versus non-cooling. a) intermediate plate velocity, intermediate plume strength b) slow plate velocity, intermediate plume strength.

5. Conclusions

5.1. Non Cooling

The experiments conducted without cooling found waist width to be a function of plate velocity. As plate velocity increases, the waist width decreases (Figure 7). At higher plate velocities more material is transported away from the ridge axis by the plates. At the slower plate velocities, there is more heated plume material coming to the surface then can be moved with the plates, so the plume must disperse along axis to compensate for the excess flux. Plume strength does not have any significant effect on the waist width though it does affect the magnitude of the thermal anomaly (Figure 8). These results support the conclusions of Feighner and Richards [1995], who used a chemically buoyant plume beneath an unsegmented ridge axis. They found waist width to be an inverse function of plate speed, with plume strength having only a small effect.

5.2. Cooling

Changing the depth of the thermocouples did not reveal any significant variation in the width of the temperature anomaly along axis produced by the plume. It did, however, show that there was less of a cooling effect at greater depths along the transform. For some reason there is more of an effect at 2-cm then 3-cm depth, but both are less than that of 1-cm depth. Except for the transform effect these results show all the near surface flow (at least the top 3-cm, scaled to the top 100km of the Earth) to be similar. With the addition of cooling there is no significant variation in waist width as a function of plume strength. For a given spreading rate the temperature anomaly produced is the same regardless of plume strengths.

5.3. Plume dispersion

Spreading rate does not appear to effect waist width either. This may be due to cooling at the transform creating a dam, preventing along axis flow. The cooler material at the transform is much more viscous than the plume material, which may force the plume to disperse under the plates rather then along axis toward the transform. The unexpected plume dispersion patterns may be due to thermal erosion of the RBL by the plume head. The plume may be so much hotter than the RBL that it erodes the RBL away, leaving an area that can not re-establish a boundary. This may create a pocket in the base of the RBL that may enhance transport of plume material perpendicular to the ridge axis.

5.4. Cooling at the transform

The other unexpected finding was the cooling effect at the transform offset. This is noticeable in both comparisons (Figure 13). With cooling the temperatures are significantly colder both near and in the transform fault (Figure 13a). The transform effect may be due to a lack of upwelling at the transform. Upwelling occurs at both ridge axes due to convection. The transform is stationary, so it may be possible that there is no upwelling at that location. This cooling at the transform may also play a part in the observed decrease in waist width with the addition of the RBL. The much cooler and therefore more viscous fluid at the transform may force plume material to disperse under the plates rather than along axis. The recent tomographic studies of Van Avendonk et al. [2001] find low seismic velocity anomalies across the Clipperton transform fault which they attribute to lower mantle temperatures along the transform. The tank model displays a similarly cooler area at the transform.

Acknowledgments. I would like to thank Roger Larson and Chris Kincaid for giving me the opportunity to do research for the summer, and for all the help they have given me. I also thank Rich Viso for always being willing to help me whenever it was wanted or needed and for dealing with me. Thanks to Rob Pockalny and Paul Hall for always being available for help and to Rob Pockalny, Chris Kincaid, Paul Hall, Kim Carey and Rhoda Kenny for running the SURFO program.

References

Douglass, J., Schilling, J.-G., and Fontignie, D., Plume-ridge interactions of the Discovery and Shona mantle plumes with the southern Mid-Atlantic Ridge (40°-55°S), *Journal of Geophysical Research,* 104, 2941-2962, 1999.

Feighner, M.A., and Richards, M.A., The fluid dynamics of plume-ridge and plume-plate interactions: An experimental investigation, *Earth and Planetary Science Letters*, 129, 171-182, 1995.

Kincaid, C., Ito, G., and Gable, C., Laboratory investigation of the interaction of off-axis mantle plumes and spreading centres, *Nature*, 376, 758-761, 1995.

Kincaid, C., Schilling, J.-G., and Gable, C., The dynamics of off-axis plume-ridge interaction in the uppermost mantle, *Earth and Planetary Science Letters,* 137, 29-43, 1996a.

Kincaid, C., Sparks, D.W., and Detrick, R., The relative importance of plate-driven and buoyancy-driven flow at mid-ocean ridges, *Journal of Geophysical Research,*101, 16,177-16,193, 1996b.

Rear, L., Laboratory study on the dispersal of on-axis mantle plumes at transform faults, *SURFO paper*, 1999.

Ribe, N.M, Christensen, U.R, and Theiβing, J., the dynamics of plume-ridge interaction, 1: Ridge-centered plumes, *Earth and Planetary Science Letters,* 134, 155-168, 1995.

Schilling, J.-G., Upper mantle heterogeneities and dynamics, *Nature*, 314, 63-67, 1985.

Van Avendonk, H.J.A., Harding, A.J., Orcutt, J.A, and McClain, J.S., Contrast in crustal structure across the Clipperton transform fault from travel time tomography, *Journal of Geophysical Research,* 106, 10,961-10,981, 2001

Analysis of Curve-Fitting Techniques for Methanotrophic Rate Calculations in Ocean Sediments

Nicole Persky[1]

Graduate School of Oceanography, University of Rhode Island, Narragansett, Rhode Island

Abstract. Methane is microbially consumed in ocean sediments through sulfate reducing methanotrophy. It has been suggested that this reaction is the globally dominant means of both methane and sulfate destruction. Consequently, such microbial reaction rates can have a great effect on ocean alkalinity, pH, and atmospheric composition. Eventually, rates for subsurface sulfate reduction will be calculated the future. These rates will be used as a basis to quantify and better understand the controls on total respiration and anaerobic methanotrophy. Rates will be determined through the use of sulfate profiles from representative OSDP/ODP sites and pore water diffusion models. This project was an analysis of curve fitting techniques of sulfate data for the determination of these rates. Of the techniques tested, we determined that smoothed finite difference was the best, and that polynomial fitting was insufficient for our purposes.

1. Introduction

The anaerobic oxidation of methane is a geochemically well documented process, however little is known about the metabolic activity and identity of the microbes involved. Orphan et. al. (2001) recently were able to identify methanotrophic species using fluorescent in situ hybridization and secondary ion mass spectrometry[1]. Their technique opens up many possibilities for future studies of microbial identification and activity. Even though this and other direct methods for measurement of metabolic rates of methanotrophic micro-organisms exist, they have not been routinely carried out at many DSDP/ODP sites, and still not much is known globally about the role of the total respiration of these microbes in deep ocean sediments. Rates of such methanotrophic metabolic activity can have critical impact on global geochemical cycles[*Fenchel and Blackburn*, 1998]. A large reason for this is that methanotrophic microbial respiration is thought to be the major sink for both sulfate and methane in the world oceans. Methane cycles are important because it is a great heat retaining gas, and could possibly pose a problem in the ongoing warming of the earth. Sulfate plays a very important role in ocean salinity since it carries with it a charge of minus two. A charge balance of the most prominently concentrated charged species in the average sample of ocean water reads as follows:

(1) $[H^+] + [Na^+] + 2[Ca^{+2}] + 2[Mg^{+2}] + [K^+] = [Cl^-] + 2[SO4^{-2}] + [HCO3^-]$

[1] Oberlin College Graduate

The charge balance must always be conserved in a steady state system. Most of the cations are biologically unreactive. There are only three major constituents that make up the anion side of the equation, and chloride is thought to remain conservative (unreactive) through the sediment column. Bicarbonate is approximately 2.5mM on average, and sulfate is approximately 28 mM on average in sea water [*Pilson*, 1998]. Since sulfate carries twice as much weight in the equation, and its concentration is so high, a relatively small change in sulfate concentration has a big effect on bicarbonate. Bicarbonate, in turn is the only anion that can accept an H^+ and is also in equilibrium with CO_2 concentrations in the sea. Dissolved CO_2, in turn, exists in equilibrium with CO_2 gas in the atmosphere. Thus, small changes in concentration of sulfate directly effect ocean alkalinity, pH, and CO_2 exchange with the atmosphere. If the major sink for sulfate and methane, thought to be methanotrophic respiration, were to change, this in turn would have a large scale effect on both the ocean and the atmosphere.

The redox reaction called methanotrophy can be written as follows:

(2) $CH_4 + SO_4^{-2} \rightarrow 2H_2O + CO_2 + S^{-2}$

Methane is produced by fermentation from methanogens at deeper levels of the sediment column and diffuses upwards. Sulfate diffuses downwards from the sediment water interface. Both concentrations approach zero, and overlap in the methanotrophic zone. An example of this is illustrated in Figure 1. Where the decrease in concentration of both reactants is linear change in slope of sulfate data only occurs in one place,

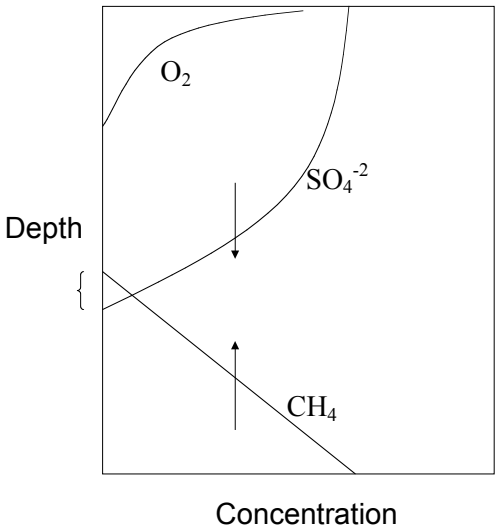

Figure 1. Hypothetical subsurface concentration profiles for oxygen, sulfate and methane.

and the methanotrophic zone is a simple plane (See figure 2a). A more complicated situation occurs when decreases in concentration are not linear, as shown in Figure 2b.

Though direct measurements of metabolic rates of reaction can be measured, they have not been carried out routinely. Indirect estimations of sulfate reduction rates can be derived from changes in sulfate concentration that is available for many DSDP/ODP sites. The relation between sulfate concentration and reaction rate can be described through Ficks laws of diffusion.

Fick first postulated the diffusional flux equation with an analogy to the equation for the conductance of heat and the conductance of electric current as developed earlier by Fourier and Ohm respectively [*Lerman,* 1988]. Ficks first law of diffusion states that:

$$J=-D(dC/dz) \quad (3)$$

Where J= flux, D= Diffusion constant, and C= concentration of the chemical in question and z=depth. Fick stipulated that the flux relies on the gradient, the cross-sectional area and a coefficient D that depends on the nature of the diffusional material and the medium [*Lerman,* 1988]. When dealing with flux due to molecular diffusion through sediment porewater, the porosity and the tortuosity of the sediment have a great effect on the outcome. In such a scenario, equation (1) can be re-written as [*Lerman,* 1988]:

$$J=-\phi(Dsol/\theta^2)(dC/dz) \quad (4)$$

Where ϕ= porosity, and θ^2= Fϕ= tortuosity.

Any change in the flux within the layer between z and z+dz must be accounted for by a change in concentration within the layer,as postulated by Fick's second law of diffusion [*Lerman,* 1988]:

$$dC/dt =-dJ/dz \quad (5)$$

However, when there is production or uptake of the chemical in question the equation is modified to:

$$dC/dt =-dJ/dz + P - U \quad (6)$$

In the case of sulfate, we assume that there is no advection due to flow, (as is the case at many ODP sites), and that the only input of sulfate should due to diffusion from ocean water. Therefore P in our case should be equal to zero. However, wherever microbes exist that uptake sulfate to be used for metabolic purposes there should be a significant uptake term in the form of a rate of reaction. Equation six can then be rewritten as:

$$dC/dt =-dJ/dz + R(z) \quad (7)$$

where R(z) equals the global rate of reaction of sulfate consuming microbes as a function of depth. At steady state, dC/dt = 0, and therefore:

$$R(z) = -dJ/dz \quad (8)$$

Thus, the total respiration of a column of sediment may be estimated from the downward flux of sulfate through the column. Plugging equation (3) into this expression reveals that the only troublesome unknown is d^2C/dz^2, since both ϕ and θ^2 are regularly recorded at ODP sites, and/or in some cases can be approximated. For simplicities sake, ϕ and θ^2 are assumed to be constant; and the final equation to be used for approximating the rates of methanotrophic reactions becomes:

$$R(z) = - k (d^2C/dz^2) \quad (9)$$

Where k equals a constant. . Visually, d^2C/dz^2 represents the curvature of a C vs. z curve. In the simple case illustrated in Figure 1., the reaction rate can be approximated at a single depth by taking the difference between the slope of the line representing decreasing sulfate concentration, and zero (which is the slope of the line at depths below the methanotrophic zone). In the more complicated case of Figure 2., a method for approximating curvature from experimental sulfate concentration vs. depth data will be needed. The main goal of this project is to explore possible smoothing methods for the best approximation of curvature, that will ultimately help determine rates of methanotrophy in ocean sediments across the globe.

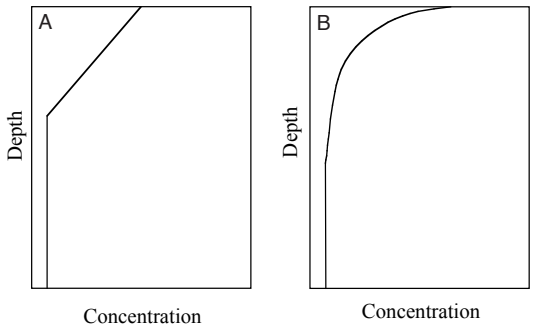

Figure 2. Illustration of linear (a) and nonlinear (b) decreases in sulfate concentration with depth.

2. Methods

2.1. Defining 'Best Fit'

Since experimental data almost certainly contains some sort of measurement error that appears as random noise in the final output, a method of observing general trends through the noise is needed [Sasena, 1998]. Since each point is not exact, a better fit does not mean proximity of predicted points to actual data points, as is assumed for curve fitting with splines and high order polynomials. These techniques seek to locally smooth the data, and force curves through every measured point. As a result, the fitted curves are incredibly bumpy and tell little of general trends in curvature that are sometimes obvious even to the naked eye. A globally smooth function will capture the general trend of the response much better than a choppy one [Sasena, 1998]. We have resolved to use low order polynomials, finite difference, and running averages to estimate the curve that fits our data best.

To compare these three techniques we started with a representative simulated function, with known second derivatives, and added stochastic disturbance. To the noisy function we applied the various techniques and compared the proximity of predicted second derivatives to the second derivatives of the simulated function. Second derivatives were used as a measure of fit because calculations of reaction rates ultimately require this value, and not the actual concentrations. 199 points were calculated for each curve. All calculations and figures were done in excel.

2.2. Defining the Representative Function

For the simulated concentration vs. depth curve we assumed an exponential decay of the form:

$$C = C° - \Delta C\,(1 - e^{-z / \mathbf{z_{1/2}}}) \quad (10)$$

Where the curvature of this function may be expressed by its second derivative:

$$d^2C/dz^2 = (\Delta C/(\mathbf{z_{1/2}}^2))\, e^{-z / \mathbf{z_{1/2}}} \quad (11)$$

In this scenario, different values may be plugged in for four adjustable parameters: C°= initial concentration at 0 meters below sea floor, ΔC = the change in concentration between the initial and the converged asymptotic values, $\mathbf{z_{1/2}}$ = the depth at which the concentration reachs one half of the initial concentration, and Δz = depth between each data point taken. The exponential function was chosen because an 1st order rate reaction would have such a shape, and it also has simple second derivatives that vary with depth.

2.3. Adding Noise

To the simulated function was added stochastic disturbance. It was assumed that each concentration value was uncertain to ±2mmol of sulfate, through assessing the error reports from sulfate concentration measurements from previous ODP sites. To add this noise to the function, a column of random numbers between 0 and 4 were generated through a random number generator under the function menu in excel. These random numbers were copied and pasted as values in a separate column (so they would not change every time the workbook was changed). The simulated function was then changed to the form:

$$C_f = (C°\text{-}2 + \text{rand.}) - \Delta C\,(1 - e^{-z / \mathbf{z_{1/2}}}) \quad (12)$$

2.4. Smoothing the Simulated Function

Finite Difference

Curvature for the noisy function was approximated using the finite difference approximation of:

$$d^2C/dz^2 = (\,C_{(z+1)} - 2C_{(z)} + C_{(z-1)}\,)/\,\Delta z^2 \quad (13)$$

Smoothed Finite Difference

Curvature for the noisy function was approximated using the smoothed finite difference approach by first averaging every three points to give 1/3 the number of points, and then applying equation (13) to the reduced data.

Polynomials

Curvature for the noisy function was approximated by fitting polynomials through use of the least squares method. The least squares method was applied to the data through the regression program found in the data analysis add in of the excel tool menu. Columns were created for z, z^2, z^3, z^4, and z^5. Only fourth and fifth order polynomials were fit to the noisy data as these resulted in quadratic and cubic second derivatives. Any lower order polynomial fit was not thought sufficient to follow the exponential decay of the actual functions second derivative. For fourth order polynomials, the z, z^2, z^3, and z^4 columns were used for the x-input area. For fifth order polynomials, the z^5 column was included in the x-input area. The y-input area consisted of C's calculated using equation 12. The second derivatives for each least squares function were calculated by hand.

2.5. Curve-Fitting Comparisons

The second derivatives calculated for each of the three techniques were compared with the simulated function's actual second derivative (equation 11). For each point the absolute difference between the predicted vs. actual curvature was taken. Averages and standard deviations of these differences were subsequently calculated. For each technique, ten different simulations were tested, and the difference averages and standard deviations were again averaged. Absolute differences were also translated into percent errors for each point. Stacked curves were plotted for predicted curvature and actual curvature vs. depth for visual reference and plausibility of fit.

2.6. Sensitivity Tests

The adjustable parameters were varied to assess the robustness of smoothing techniques to different changes in curvature. These sensitivity tests were used as a way to check results of the curve fitting comparisons. Each technique was tested using the input variables listed in Table 1.

3. Results and Discussion

3.1. Curve Fitting Comparisons

Before sensitivity tests were undertaken, a standard input of the adjustable parameters was used to generally compare the methods. The input used was the following: Δz =5m, ΔC =15 m, and $\mathbf{z_{1/2}}$ = 10. The finite

Table 1. Sensitivity test values for keyparameters.

C°	Δz	ΔC	$\mathbf{z_{1/2}}$
30 mmol	5 m	0 m	10 m
	10 m	2 m	15 m
		15 m	50 m
		30 m	100 m

difference approximation, without smoothing, remained incredibly noisy, and no general trends could be seen at all. This is shown visually in Figure 3 and numerically with high difference averages and standard deviations of 0.092 mM/m^2 and 0.007 mM/m^2 repectively.

The smoothed finite difference approximation cut out a lot of the noise and fit much closer to the actual function with a 0.0117 mM/m^2 average and a 0.0008 mM/m^2 standard deviation (see Figure 4). However, due to the nature of running averages, the output curve had much fewer data points. Since the curvature of this standard input function really only occured in the first eight data points, the loss of units effected the ability to define the curve, even though the points lay much closer to the actual function's second derivatives.

Upon fitting a fifth order polynomial to the curve, we find that the difference averages and standard deviations drop immensely (see Table 2). However, the visual graph of the data does not fit the curve at all, and appears to be basically a flat line at y=0 for the entire curve (see Figure 5). This output occurred because there were 199 points in the input, most of which fall after the exponential has converged to zero. Subsequently, the least squares technique put a lot of weight on the fact that a straight line fit most of the data very well. With this in mind, the data was refit for only what appeared visually to be the curved part of the function (the first eight points). It was assumed this was a plausible area to define for any reasonable data set. For this second fit, the difference averages and standard deviations remained low. But again, the curvature did not correlate with that of the original function. The second derivatives cubic did not utilize its positive concavity, but crossed back and forth through the data (see Figure 6). Consequently the curve was refit using 31, 18, and 21 points, till the curvature of the cubic looked similar to that of the original function(see Figures 7-9).

The fourth order polynomial (quadratic second derivative) was fit to the first eight points under the assumption that if there was not a change in concavity of the second derivatives the number of fit points might not be as much of an issue for the flexibility of the polynomial. Unfortunately, the fourth order fit only accentuated the inflexibility of polynomials, and the resulting quadratic, again, did a poor job of illustrating general trends in the second derivatives of the initial function (see Figure 10).

In summary: two bases of comparison were used. The first consisted of averages and standard deviations of the absolute difference between the predicted and the actual second derivatives. The second was the plausibility of the second derivative curvature (primarily concavity). The smoothed finite difference technique as well as all fitted polynomials had similar absolute difference values. However, fitting polynomials by using merely difference values to determine fit prove insufficient for estimating trends. Polynomial fitting requires a predetermined knowledge of curvature (i.e. how much of the curve to fit) for plausible concavity. Subsequently this technique is not compatible with the need to find general trends in curvature without a

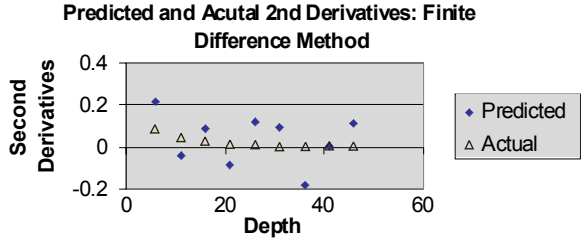

Figure 3. Predicted and actual second derivatives for the finite difference method without smoothing. The predicted values are noisy.

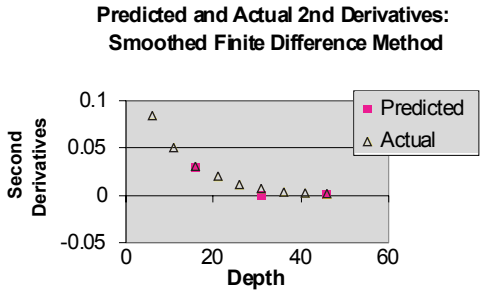

Figure 4. Predicted and actual second derivatives for the finite difference method after smoothing the data with a running average.

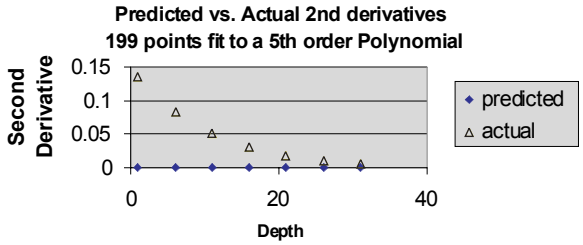

Figure 5. Predicted and actual second derivatives for a fifth-order polynomial fit to all data. The poor fit it due to the large number of data points that are in the zone where the exponential has already fallen to zero.

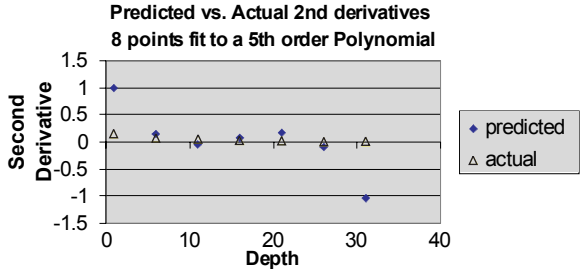

Figure 6. Predicted and actual second derivatives for a fifth-order polynomial fit to only the upper 8 data points that define the profile.

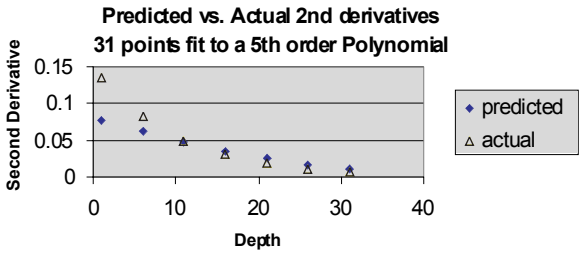

Figure 7. Predicted and actual second derivatives for a fifth-order polynomial fit to 31 data points.

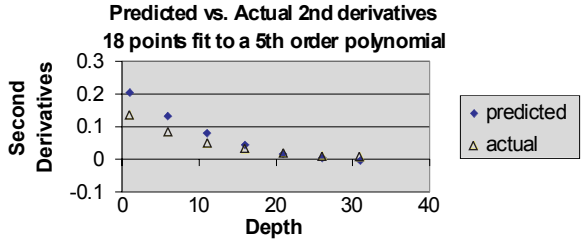

Figure 8. Predicted and actual second derivatives for a fifth-order polynomial fit to 18 data points.

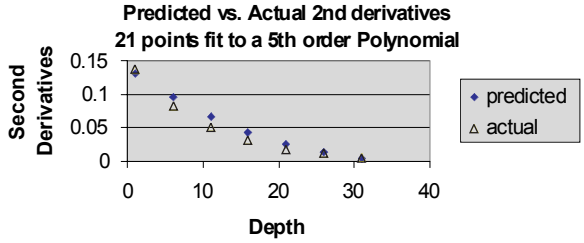

Figure 9. Predicted and actual second derivatives for a fifth-order polynomial fit to 21 data points. This solution provides the best estimates of the actual second derivative for the fifth-order polynomial case.

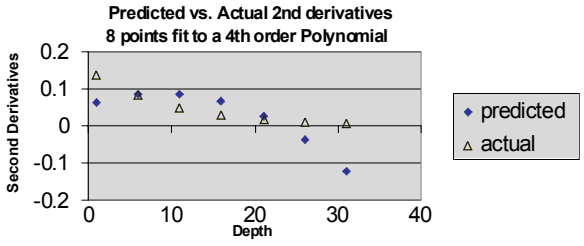

Figure 10. Predicted and actual second derivatives for a fourth-order polynomial fit to 8 data points.

predetermined function.

We determined that of the three techniques smoothed finite difference followed the curve best and remained flexible. It also has the added advantage of control over smoothness. However, smoothed finite difference approximations have the disadvantage of decreasing the amount of data points. To be used to its full capacity, the tester must balance the accuracy of fit with ability to determine general shape. In other words, with smoothed difference approximations, the tester will be faced with the problem of deciding the equivalent of a smoothness factor.

3.2. Sensitivity Tests

Changes in the adjustable parameters did not significantly change the average difference values or the plausibility of curvature results that were determined from the curve fitting comparisons.

4. Conclusions and Future Work

Of the techniques addressed in this project, it was determined that the smoothed finite difference approximation is the most helpful for determining general trends in curvature of sulfate concentration vs. depth data. However, a major setback in using this technique is that there are few ODP sites where the tester can afford to reduce the number of data points and still determine curvature. If a different technique is needed, it is suggested that higher mathematical methods are employed. Two examples of more complex techniques are the smoothed spline method and Kringing method; both allow the tester to keep the original number of points. If used, the tester can define a curve that goes through all the data points, and then determines an appropriate smoothness factor. Whichever smoothing method is used, however, the tester will remain faced with the problem of determining the appropriate amount of smoothness. This in itself will pose quite a challenge. Even with an appropriate smoothness factor, it remains unclear that this progression from local to global smoothing is the best way to determine general trends in curvature. In the future, it would be useful to run curve fitting comparisons and sensitivity tests on these more complex models.

Acknowledgments. Thanks to Art Spivack, Steve D'Hondt, Scott Rutherford and all of the other SURFO's for their help on this project.

References

Fenchel, T., King, G. M., Blackburn, T. H. *Bacterial Biogeochemistry*, pp. 230, Acedemic Press, San Diego, 1998.

Lerman, A., *Geochemical Processes*, pp.74, Krieger Publishing, New York, 1988.

Orphin et al., *Science,*20 July 2001 vol. 293, pp. 484.

Pilson M. E. Q. , *An Introduction to the Chemistry of the Sea*, pp.59, Prentice Hall, New Jersey, 1998.

Sasena Mike, Masters Thesis, [pdf]www-personal.engin.umich.edu/~msasena/Thesis.pdf

Horrible, horrible things: Numerical modeling of oil spills in Narragansett Bay

Dan Shaevitz[1]

Graduate School of Oceanography, University of Rhode Island, Narragansett, Rhode Island

Abstract. Numerical modeling is an important tool in the study of geophysical fluids. This methodology is particularly powerful because the response of natural systems to a range of parameters can be examined, which is not possible in "real world" experiments. Modeling estuarine circulation allows the prediction of the transport of materials that are in the water column such as pollutants, larvae, or other biological organisms. We use a three dimensional model of Narragansett Bay to perform numerical experiments on the dynamics of oil spills. We study the significance of different surface wind directions and magnitudes, as well as the significance of including variable salinity in the model. Most models only look at oil at the surface, but oil that mixes down into the water might behave differently than surface oil. We examine the difference in the spread of oil at the surface and oil that mixes down into the water. Our results suggest the direction and magnitude of surface winds provide a large constraint on the path of the oil spill and including variable salinity drastically changes the extent of oil dispersion within both surface and bottom waters.

1. Introduction

The physical dynamics of an estuary determine the transport of nearly all materials in the estuary. These materials include pollutants, biological organisms, and nutrients. Therefore, the ability to predict the velocity field of an estuary is an important tool in understanding the biology and chemistry of the estuary. There have been various numerical studies of estuarine circulation (e.g., Gordon and Spaulding, 1987). They are useful tools for studying the transport of these kinds of tracers because they predict the velocity field.

In this study we examine the dynamics of oil spills in Narragansett Bay. Narragansett Bay is a weakly stratified estuary in Rhode Island. The three important forces that act on this estuary are tidal forces, surface wind stress, and density effects caused by the salinity gradient. We examine the effect of these forces on the spread of oil in the Bay.

Oil spill modeling aids in the timely containment of spills and minimizing their damage. Most oil spill models only look at the spread of oil at the surface and assume that this will give an accurate representation of the total oil spreading. This may not be the case if the oil mixes down into the water column. We study the transport of oil at the surface as well as oil that mixes downward into the water column.

[1]Now at Columbia University

2. Model Description

The model we use is the Regional Ocean Modeling System (Haidvogel et al., 2000). It is a three-dimensional, free-surface, hydrostatic, primitive equation ocean model that uses stretched, terrain-following coordinates in the vertical and orthogonal cartesian coordinates in the horizontal. The primitive equations are:

$$\partial u / \partial t + \vec{u} \cdot \nabla u - fv = - \partial \phi / \partial x + F_u + D_u \quad (1)$$

$$\partial v / \partial t + \vec{u} \cdot \nabla v + fu = - \partial \phi / \partial y + F_v + D_v \quad (2)$$

$$\partial T / \partial t + \vec{u} \cdot \nabla T = F_T + D_T \quad (3)$$

$$\partial S / \partial t + \vec{u} \cdot \nabla S = F_S + D_S \quad (4)$$

$$\rho = \rho(T,S,P) \quad (5)$$

$$\partial \phi / \partial z = -\rho g / \rho_0 \quad (6)$$

$$\nabla \cdot \vec{u} = 0 \quad (7)$$

Equations (1) and (2) are the conservation equations of momentum for the x and y directions. Equations (3) and (4) are the advection-diffusion equations for potential temperature and salinity. Equation (5) is the equation of state. Equation (6) is the hydrostatic balance with the Boussinesq approximation. Equation (7) is the incompressible continuity equation.

We run this model on a domain from the Providence River as the north boundary and Rhode Island Sound as the south boundary. We force the open boundaries with tidal heights and amplitudes we obtained from the Adcirc circulation model run by the USGS and force the surface with analytical wind stresses.

We use 90 grid boxes in the zonal direction, 150 grid boxes in the meridional direction, and 20 grid boxes in the vertical direction. The vertical "sigma" coordinate is stretched and terrain-following. Since there are 20 vertical levels at all points in the bay, shallower points will have shorter grid boxes and deeper points will have taller grid boxes. Also, any vertical level will be at different depths at different points in the bay, depending on the total thickness of the water at that point.

3. Description of Numerical Experiments

We modeled an oil spill at Brenton Reef in Narragansett Bay (Figure 1) and represented the oil spill by adding lagrangian "floats". These floats move along lines of constant geopotential by horizontal advection. It is important to note that we are ignoring the effect of horizontal diffusion or any other sinks for the oil, such

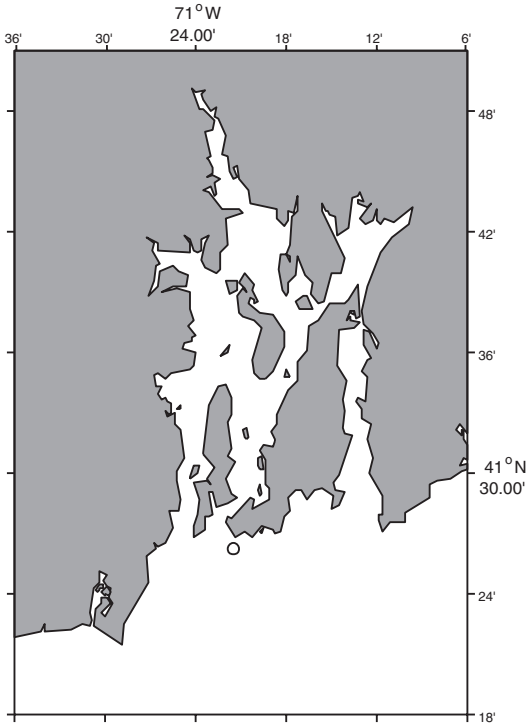

Figure 1. Brenton Reef. Site of oil spill (circle).

as loss to the bottom or air. We account for vertical diffusion by placing floats at the top, middle, and bottom sigma level. Finally, the simplifying assumption is made that much of the important dynamics are advection based and that we may still capture many of the important features of the oil spill while ignoring other terms in the transport equation.

All runs are forced with tidal components M2, M4, M6, S2, N2, K1, and O1 obtained from the Adcirc circulation model run by the USGS. We examined the effects of different wind speeds and directions and the effects of salinity. We used four different surface wind directions and three different surface wind speeds. The control run had no wind and subsequent trials had winds of 5, 7, and 9 m/s out of the north, east, south, and west. We ran the model without variable salinity for each case and then ran the 5 m/s cases with variable salinities and fresh water input at the Providence River of 50 cubic meters per second. The initial condition for the salinity runs was a simple linear meridional gradient, starting at 30 PSU at the south boundary and ending at 0 at the Providence River. (In order for the numerics to work properly, we included a very small sine wave perturbation to this salinity field in the zonal direction in the). A constant temperature was applied throughout the bay in all runs.

The duration of all experiments was five days. Initial wind speed was zero and ramped up over three hours to the final wind speed. After three days, speeds were ramped down over three hours. The final two days had no wind. Ten floats were put in at each of the top, middle, and bottom layers. The first float at each level was added 12 hours into the run in order to give the model time to "spin up". Every additional six hours, a float was added at each level.

The duration of all experiments was five days. Initial wind speed was zero and ramped up over three hours to the final wind speed. After three days, speeds were ramped down over three hours. The final two days had no wind. Ten floats were put in at each of the top, middle, and bottom layers. The first float at each level was added 12 hours into the run in order to give the model time to "spin up". Every additional six hours, a float was added at each level.

4. Results

4.1. Without variable salinity

The positions of floats over time mark dispersion patterns, or pathways, for oil introduced to the system. These particle paths also provide a glimpse into both tidal and non-tidal circulation patterns as a function of different forcing conditions. Results are presented for simple cases first and then for cases with increasing complexity.

Figure 2 shows the partical trajectories of the oil floats with no wind or salinity in the top, middle, and bottom levels. The oil does not go very far in this run. The prevailing pattern is characterized by the floats moving northward along the east side of the east passage and then moving southward along the west side of the east passage.

Figure 3 shows the partical trajectories for the runs with winds out of the north and no salinity. It shows the top, middle, and bottom levels for a 5, 7, and 9 m/s surface wind. In the 5 m/s run, only the surface floats seem to be influenced by the wind. The surface floats go to the south. For stronger wind speeds, the bottom and middle floats go further north. This is reasonable, because conservation of mass dictates that if the surface water is flowing south, there must be a return flow going north.

Figure 4 shows the same plots with winds out of the south. Like with the southerly winds, the surface water flows in the direction of the wind. Interestingly, at higher wind speeds there is basically no flow opposite the wind by the bottom floats and only a very small return flow by the middle floats.

Figure 5 shows the same plots with winds out of the east. The surface water flows with the wind. At higher wind speeds, the middle and bottom floats do not go against the wind, but in some cases go slightly more north and south.

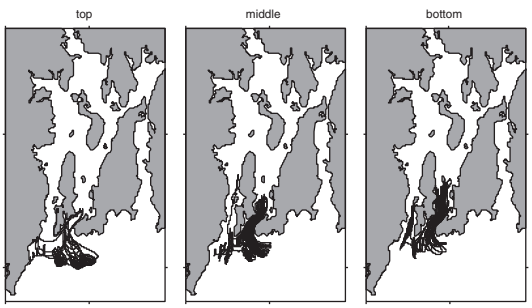

Figure 2. Path of oil spill. No wind. No salinity.

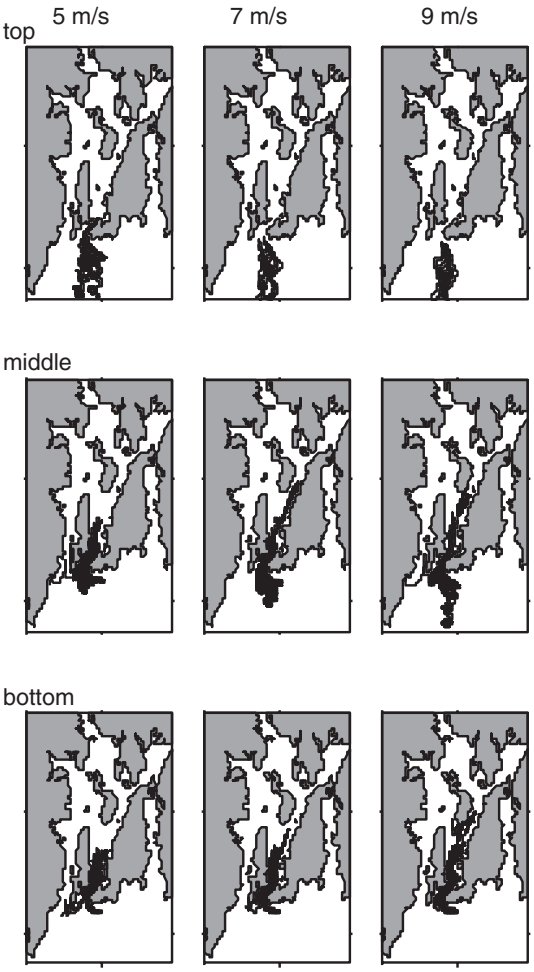

Figure 3. Path of oil spill. Northerlies. No salinity.

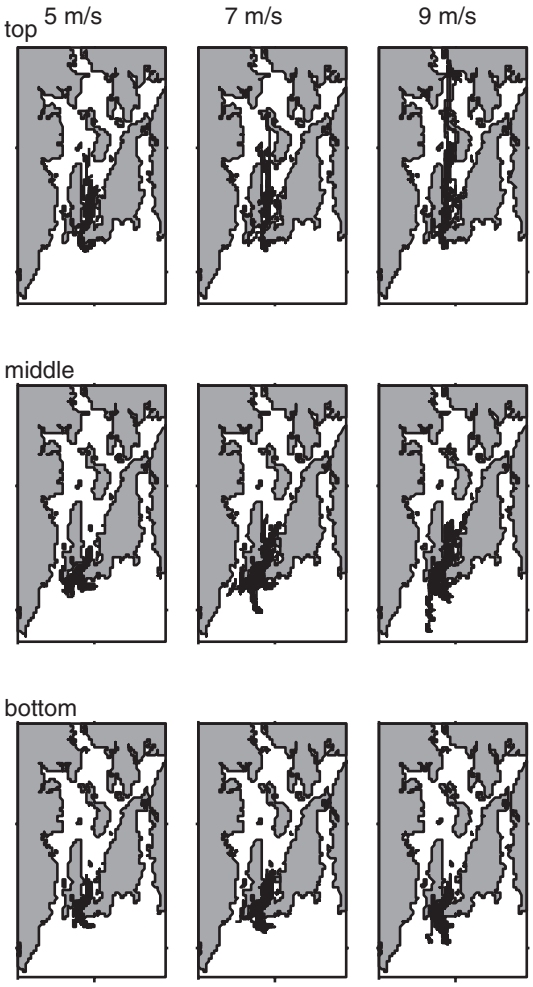

Figure 4. Path of oil spill. Southerlies. No salinity.

Figure 6 shows the same plots with winds out of the west. The surface water flows with the wind, and interesingly at higher wind speeds, the middle floats go with the wind and with a 9 m/s wind even the bottom floats go with the wind.

In the runs with no salinity, the winds did not have a very large influence on the floats in the middle and bottom layers. With the northerlies and southerlies, the bottom floats typically traveled opposite the wind direction. With the easterlies and westerlies, the middle and bottom floats sometimes moved orthogonal to the wind and sometimes traveled with the wind.

4.2. With variable salinity

Long term transport in estuaries is clearly influenced by background density gradients. In natural systems like the Bay, density is related to both temperature and salinity. In order to begin simply, we start by considering the role of salinity on non-tidal dispersion patterns.

Figure 7 shows the particle trajectories of the oil floats with no wind, including variable salinity and a freshwater source from the Providence River. Clearly, including variable salinity and adding mass at the Providence River makes a substantial difference. As expected because of the freshwater from the Providence River the surface floats travel further south than they did without salinity. Also, because of the density effects, the middle and bottom floats go much further north. The oil floats also spread more with salinity than without salinity.

Figure 8 shows the particle trajectories of the floats for 5 m/s winds out of the north and south while including variable salinity. For the northerly wind, the surface floats travel further to the south and less to the east and west than without wind. The middle and bottom floats travel further north and the bottom floats move less to the east than without any wind. With the southerly wind, some of the surface floats travel much further north and the floats do not move southeast as in the no wind case. The middle floats do not move as far north and more floats move to the south and east as in the no wind case. The bottom floats move further to the south and less to the east than with no wind.

Figure 9 shows the trajectories for 5 m/s winds out of the east and west with variable salinity. For the easterly wind, the surface floats all move southwest instead of some of the floats moving southeast as in the run with no wind. The middle floats travel further north, and

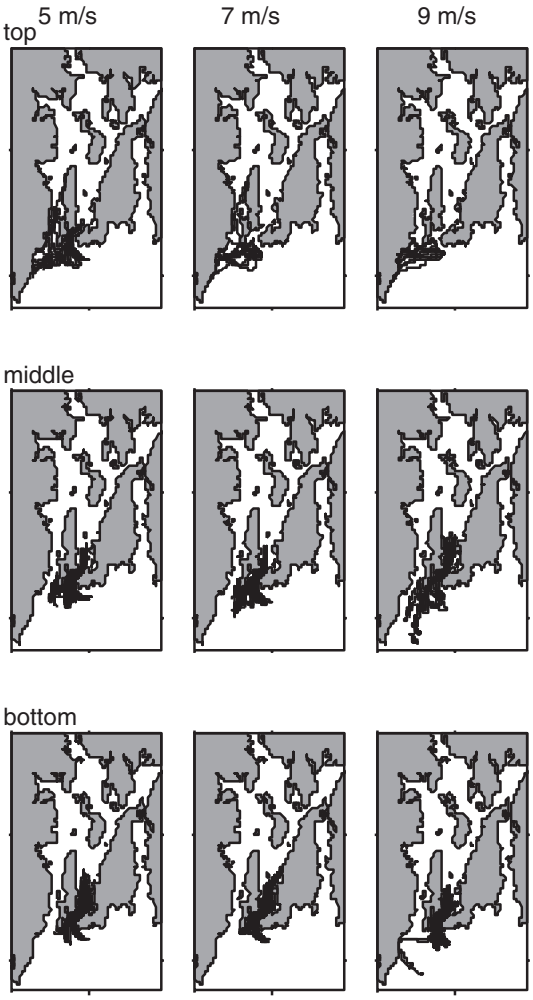

Figure 5. Path of oil spill. Easterlies. No salinity.

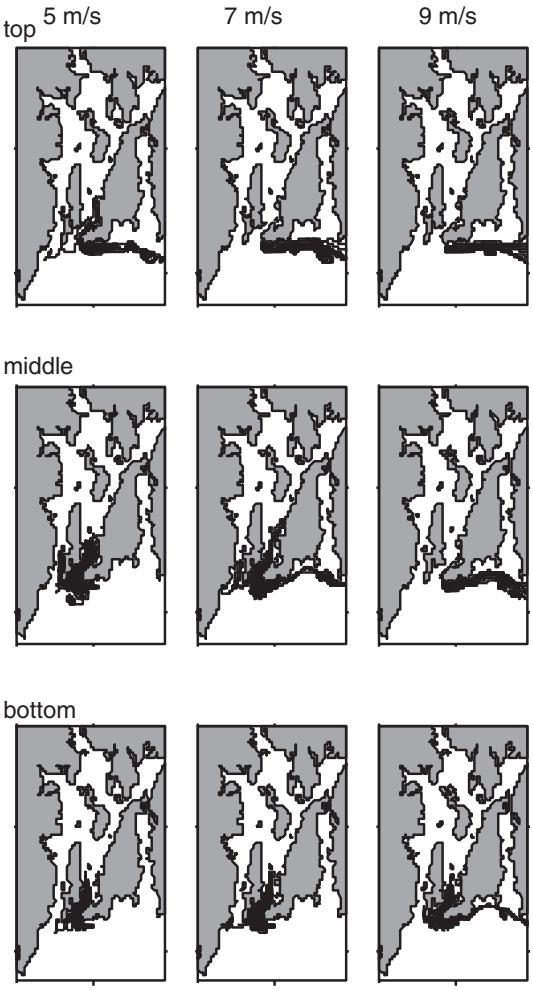

Figure 6. Path of oil spill. Westerlies. No salinity.

some floats travel up the west passage. The bottom floats move less to the east. For the westerly wind, the surface floats go much more to the east than with no wind. The middle floats move further north and south and the bottom floats move further north.

The runs that include variable salinity show the oil spreading out much more than the runs without variable salinity. Also, the wind influences the flow at the bottom and middle levels more than without salinity and the bottom and middle level floats move much further, especially to the north.

4.3. Effects of different magnitudes of wind speed

A number of studies (eg., Weisburg and Sturges, 1976) have shown that wind forcing is of equal magnitude to tides in terms of kinetic energy for estuarine systems. A set of experiments were run to quantify how the magnitude and direction of wind speed modulates surface versus bottom dispersion patterns.

Figure 10 shows the maximum latitude reached by the floats as a function of wind speed; these runs have no variably salinity. The four panels show the four wind directions, each with a separate curve for the top middle and bottom levels.

With the easterlies, at moderate wind speeds the surface floats move much further north than with no wind or at extreme wind speeds. The curve for the middle floats initially decreases and subsequently increases at very high wind speeds. The bottom curve does exactly the opposite, initially increasing and then decreasing at very high wind speeds. With the westerlies, the surface curve increases from no wind to the 5 m/s wind and then decreases. The middle curve is erratic, and the bottom curve decreases at a steady, slow rate.

The southerlies show the surface curve increasing very rapidly with wind speed. The middle and bottom curves are fairly flat. With the northerlies, the surface curve decreases, while the middle and bottom curves increase.

Figure 11 shows the minimum latitude reached by the floats as a function of wind speed. Once again, these runs do not include variable salinity.

With the easerlies, all of the curves initially increase and then decrease. However, the surface curve is fairly constant. With the westerlies, all the curves increase.

With the southerlies, the surface curve increases, while the middle and bottom curves increase and then decrease. With the northerlies, the surface curve

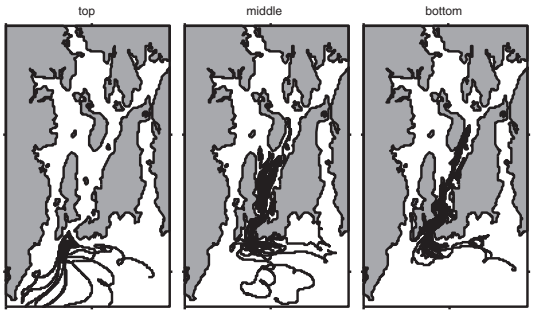

Figure 7. Path of oil spill. No wind. With salinity.

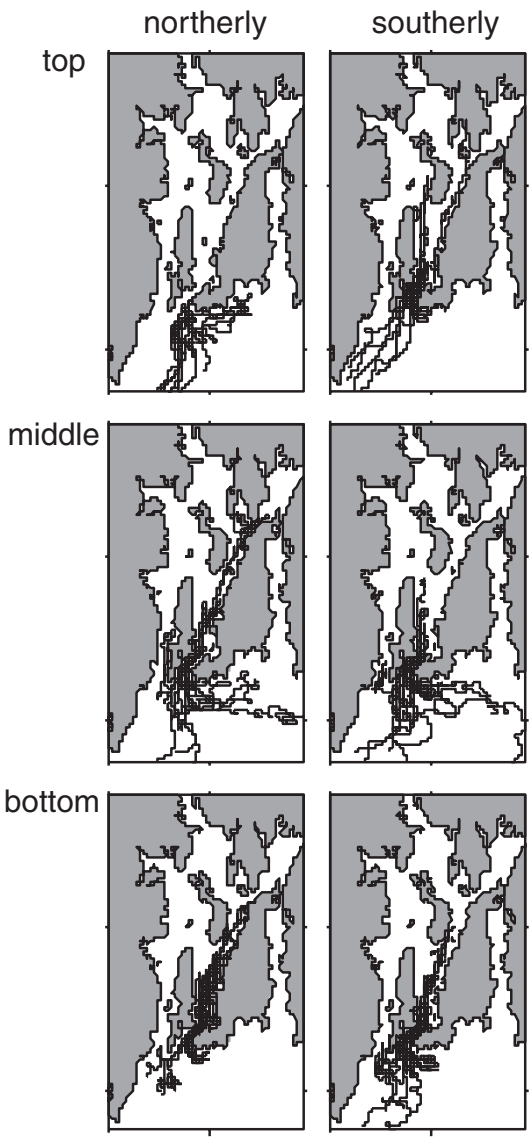

Figure 8. Path of oil spill. 5 m/s Northerly and Southerly. With Salinity.

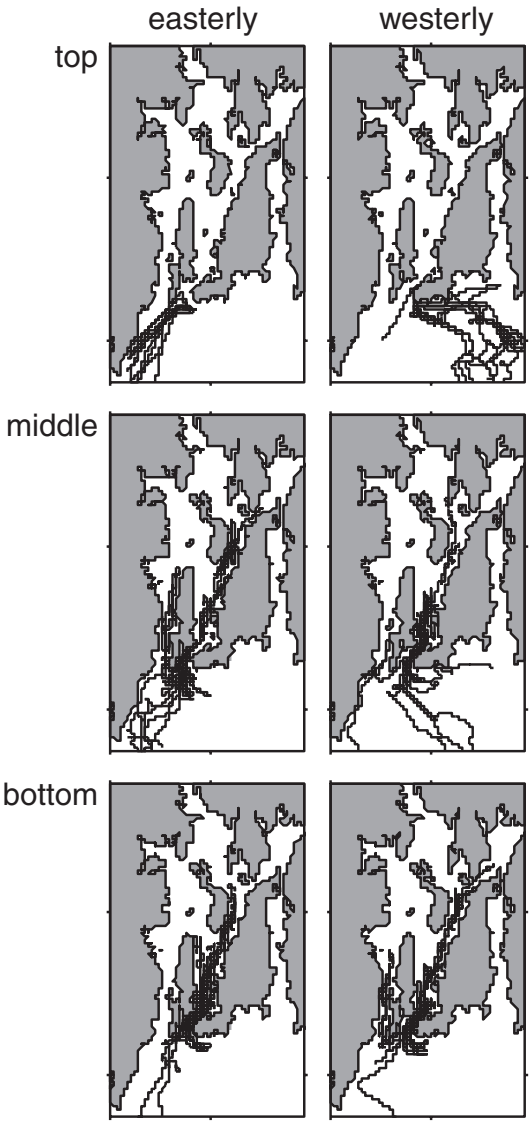

Figure 9. Path of oil spill. 5 m/s Easterly and Westerly. With Salinity.

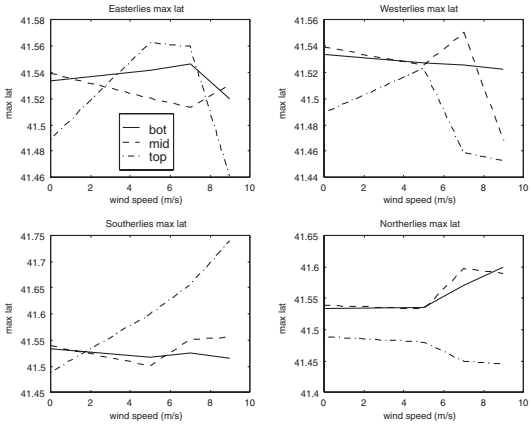

Figure 10. Furthest north floats reach vs wind speed.

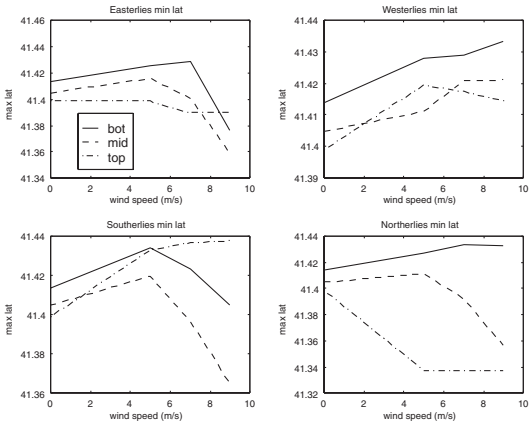

Figure 11. Furthest south floats reach vs wind speed.

decreases. (For all of the northerly winds, the floats reached the south boundary of the model.) The middle curve decreases, while the bottom curve increases slightly.

These plots show the nonlinear effects of surface winds. Few clear patterns were observed, but the middle and bottom curve behave fairly similarly.

5. Conclusions

It is clear that oil that mixes down into the water column behaves very differently than oil that remains at the surface. Models that only predict the spread of oil at the surface do not accurately predict the spread of oil if some oil mixes down into the water column. In order for the government to be able to respond better to an oil spill, models must be made that include deep water oil.

There is a drastic difference in the oil spill path and amount of spreading with and without salinity. This is due to the density difference induced by salinity, with fresh water at the surface moving out of the Bay and more saline, deeper water moving up into the Bay. Thus, hydrodynamical models that do not include density effects would predict far less deep transport.

The surface oil generally moves in the direction of the surface wind, while the deeper oil generally moves orthogonal to the wind if the wind is out of the east or west and opposite the wind if the wind is out of the north or south. The maximum opposite transport is at the middle level and not at the bottom. This could possibly be due to bottom friction.

6. Notation

D's	diffusive terms.
F's	forcing terms.
$f(x,y)$	Coriolis parameter.
g	gravitational acceleration.
P	total pressure.
$\phi(x,y,z,t)$	dynamic pressure, $\phi=(P/\rho_0)$.
$\rho(x,y,z,t)$	density.
$S(x,y,z,t)$	salinity.
$T(x,y,z,t)$	potential temperature.
u,v,w	(x,y,z) components of velocity vector $\vec{u}$.

Acknowledgments. I would really like to thank Bridget Sullivan and Chris Kincaid for their guidance, help, and suggestions. Thanks to everyone else, too.

References

Gordon, R. B., and Spaulding, M. L., 1987. Numerical Simulations of the Tidal- and Wind-Driven Circulations in Narragansett Bay. *Estuarine, Coastal and Shelf Science*, **24**, 611-636.

Haidvogel, D. B., Arango, H. G., Hedstrom, K., Beckmann, A., Malanotte-Rizzoli, P., Shchepetkin, A., 2000. Model evaluation experiments in the North Atlantic Basin: simulations in nonlinear terrain-following coordinates. *Dynamics of Atmospheres and Oceans*, **32**, 239-281.

Weisburg, R., and Sturges, W., 1976. Velocity Observations in the West Passage of Narragansett Bay: A Partially Mixed Estuary. *Journal of Physical Oceanography*, **6**, 345-354.

High-resolution paleomagnetic analysis of a sediment core from Lake Bosumtwi, Ghana

Becca Walker[1]

Graduate School of Oceanography, University of Rhode Island, Narragansett, Rhode Island

Abstract. The ability to predict future climate cycles requires a knowledge of past climate variations. Information about these past changes is recorded in sediments. In this study, we performed paleomagnetic analysis of a core from Lake Bosumtwi, a closed-basin crater lake in southern Ghana. These data aided in the construction of a high-resolution age model for sub-Saharan Africa. Assuming that regional climate variations are recorded magnetically in sediments, the magnetic measurements were utilized as a proxy for century-scale climate variation in West Africa.

Lake Bosumtwi provides a record of African climate variability and drought history over the last 27,500 years. Annual lamination sequences for at least 1000 years and perhaps as long as 20,000 years make the possibility of investigating both rapid and high-resolution climate change feasible. A piston core recently acquired from Lake Bosumtwi was u-channeled and analyzed using a cryogenic magnetometer to obtain inclination, declination, and relative intensity measurements. Paleosecular variation of Lake Bosumtwi was compared with a record of a nearby African lake, and an age-depth model for our core was produced. Environmental magnetic analyses were performed using additional magnetic mineral parameters. Our high-resolution model was compared with established, lower-resolution climate proxies to construct a climate change model.

Inclination and declination measurements for the upper 7 ka of the core correlate well to the regional PSV record, whereas correlations between 7-18 ka were less conclusive. Reduction diagenesis occurred during two intervals possibly related to intermittent storm events. These intervals are inferred to represent a deep, anoxic, low-energy lake environment. We speculate that the deep lake levels correspond to wet climate periods in sub-Saharan Africa.

1. Introduction

Climate change is becoming an increasingly important political, social, and scientific issue because of questions regarding anthropogenic influences on Earth's climate. These concerns have prompted paleoclimate studies because an understanding of past climate variability is necessary for the prediction of future climate change. Once knowledge about natural climate cycles is acquired, determining the extent of human influence on climate becomes feasible. King and Peck (in press) demonstrated that Holocene lacustrine sediments are particularly useful regional paleoclimate archives, provided that sedimentation rates exceed 30 cm/ka. This study presents high-resolution magnetic data from a Lake Bosumtwi, West Africa, sediment core.

The Earth's magnetic field undergoes small, temporal variations in direction and intensity over periods typically ranging from 10^2-10^5 years (Merrill and McFadden, 1990). This regional paleosecular variation (PSV) is recorded magnetically in sediments (Dunlop, 1997). The sediment magnetic properties are measured and provide information about past climate changes using paleomagnetic and environmental magnetic principles. We used paleomagnetic data and an already established, low-resolution secular variation curve from a nearby African lake to construct a secular variation curve for Lake Bosumtwi. Environmental magnetic data were used to interpret the lake's history over the last ~20 ka, generating a high-resolution model of regional climate change for sub-Saharan Africa. This is a collaborative project in which investigators will study varves, lithostratigraphy, and radiometric dates in addition to the rock-magnetic parameters addressed in this paper.

1.1. Origin of magnetic signals in lake sediment

Convection currents in the molten iron-nickel outer core and latent heat of crystallization from the freezing of the inner core provide energy for Earth's self-exciting dynamo (Merrill and McFadden, 1990). Mechanical energy from the fluid motion converts to magnetic energy and generates the Earth's magnetic field.

The geomagnetic field may be characterized by three parameters (Figure 1): inclination, declination, and intensity (Butler, 1992). Inclination (I), the plunge

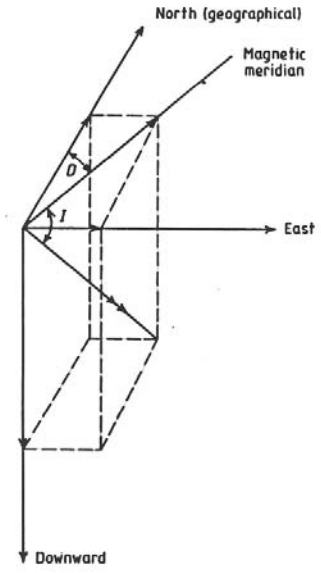

Figure 1. Diagram of inclination (I), declination (D), and intensity, the three vector components of the geomagnetic field. From Butler, 1992.

[1]Now at Hamilton College, Clinton, New York.

angle of field lines below the horizontal plane, depends primarily on the direction of Earth's magnetic field and is related to latitude (λ) by the equation:

$$\tan I = 2 \tan \lambda.$$

Inclination serves as a paleolatitude indicator although shallowing may be observed in certain depositional environments (see Levi and Banerjee, 1990, Butler, 1992). Declination refers to the angle between geographic and magnetic north and provides additional directional data. Intensity, a magnetic mineral concentration indicator, is characterized by the average dipole moment of the field (Butler, 1992). The geocentric axial dipole illustrates the time-averaged geomagnetic field over time scales greater than 10^4 years (Figure 2).

Some iron-bearing minerals exhibit paramagnetism, whereby a weak, temporary magnetization may be acquired in the presence of an applied field but is lost upon removal of the field (Thompson and Oldfield, 1986). In contrast, magnetic minerals have the capability to carry magnetic remanence even after the removal or alteration of the field. On the atomic scale, this remanence is acquired when a rock is below its Curie temperature and the spin magnetic moments of its electrons align themselves parallel to the ambient field (B. Tewksbury, pers. comm., 2001). The relevant magnetic minerals to this study are magnetite (Fe_3O_4), a ferrimagnetic mineral, and hematite (Fe_2O_3), a canted antiferromagnet. Magnetic moments in ferrimagnets are antiparallel and have different magnitudes (Figure 3a), creating a net magnetization (Thompson and Oldfield, 1986). Canted antiferromagnetic minerals have antiparallel magnetic moments of the same magnitude

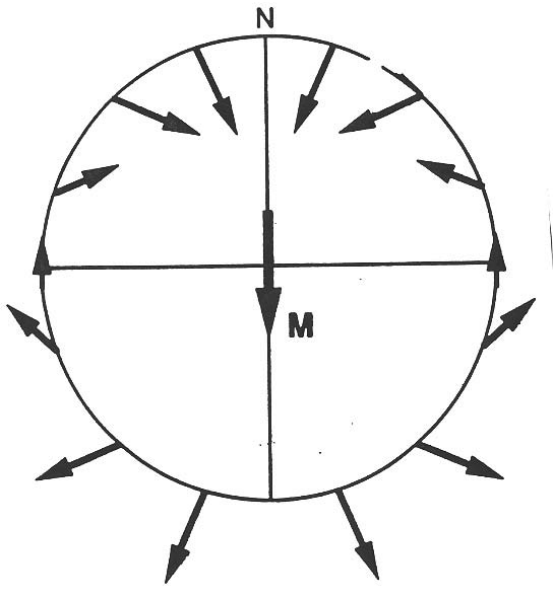

Figure 2. Schematic diagram of the geocentric axial dipole model for the geomagnetic field. M denotes the net magnetic moment of the field. From Butler, 1992.

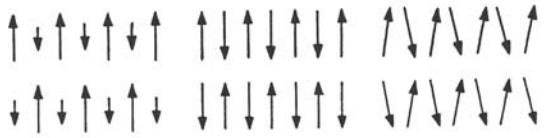

Figure 3. Sketches of magnetic moments in minerals. (left) Ferrimagnetic minerals (*eg*, magnetite). Individual spin magnetic moments are antiparallel with differing magnitudes, generating a net dipole. (center) and (right) Canted antiferrogmagnetic minerals (*eg*, hematite). Individual spin magnetic moments are antiparallel with the same magnitude (center). Expected net dipole is zero, but angling in the unit cell produces small net magnetic moments (right). From Thompson and Oldfield, 1986.

(Figure 3b), producing a net dipole of zero. However, slight angling of sublattices in the unit cell produces a net magnetic moment (Figure 3c) and weak magnetization (Butler, 1992).

1.2. Setting

Lake Bosumtwi (6°30'N, 1°25'W), one of Africa's few natural lakes, is located in the lowland forest zone of southern Ghana, West Africa (Figure 4). The hydrologically closed crater lake currently measures 78 m in depth and roughly 8 km in diameter (King et al., 2001). Breccia outcrops around the lake's perimeter, thrust faults dipping toward the center of the lake, and the presence of the Ivory Coast microtektites in nearby marine cores provide evidence that a meteorite impact at ~1.1 Ma produced the Lake Bosumtwi basin (Jones et al., 1981).

1.3. Paleoclimatological significance of Lake Bosumtwi

The hydrologic and sedimentary properties, diverse drought history, and geographic location of Lake Bosumtwi designate the lake as an ideal candidate for paleomagnetic and environmental magnetic studies. Lake Bosumtwi's permanent stratification results in anoxic conditions below 15 m depth (King et al., 2001), inhibiting bioturbation and contributing to sediment preservation. Sediments from the last 20 ka exhibit laminations, thin layers whose color, composition, and grain size differ from the surrounding laminae. Preliminary examination of the Bosumtwi cores indicates that lamination sequences have been annual (varved) for the last 1000 years and possibly as long as 20 ka (King et al., 2001). These annual changes in sedimentation will provide a high-resolution record of climate change in the area.

The diverse drought history of Lake Bosumtwi over the past 27,500 years has been documented in previous studies (*eg*, Talbot and Delibrias, 1977) and suggests that Holocene changes in the lake's hydrologic budget were coeval with that of other African lakes. Bosumtwi experienced high lake levels during the Early Holocene and subsequent regression during the Late Holocene

(Talbot and Delibrias, 1977). Analysis of another Bosumtwi core (B2000-16P) revealed an erosional boundary at roughly 13.6 ka suggesting a depth of 60 m below current levels (King et al., 2001).

The lake's location is ideal for paleomagnetic studies because its PSV record may provide information about past Sahel rainfall variations. Lake Bosumtwi lies just south of the Sahel, the savanna region of West Africa currently undergoing desertification but not yet considered part of the Sahara Desert. Talbot and Delibrias (1977) proposed that variations in Bosumtwi lake levels corresponded reasonably with variations in the moisture balance of the Sahel (Figure 5). While this relationship has been disputed in more recent studies (Opoku-Ankomah and Cordery, 1994), Bosumtwi sediments can play a role in examining variations in Sahel rainfall (King et al., 2001).

Sedimentation in the lake is heavily influenced by the monsoons. The North African monsoon is characterized

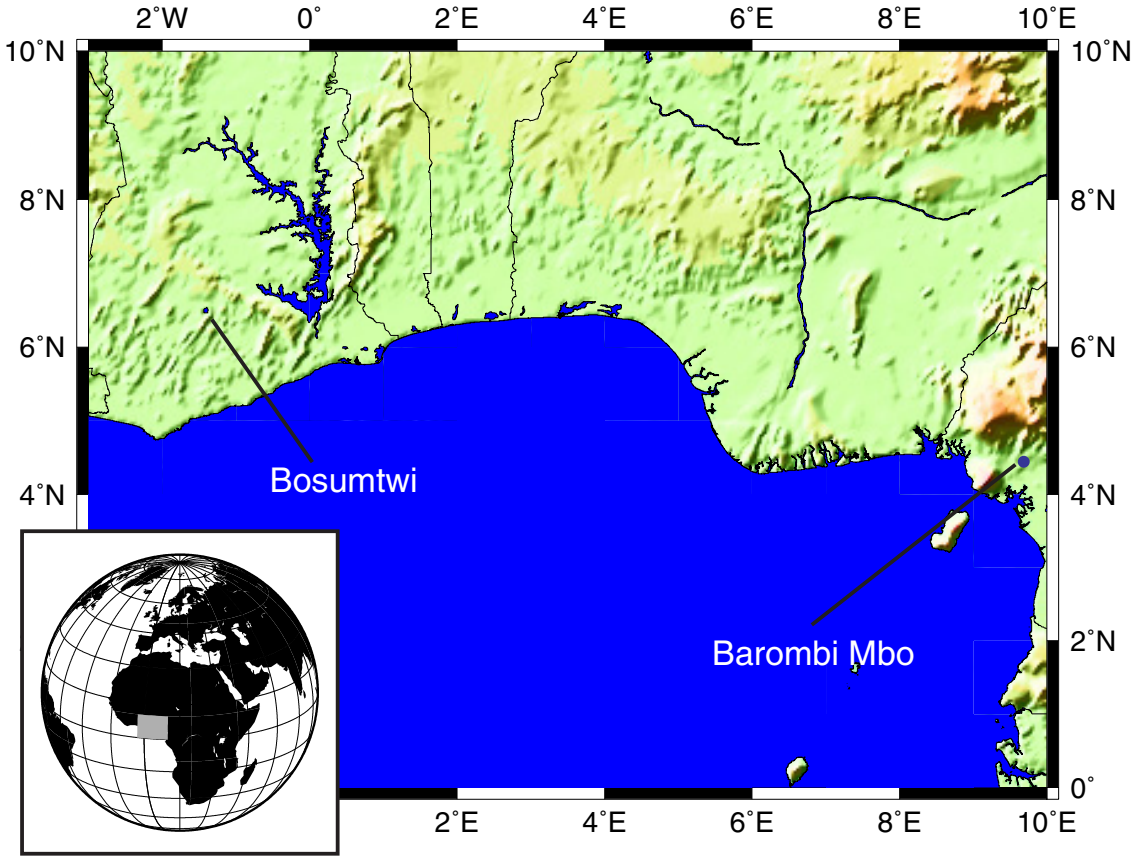

Figure 4. Study area location: Lake Bosumtwi, Ghana. Note that Lake Barombi Mbo, Cameroon, is also shown because PSV data from Barombi Mbo were used to construct an age model for Lake Bosumtwi. Figure by R. Viso, 2001.

by seasonal winds generated by the unequal heating of water and land surfaces. The dry, winter monsoon (Figure 6) is characterized by subsiding air over land moving offshore and advecting Saharan dust to the East Atlantic and West Africa (deMenocal et al., 1999). The land-sea pressure gradient reverses during the summer months as warm air rises over the continent and brings moist Atlantic air onshore. In contrast with the arid winter conditions, the summer monsoon (Figure 7) brings intense precipitation to sub-Saharan Africa (deMenocal et al., 1999). Bosumtwi's variable yearly precipitation—currently 17 mm in January and close to 234 mm in June—suggest that the lake's hydrologic budget is strongly influenced by the monsoons (King et al., 2001).

1.4. Magnetic minerals as climate proxies

The presence of magnetite and hematite in the Lake Bosumtwi sediments provides information about variations in the North African monsoon. Magnetite in the lake sediment results primarily from topsoil erosion, suggesting intense precipitation and a strong summer monsoon (J. King, pers. comm., 2001). Since dust flux from the Sahara transports hematite, the presence of hematite in the lake sediments implies arid conditions and a weakened summer monsoon. Increased dust transport indicates precipitation decreases in the source area (deMenocal et al., 1999) and suggests that Sahel climate variability plays an important role in sediment input into Lake Bosumtwi.

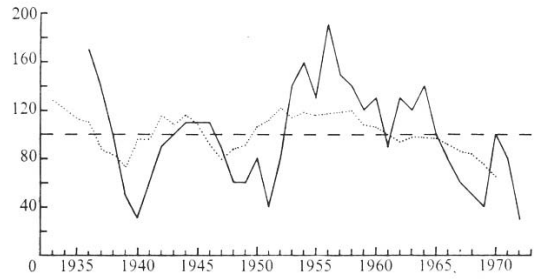

Figure 5. Graph illustrating the relationship between Sahel rainfall and the levels of Lake Bosumtwi from 1935-1972. From Talbot and Delibrias, 1977.

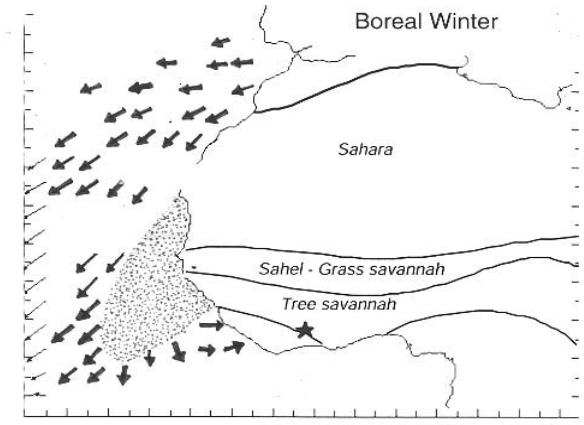

Figure 6. Predominant atmospheric circulation patterns accompanying the boreal winter (arid) North African monsoon. Offshore winds (arrows) generate the dust plume, denoted by the stippled area. Similar transport patterns occur on land, resulting in terrigenous flux from the Sahara and Sahel southward into the forest zone (tree savanna). Star represents Lake Bosumtwi. Modified from deMenocal et al., 1999.

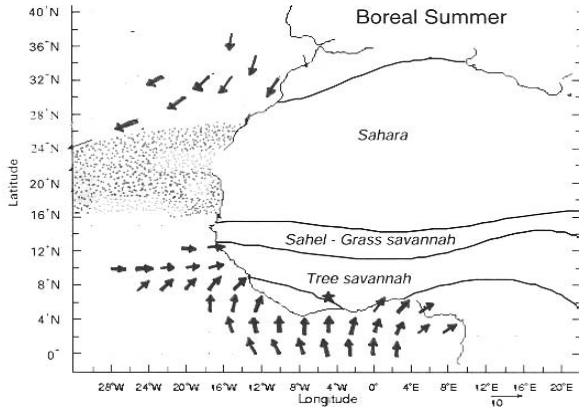

Figure 7. Illustration of atmospheric circulation patterns accompanying the boreal summer (wet) North African monsoon. Onshore winds (arrows) bring intense precipitation to the forest zone and Sahel. Position of the dust plume (stippled region) is generated by the African Easterly Jet. Star represents Lake Bosumtwi. Modified from deMenocal et al., 1999.

Sediment mineralogy may be influenced by a variety of other factors including reduction diagenesis and magnetotactic bacterial activity (King and Channell, 1991). These processes must be considered when using mineralogy as a climate proxy.

2. Methods

2.1. Core acquisition and sub-sampling procedure.

Nineteen piston cores were acquired from the central area of Lake Bosumtwi (Figure 8) during summer 2000. The cores were subsequently split and stored in the University of Rhode Island's sediment core repository. This paper presents results from core B2000-12P, which measured approximately 9 m in length. The core was cut into six sections, each roughly 150 cm in length.

U-channel samples were taken from the core in order to obtain magnetic measurements. U-channeling allows measurement of the sub-sampled sediment by a small access cryogenic magnetometer, which provides a high-resolution magnetic record at low sample intervals (King et al., 1983). In addition, sampling from the center of the core reduces the likelihood of encountering sediment disturbances acquired during coring (C. Heil, pers. comm., 2001). Samples of core B2000-12P were obtained during 6/22-6/29/01 at the University of Rhode Island Bay Campus. Six plastic u-channel tubes each measuring approximately 150 cm in length and 3.6 cm^2 in area were pressed into the central area of each split core section, parallel to the vertical axis of the core. Sediment-filled u-channels were subsequently removed, labeled, capped, and taped to prevent dessication. In general, laminations (possibly varves) were visible throughout the core. (Preliminary studies of the Bosumtwi cores (King et al., 2001) indicate that the cores are 70% strongly, 17% visibly, and 13% poorly laminated.)

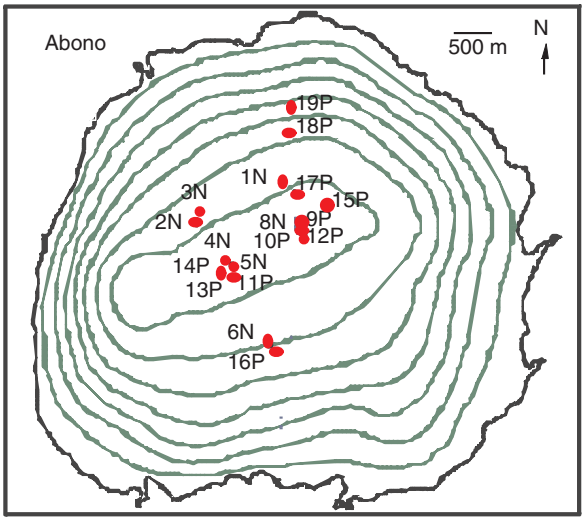

Figure 8. Bathymetric map of Lake Bosumtwi illustrating the location of B2000 series piston cores. Core 12P was analyzed in this paper. Contour interval is 10 m. From King et al., 2001.

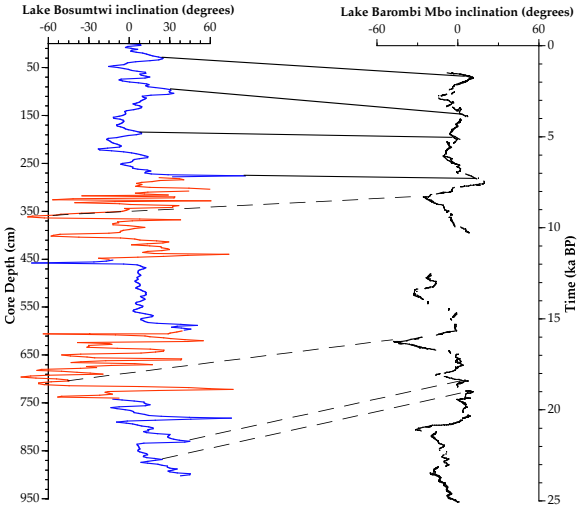

Figure 9. Comparison of PSV inclination data from B2000-12P (left) and Lake Barombi Mbo, Cameroon (right). Uncertain points are connected by dashed lines. Lake Barombi Mbo data from Thouveny and Williamson, 1988.

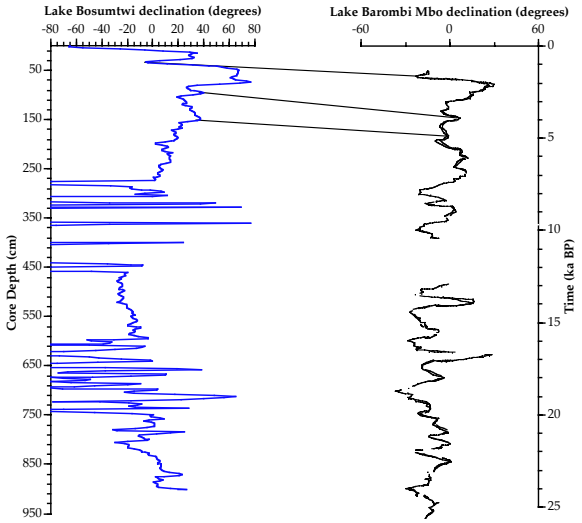

Figure 10. Comparison of PSV declination data from B2000-12P (left) and Lake Barombi Mbo, Cameroon (right). Lake Barombi Mbo data from Thouveny and Williamson, 1988.

2.2. Magnetic measurements.

Cryogenic magnetometers provide a rapid, nondestructive method of obtaining magnetic data from sediments (King and Channell, 1991). The sample passes through a chamber containing liquid helium (7 K), and the relatively weak magnetic remanence of the sediments is measured by SQUID (Superconducting Quantum Interference Device) sensors within the chamber (Butler, 1992). Removal of weak magnetic remanences acquired during coring, sub-sampling, or storage called overprints is accomplished by demagnetizing coils. U-channel samples were measured and underwent stepwise alternating field demagnetization up to 50 mT at 2.0 cm intervals on a 2-G Enterprises cryogenic magnetometer.

2.3. Paleomagnetic data.

Paleomagnetic studies use rock-magnetic measurements to characterize small changes in the Earth's magnetic field over time (Butler, 1992). Local PSV curves serve as correlation tools between sites, allowing sediment dating and the construction of age models.

Natural remanent magnetization (NRM) was measured first to obtain inclination, declination, and intensity data. These data would subsequently be compared to regional data and used to construct an age model (figures 9-11). NRM is a vector component whose magnitude and direction are functions of the geomagnetic field at the time of rock formation (Dunlop, 1997). While total NRM includes chemical, detrital, and thermoremanence (Dunlop, 1997) magnetic analysis of lake sediments relies primarily on detrital remanent magnetization (DRM). DRM is the alignment of magnetic grains during deposition and lithification and is influenced by grain size, rate of deposition, and bioturbation (Thompson and Oldfield, 1986). Under certain circumstances, sediment may acquire weak, unstable forms of secondary NRM subsequent to deposition (Dunlop, 1997). Such magnetic overprints interfere with the primary NRM signal and must be eliminated through a series of demagnetization steps. Paleomagnetic measurements for core B2000-12P were obtained using a cryogenic magnetometer, and the appearance and removal of these overprints were observed in demagnetization (Zidjerveld) plots.

2.4. Environmental magnetic data.

Environmental magnetism uses mineral magnetic properties in sediments including concentration, mineralogy, and grain size as indicators of paleoenvironmental change (Negrini et al., 2000). Variations in these properties are used to infer changes in depositional environment, weathering and erosion, sediment source regions, and sediment transport mechanisms caused by regional climate variability (King and Channell, 1991). Environmental magnetic data were generated from ARM, IRM, and magnetic susceptibility measurements.

Anhysteretic remanent magnetization (ARM) is a laboratory-induced magnetization typically used as a grain size and concentration indicator in environmental magnetic studies (Thompson and Oldfield, 1986). ARM was imparted at 0.1 mT in the Z direction using a steady D/C field.

Isothermal remanent magnetization (IRM) serves as an indicator of grain size and the concentration of magnetite (Thompson and Oldfield, 1986). This laboratory-imparted remanence involves subjecting a sample to a strong, steady magnetic field, followed by a series of AF demagnetization steps. Saturation IRM (SIRM) was imparted at 1200 mT in the +Y direction, measured, and subjected to stepwise alternating field

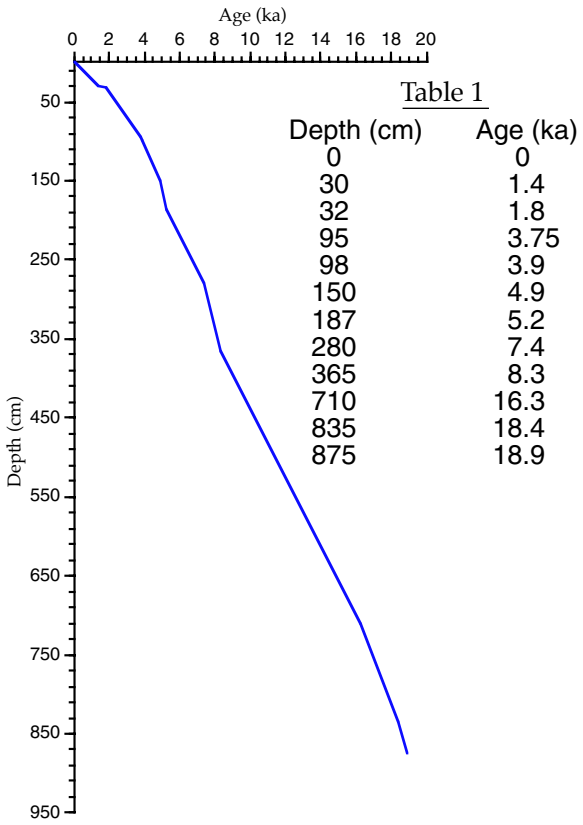

Table 1

Depth (cm)	Age (ka)
0	0
30	1.4
32	1.8
95	3.75
98	3.9
150	4.9
187	5.2
280	7.4
365	8.3
710	16.3
835	18.4
875	18.9

Figure 11. Age model for Lake Bosumtwi using the paleosecular variation record**.** Depths from core B2000-12P and corresponding ages from Lake Barombi Mbo PSV data (Thouveny and Williamson, 1988) shown in Table 1 were used to construct the dpeth-age curve.

demagnetization up to 50 mT. The samples were then resaturated, and back IRM (BIRM) was imparted at 300 mT in the –Y direction. Again, the samples were measured and demagnetized. Note that HIRM data (Figure 14) were obtained by forward saturation at 1200 mT, measurement of SIRM, BIRM at 300 mT, and measurement of BIRM.

Magnetic susceptibility (K) refers to the ease at which a sample is magnetized (Thompson and Oldfield, 1986). As an environmental parameter, K varies directly with both concentration and grain size of magnetic minerals (Verosub and Roberts, 1995). Susceptibility data were obtained previously from a Geotek multisensing core logger.

2.5. Age model.

There are currently no other high-resolution secular variation curves from Lake Bosumtwi for comparison to our PSV curve. Thouveny and Williamson (1988) utilized magnetic and radiocarbon data from Lake Barombi Mbo, Cameroon (4.5°N, 9.5°E- Figure 1) to construct a Holocene (0-25 ka) paleosecular variation curve for the lake. Using our inclination and declination data, the high-resolution PSV curve of Bosumtwi was compared to Barombi Mbo's low-resolution PSV curve for age correlation (Figure 9, 10). Tie points were drawn, and an age-depth model (Figure 9) for Lake Bosumtwi was constructed. A rough basal age for core B2000-12P was obtained using lithostratigraphic correlations between cores B6/7 and B2000-12P (Figure 12) and ^{14}C dates from core B/67 (Talbot and Johannessen, 1992).

3. Results

3.1. Magnetic measurements.

Inclination for core B2000-12P serves as an accurate paleolatitude indicator because the data correspond well to the expected GAD (roughly 12.8°). Notable exceptions occur in two intervals of the core, 280-450 cm and 600-740 cm, in which noisy inclination data were noted (Figure 13). Declination data also exhibited extreme variability in these intervals (Figure 13). The relative intensity curve (Figure 13) showed sharp peaks indicating the presence of magnetic minerals. However, we noticed that magnetic intensity dropped sharply (essentially to zero) over the same intervals as the fluctuating directional data, roughly 280-450 cm and 600-740 cm (Figure 13). Susceptibility measurements (Figure 14) also showed low concentrations of magnetic minerals in the 280-440 cm and 590-730 cm intervals. The extreme drop in susceptibility around 305 cm corresponds to a void in the u-channel sample.

Environmental magnetic measurements are presented using K_{ARM}/SIRM and K_{ARM}/susceptibility ratios, HIRM, and the S parameter (Figure 14). Anhysteretic

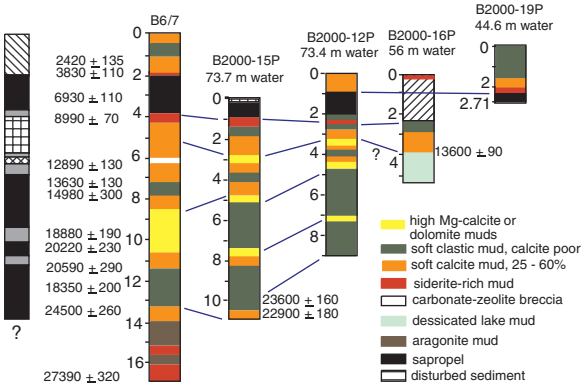

Figure 12. Lithologic correlations between cores B 6/7 (Talbot et al., 1984) and B2000-12P. Correlations are also shown between Talbot's core and three other cores from the B2000 suite. Correlations between 19P, 16P, 12P, and 15P are based upon major lithostratigraphic intervals. Correlations between 12P and 15P based on individual marker laminae. B6/7 can be correlated to 12P and 15P on major lithofacies and 2 laminated dolomite beds; correlations below 7 m depth in 15P may be obscured by slumping and scoured surfaces in B6/7. Left-hand column represents a composite core based on piston and freeze-cores summarizing the laminated (likely varved) sediment stratigraphy. Striped sections are well-laminated (70%), grey are fairly laminated (17%), and black is unknown (13%) until thin-sectioning is complete. From King et al., 2001

susceptibility (K_{ARM}) serves as a grain-size normalizer. K_{ARM}/SIRM and K_{ARM}/susceptibility vary inversely with magnetic grain size. HIRM serves as an indicator of the concentration of high-coercivity minerals (*ie*, hematite and goethite) and is the average of the SIRM and BIRM measurements (King and Channell, 1991):

$$\text{HIRM} = \frac{\text{BIRM} + \text{SIRM}}{2}$$

The S parameter is designated by the ratio of BIRM to SIRM and indicates the relative amounts of hematite-like minerals and magnetite-like minerals in a sample (Negrini et al., 2000). S-parameter values close to 1 indicate higher proportions of magnetite relative to hematite, while ratios of less than 1 suggest greater ratios of hematite relative to magnetite (Thompson and Oldfield, 1986).

Each remaining environmental magnetic parameter exhibited coherent behavior over the same depth intervals. K_{ARM}/SIRM and K_{ARM} /susceptibility ratios exhibited relatively high values from 0-290 cm, indicating the presence of fine-grained magnetic sediment. Magnetic grain size was inferred to increase from 290-450 cm, based on the dramatic drop in both ratios (Figure 14). From 450 cm downcore, the K_{ARM} /susceptibility data appeared to provide a more sensitive record of grain size variation. Fine-grained magnetic material was detected from roughly 450-600 cm, with a greater proportion of coarse magnetic grains evident over the interval of 600-820 cm (Figure 14). Magnetic grain size trends were similar for the K_{ARM}/SIRM ratio but with lower resolution.

Spikes in the top 280 cm of the HIRM data indicated relatively high concentrations of hematite-like minerals in the sediment (Figure 14). From 280-440 cm, extremely low concentrations of hematite were inferred by HIRM values of essentially zero. Hematite concentration increased over the interval of 440-590 cm and dramatically decreased from 590-740 cm (Figure 14). This virtual absence of hematite-like minerals was followed by an increase in hematite concentration in the lower 160 cm of sediment. Note that low HIRM sections of the core correspond with the fluctuating inclination and declination data, low magnetic intensity, and coarse magnetic grain size intervals.

S parameter measurements indicated greater proportions of hematite relative to magnetite over similar intervals. Notably, the magnetite/hematite ratio was considerably less than 1 from 320-450 cm and 590-750 cm (Figure 14). Missing data from 272-282, 442-446, and 824-828 cm resulted from SIRM.

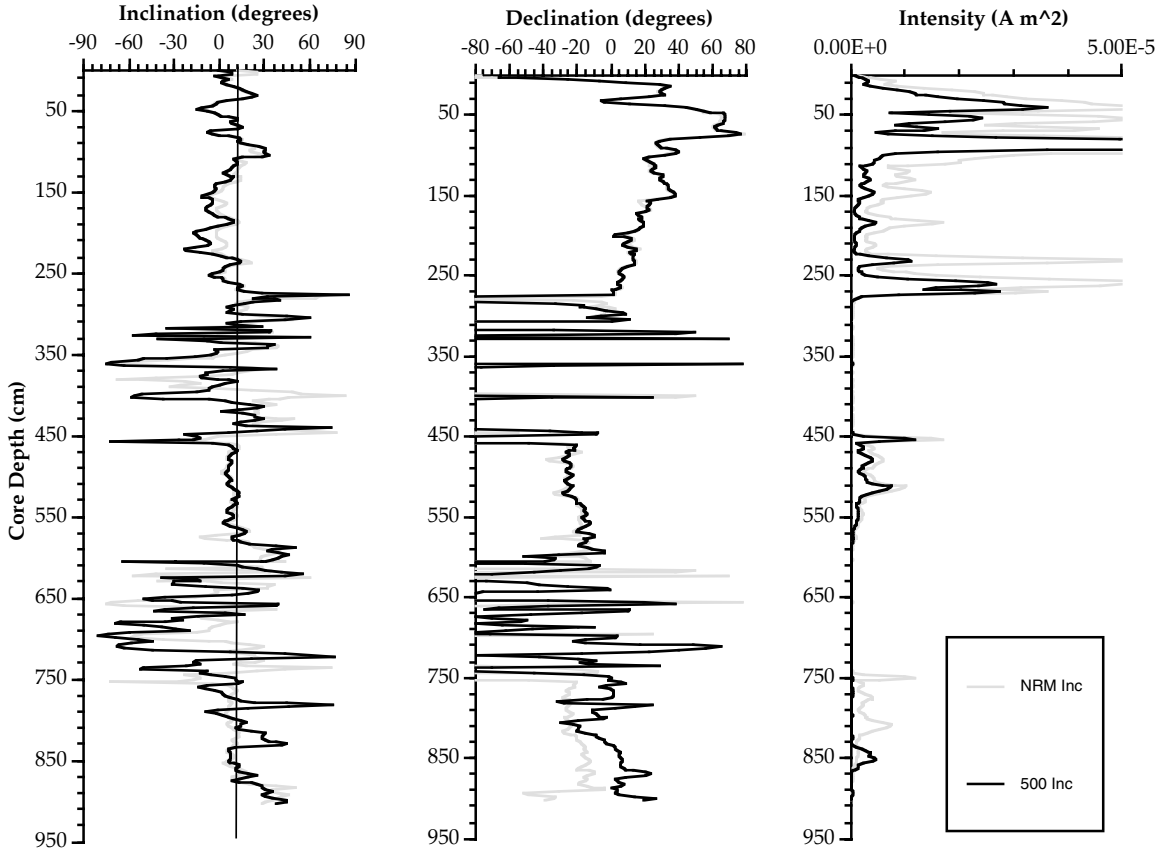

Figure 13. Paleomagnetic data from core B2000-12P. Sample interval is 2.0 cm; total NRM and 50 mT demag steps are shown, as well as expected GAD. (a) Inclination, declination, and relative intensity are shown. Note turbidite-like storm intervals at approximately 280-450 cm and 600-740 cm.

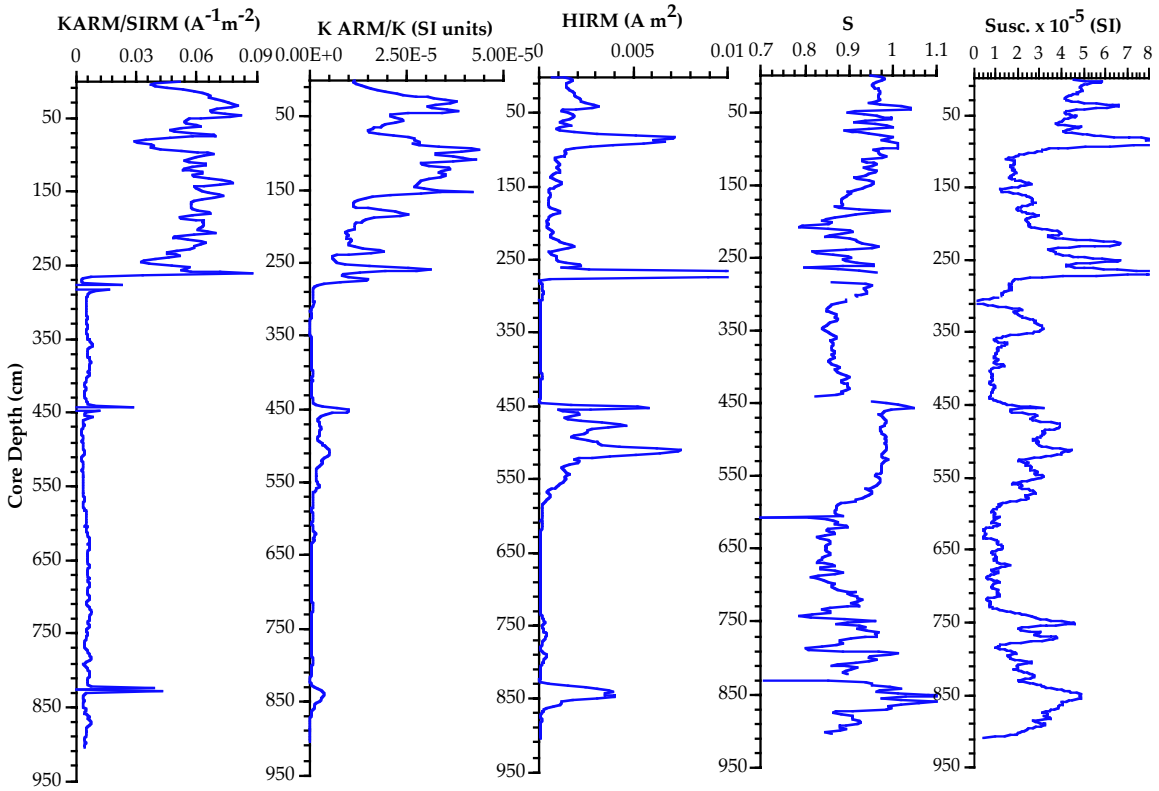

Figure 14. Environmental magnetic parameters for core B2000-12P.

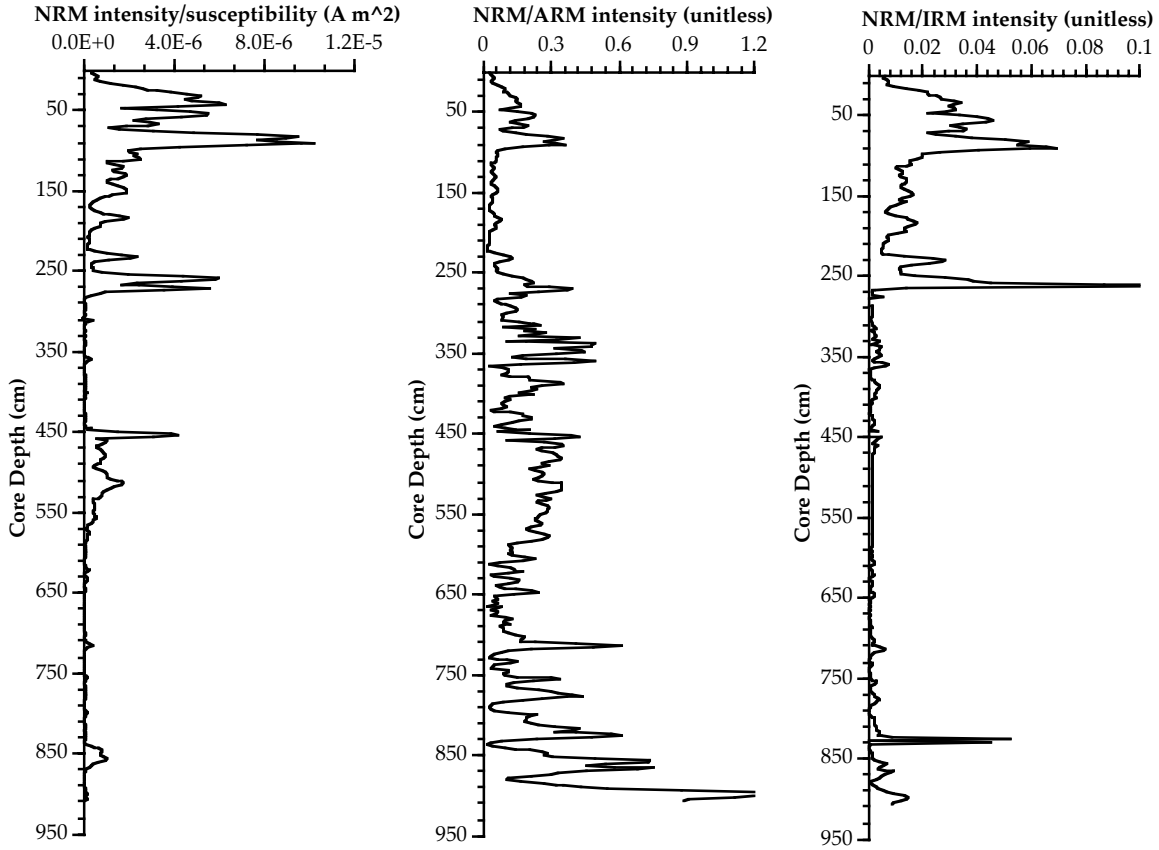

Figure 15. Paleointensity plots for core B2000-12P.

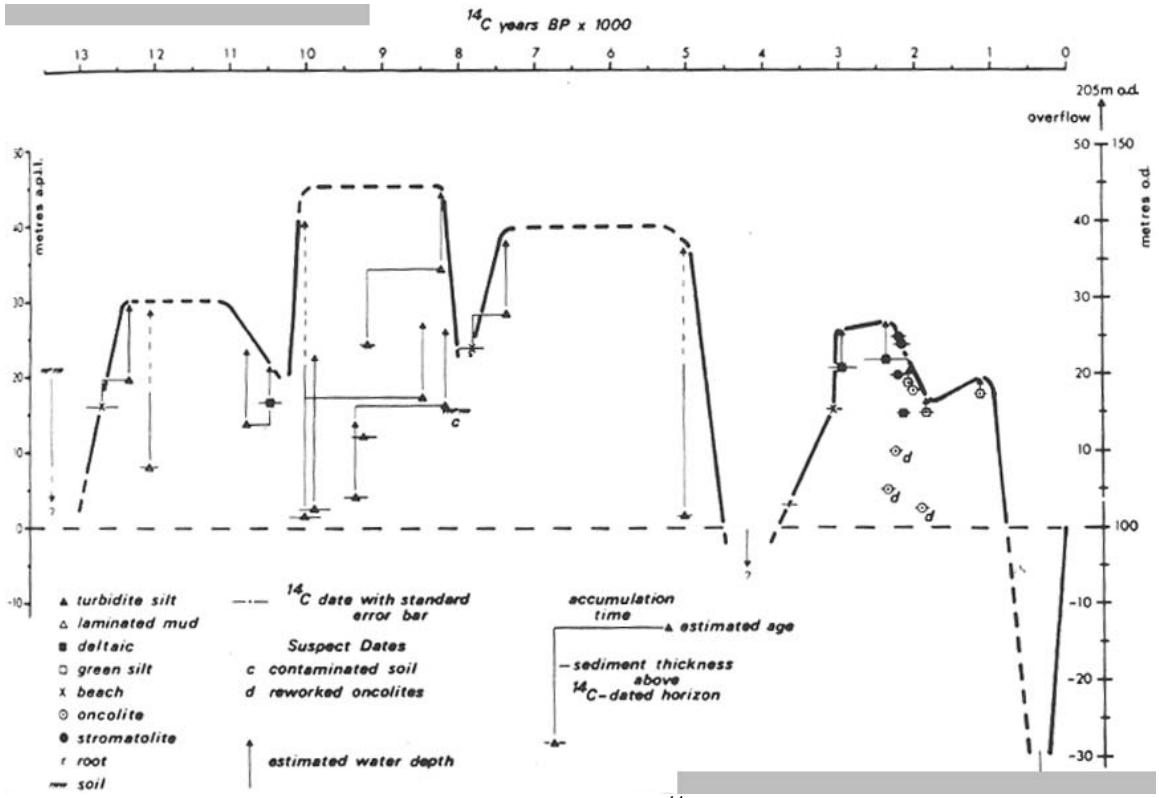

Figure 16. Lake-level curve for Lake Bosumtwi for the last 13.5 ka. ^{14}C dates, facies symbols and inferred lake levels are indicated. From Talbot and Delibrias, 1980.

measurements less than zero. The cause of these anomalous data remains unclear, but possibilities include contamination from the cutting tool used to split the core or mineralogical changes over these intervals. Further investigation is needed

NRM/ARM, NRM/susceptibility, and NRM/SIRM curves (Figure 15) were constructed as paleointensity proxies. All but NRM/ARM exhibited extreme lows over the same intervals, 280-450 and 600-740 cm, as well as 740-830 cm in the case of NRM/susceptibility.

3.2. Regional PSV and age model.

The basal age for core B2000-12P was constrained at roughly 18 ka based on age/depth data from Talbot and Johannessen (1992) and the lithology of B2000-12P (Figure 12). We proceeded to compare our high-resolution PSV curves for Lake Bosumtwi with the records of Lake Barombi Mbo (Thouveny and Williamson, 1988). Many similarities were seen between the inclination records (Figure 9), specifically in the upper 250 cm of core B2000-12P (0-6 ka for Lake Barombi Mbo.) Notable match points between the PSV curves occur at approximately 32 cm, 98 cm, 187 cm, and 280 cm for core B2000-12P (Figure 11, Table 1). We also found some possible match points further downcore, including in the regions of highly variable inclination measurements for B2000-12P. While these fluctuations are not evident in the Barombi Mbo record, we observed large inclination peaks and troughs at roughly 7.5 ka and 16.5 ka (Figure 9). Since this is a low-resolution PSV curve relative to our Bosumtwi data, the peaks and troughs may correspond to the fluctuations noted in Bosumtwi's PSV curve.

Declination data yielded fewer match points relative to inclination measurements, but we observed three reasonable tie points in the upper 150 cm of core B2000-12P (Figure 10). Declination fluctuations noted in our core were not seen in the Barombi Mbo data and made comparison of the lakes below 250 cm difficult.

PSV match points from our inclination and declination measurements were combined and used in conjunction with corresponding depths from the Barombi Mbo records (Figure 11, Table 1) to construct an age model for core B2000-12P (Figure 11). No significant variations in sedimentation rate were observed, and these data constrained the basal age of the core at roughly 19 ka. Our age model dates the anomalous intervals at roughly 7-10 ka and 14-16.5 ka.

4. Discussion

Despite two intervals of anomalous magnetic data, core B2000-12P PSV records for the top ~7 ka correlate well with the Barombi Mbo record, and our inclination data fit the expected GAD. With respect to core depth, the unusual patterns are highly correlative between both the directional and environmental magnetic measurements. Thus, we are confident that these intervals represent some sort of lithologic—and perhaps environmental—change.

The highly variable inclination data are interpreted to represent turbidite-like intervals which may represent storm layers. We do not classify these events as turbidites because true turbidites arise from slope collapse. We believe that the intervals of noisy directional data represent a series of storm events with fluvial influx into the lake, alternating with pelagic lake intervals. The variability in the directional data may arise from the discrete, randomized storm events within the intermittent pelagic intervals (C. Heil, pers. comm., 2001). Talbot and Delibrias (1980) suggest that certain silts and finely laminated muds in the Bosumtwi sediments represent primordial turbidity underflows that settled in anoxic waters. This inference and an existing water-level curve for Lake Bosumtwi (Figure 16) indicate that the inferred "turbidite-like" (storm?) intervals correspond to deep lake levels and a low-energy depositional environment. Lithostratigraphy and observations made during u-channeling reveal the expected fine-grained, strongly laminated sediment in the turbidite-rich intervals.

We believe that reduction diagenesis during these intervals is responsible for the low NRM intensity, susceptibility, and environmental magnetic values observed over the 280-450 cm and 600-740 cm intervals. These low points represent intervals in which the primary magnetic signal has been obscured by diagenetic processes in the sediment. Dramatic decreases in magnetic susceptibility in both turbidite-like storm intervals (Figure 14) indicate decreases in magnetic mineral concentration. Magnetic intensity is drastically reduced during these periods (Figure 13) and indicates the removal of magnetic carriers in the sediment. We believe that this was accomplished through reduction diagenesis.

Diagenesis artificially depresses HIRM values over the same intervals. We consider the apparent hematite decrease feasible because the turbidite-like storm intervals represent a deep, essentially anoxic lake (Talbot and Delibrias, 1980). Diagenetic processes in anoxic environments typically involve the conversion of ferric iron (the primary form of iron in hematite) to ferrous iron (J. King, pers. comm., 2001). We have briefly considered HIRM as a lake-level proxy because in general, high HIRM values correspond with low or regressing lake levels, while very low HIRM values correspond with high lake levels (Figures 14 and 16). This idea needs further analysis because of the reduction diagenesis and the 110-270 cm intervals, in which high HIRM values correspond to rising lake levels (Figures 14 and 16).

S parameter decreases in the turbidite-like storm intervals (Figure 14) suggest higher proportions of hematite relative to magnetite. Even though both magnetite and hematite are altered during diagenesis, magnetite is typically removed first because of its generally fine-grained, single domain grain nature (King and Channell, 1991). Preferential diagenesis of magnetite leads to the lower S ratios in the turbidite-like storm intervals.

Low K_{ARM}/SIRM and K_{ARM}/susceptibility values in the turbidite-like storm intervals were initially counterintuitive. During these intervals, the curves show higher proportions of coarse-grained material in a low-energy environment (Figure 14). Note, however, that these ratios reflect magnetic grain size rather than sediment grain size. The data are showing a selective diagenesis of fine-grained magnetic material during the turbidite-like storm intervals, leaving behind coarser grains. Therefore, these magnetic grain size ratios indicate the effects of reduction diagenesis and not lake energy (J. King, pers. comm., 2001).

Highly organic sediment (sapropel) is present between 93.5-218.5 cm, roughly 3.5-5.5 ka according to our age model. When we compare these intervals to the lake level curve (Talbot and Delibrias, 1980), it appears as though the sapropel was deposited during periods of intermediate or low lake levels. Environmental magnetic parameters, relative intensity, and susceptibility measurements in this interval indicate a stronger magnetic signal compared to the turbidite-like storm intervals, but slightly depressed levels are observed. Therefore, we cannot rule out the possibility of some diagenetic activity during this period.

Our paleointensity curves do not accurately depict changes in the geomagnetic field. Our NRM/susceptibility and NRM/SIRM curves are shaped similarly (Figure 15), but both exhibit the same trends as the environmental magnetics parameters (*ie*, low values in the turbidite-like storm intervals.) This implies that the shape of the curves is controlled primarily by lithologic changes, rather than geomagnetic secular variation. Based on shape, it is possible that the NRM/ARM data obtained from this core may serve as a suitable paleointensity record. Since changes in the geomagnetic field should be global, we suggest a comparison of these data to other African paleointensity curves.

5. Implications

At this stage, we may only speculate about the strength of the African monsoon during the period represented by core B2000-12P. The turbidite-like storm intervals occurred during times of deep lake levels, which may indicate wet climate periods. We would expect hematite-rich intervals to correspond with arid periods. During these times, lake sediments should predominantly consist of terrigenous flux from the Sahara. However, reduction diagenesis in the turbidite intervals has attenuated the primary magnetic signal and adds difficulty to climate interpretation. We hope to find a more complete record of climate change from magnetic analysis of additional Lake Bosumtwi cores. Future varve examination, radiometric dating, and lithostratigraphic analysis will also be useful in developing a clearer record of climate variability from the cores. A more detailed investigation of the cause(s) and mechanism of the inferred diagenesis would be an interesting undertaking as well.

The next step in this study involves coupling our high-resolution model to general atmospheric circulation models to document African monsoon variability. Examining the effects of SST/precipitation,

vegetation/albedo, precipitation/evaporation, and orbital forcing feedback systems on changes in the monsoon (see deMenocal et al., 1999, Talbot and Delibrias, 1977, Palmer, 1986, Opoku-Ankomah et al., 1994) would also be beneficial. High-resolution, paleomagnetic analysis of an African lacustrine sediment core has put us one step closer to predicting African drought cycles and understanding anthropogenic influences on global climate change.

Acknowledgments. I thank Chip Heil, John King, and Carol Gibson for this research experience, their assistance with this project, their patience, and much insight into reduction diagenesis, DeltaGraph, and Microsoft Excel. Rob Pockalny, Paul Hall, Chris Kincaid, Rhonda Kenny, and Kim Carey organized the 2001 SURFO program and provided me with this opportunity. Members of the geophysics reading group gave me feedback on my presentation, helped improve my speaking skills, and made the location map used in this paper. I'd also like to thank the other eight people who lived at 16 Lilly Lane—Erin, Shaevitz, Brent, Nicky, Robin, Marcie, Brenda, and Angela—for an awesome summer. (The SURFO house is far superior to The Real World!)

References

Butler, R.F., 1992, Paleomagnetism: Boston, Blackwell Scientific Publications, 319 p.

deMenocal, P.J., Ortiz, O., Guilderson, T., Adkins, J., Sarnthein, M., Baker, L., and Yarusinsky, M., 2000, Abrupt onset and termination of the African Humid Period: rapid climate responses to gradual insolation forcing: Quaternary Science Review, v. 19, p. 347-361.

Dunlop, D.J., and Ozdemir, O., 1997, Rock magnetism: fundamentals and frontiers: Cambridge, Cambridge University Press, 573 p.

Jones, W.B., Bacon, M. and Hastings, D.A., 1981, The Lake Bosumtwi impact crater, Ghana: Geological Society of America Bulletin, v. 92, p. 342-349.

King, J.W., Peck, J.A., Overpeck, J.T., and Scholz, C.A., 2001, Collaborative research: high-resolution paleoclimatology from newly acquired sediment cores from Lake Bosumtwi, Ghana: proposal #0117414 to the National Science Foundation.

King, J.W., and Channell J.E.T., 1991, Sedimentary magnetism, environmental magnetism, and magnetostratigraphy: Reviews of Geophysics supplement, U.S. National Report to International Union of Geodesy and Geophysics, p. 358-370.

King, J.W., Banerjee, S.K., and Marvin, J., 1983, A new rock-magnetic approach to selecting sediments for geomagnetic paleointensity studies: application to paleointensity for the last 4000 years: Journal of Geophysical Research, v. 88, p. 5911-5921.

King, J., and Peck, J., in press, Use of paleomagnetism in studies of lake sediments, *in* Developments in Paleoenvironmental Research, Journal of Paleolimnology.

Levi, S., and Banerjee, S., 1990, On the origin of inclination shallowing in redeposited sediments: Journal of Geophysical Research, v. 95, p. 4383-4390.

Merrill, R.T., and McFadden, P.L., 1990, Paleomagnetism and the nature of the geodynamo: Science, v. 248, p. 345-350.

Negrini, R.M., Erbes, D.B., Faber, K, Herrera, A.M., Roberts, A.P., Cohen, A.S., Wigand, P.E., and Foit, F.F., Jr., 2000, A paleoclimate record for the past 250,000 years from Summer Lake, Oregon, USA: I. Chronology and magnetic proxies for lake level: Journal of Paleolimnology, v. 24, p. 125-149.

Opoku-Ankomah, Y., and Cordery, I., 1994, Atlantic sea surface temperatures and rainfall variability in Ghana: Journal of Climate, v. 7, p. 551-558.

Palmer, T.N., 1986, The influence of the Atlantic, Pacific, and Indian Oceans on Sahel rainfall: Nature, v. 322, p. 251-253.

Talbot, M.R., and Johannesen, T., 1992, A high resolution palaeoclimatic record for the last 27,500 years in tropical West Africa from the carbon and nitrogen isotopic composition of lacustrine organic matter: Earth and Planetary Science Letters, v. 110, p. 23-37.

Talbot, M.R., and Kelts, K., 1986, Primary and diagenetic carbonates in the anoxic sediments of Lake Bosumtwi, Ghana: Geology, v. 14, p. 912-916.

Talbot, M.R., and Delibrias, G., 1980, A new Late Pleistocene-Early Holocene water-level curve for Lake Bosumtwi, Ghana: Earth and Planetary Science Letters, v. 47, p. 336-344.

Talbot, M.R., and Delibrias, G., 1977, Holocene variations in the level of Lake Bosumtwi, Ghana: Nature, v. 268, p. 722-724.

Thompson, R., and Oldfield, F., 1986, Environmental magnetism: London, Allen and Unwin, 227 p.

Thouveny, N., and Williamson, D., 1988, Palaeomagnetic study of the Holocene and Upper Pleistocene sediments from Lake Barombi Mbo, Cameroun: first results: Physics of Earth and Planetary Interiors, v. 52, 193-206.

Verosub, K.L., and Roberts, A.P., 1995, Environmental magnetism: past, present, and future: Journal of Geophysical Research, v. 100, p. 2175-2192.